UNIVERSITÀ DI ROMA "LA SAPIENZA"

DIPARTIMENTO DI INGEGNERIA MECCANICA E AEROSPAZIALE
DOTTORATO DI RICERCA IN TECNOLOGIA AERONAUTICA E SPAZIALE
XXIV CICLO

PH.D. THESIS

Flow Field and Heat Transfer Analysis of Oxygen / Methane Liquid Rocket Engine Thrust Chambers

Barbara Betti

SUPERVISOR
Prof. Francesco Nasuti

June 2012

Author's e-mail: barbara.betti@uniroma1.it

Author's address:

Dipartimento di Ingegneria Meccanica e Aerospaziale
Università di Roma "La Sapienza"
Via Eudossiana, 18
00184 Roma – Italia
web: `http://www.dima.uniroma1.it`

Abstract

This study is devoted to the characterization and analysis of the flow field and heat transfer in oxygen/methane liquid rocket engines. Attention is focused on the hot gas side of the thrust chamber, where highly energetic flows have to be managed ensuring the safe operation of the thrust chamber and of the entire engine. Different technological solutions to handle such flows are here investigated by means of CFD numerical simulations. As a compromise between details and computational cost, the attention is focused on capturing the basic phenomena involved which drive the main heat transfer processes, to allow full scale engine analysis as support to the engine design phase. The simplified approaches are defined, verified and validated against experimental data in different rocket engine conditions, such as film cooled and regeneratively cooled thrust chambers, and expander cycle engine thrust chambers with heat transfer enhancement devices. Hence, parametric analyses are finally carried out for each configuration. Finally, the simplified approaches are adopted in the thermal analysis of the LM-10 MIRA oxygen/methane expander cycle engine thrust chamber.

Contents

1

Introduction

Liquid rocket engines are employed as a propulsion solution in a wide range of missions: from boosters and upper stages in launchers to in-space propulsion and attitude control on spacecrafts. This wide variety of performance can be covered by means of different propellants, different propellant pressurizing techniques and different engine cycles. For each mission, different requirements have to be fulfilled, but some peculiar problems must be faced in all the applications. In particular, recalling the base physical phenomena involved in producing thrust by means of chemical rockets, the chemical energy of the propellants is converted into kinetic energy in two steps: combustion or chemical decomposition of the propellants inside the combustion chamber and expansion of combustion products inside the nozzle. To improve the engine performance, which can be expressed in terms of specific impulse, the combustion process inside the chamber should be near the chemical equilibrium, and the flow at the end of the expansion through the nozzle should approach the ambient pressure outside the nozzle. Focusing on the first step, the main goal is to reach the higher temperature of the products inside the chamber which can be achieved with high residence time in the chamber and mixture ratio near the stoichiometric mixture ratio together with low molecular weight of the products. Hence, thermal control is one of the most challenging task to face in a high performance liquid rocket engine. Different solutions can be adopted depending on the mission assigned to the engine. In this work, the heat transfer properties of high thrust liquid rocket engines are of interest, with particular attention to those operated with the oxygen/methane propellant combination. Different thermal control solutions are investigated with the aim of identifying and analyzing the main phenomena involved and provide simplified and accurate analysis methods to support the system design phase.

Oxygen/methane propellant combination

Most of the current rocket engines utilize hydrogen, kerosene, or storable fuels such as hydrazine. In the recent past, oxygen/methane propellant combination has gained interest in the study of new generation propulsion systems for liquid booster stages, upper stages and in-orbit transfer stages. In Figs. 1.1(a) and 1.1(b), specific impulse in vacuum and bulk density are plotted against the oxidizer to fuel mass ratio (O/F) for four propellant combinations: oxygen/hydrogen (O_2/H_2), oxygen/methane (O_2/CH_4),

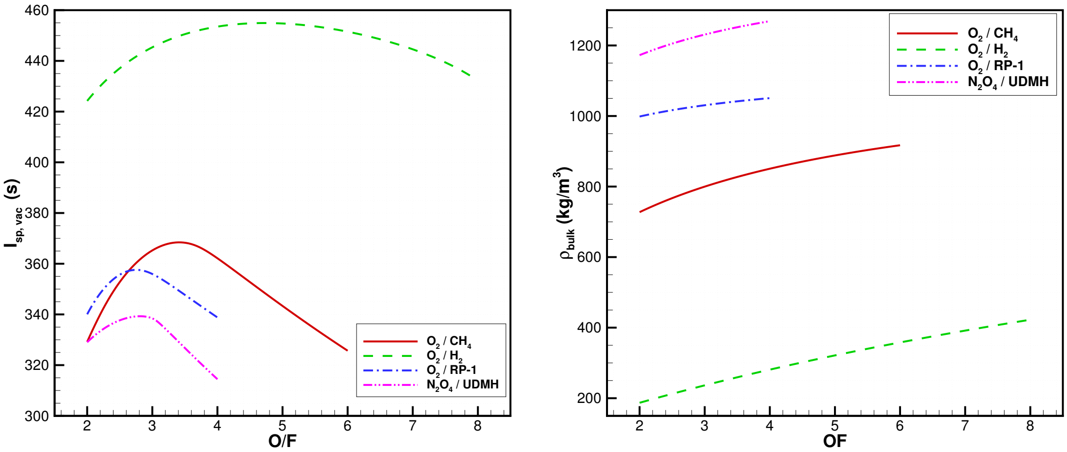

(a) Specific impulse in vacuum (p_c=68.95 bar, ε=40)

(b) Bulk density at tank conditions

Figure 1.1: Performance comparison between propellant combinations.

oxygen/kerosene (O_2/RP-1) and nitrogen tetroxyde / unsymmetrical dimethylhydrazine (N_2O_4/UDMH). The first two are cryogenic propellants, the third is composed by a cryogenic oxidant and a storable fuel and the last are both storable propellants. Specific impulse in vacuum is evaluated for a standard nozzle with chamber pressure 68.95 bar and area ratio 40. The bulk density is defined as:

$$\rho_{bulk} = \frac{1 + O/F}{\dfrac{1}{\rho_{fuel}} + \dfrac{O/F}{\rho_{ox}}}$$

is evaluated from the propellant densities in tank conditions which are the vaporization temperature for cryogenic propellants and ambient temperature for storable propellants. Oxygen/methane provides better performance compared to storable propellant combination and oxygen with other hydrocarbons, but it still gives poorer performance than oxygen/hydrogen. Compared to other hydrocarbon fuels, such as kerosene (RP-1), it has lower density and gives higher performance when associated to liquid oxygen. Moreover, it is characterized by less soot and coke deposition in the thrust chamber and inside the cooling channels, respectively. Despite its lower specific impulse compared to liquid hydrogen, liquid methane is favored by higher density, warmer liquid temperature and lower flammability limit. In particular, its higher density significantly reduces the volumes needed for the tanks and its warmer liquid temperature makes it a “space storable propellant”. Moreover, it is not dangerous for human health unlike storable propellants which need specific safety procedures to be handled during on ground and on board operations. For these reasons, it is often considered as a “green propellant”. Methane is also an interesting fuel for dual-fuel engines able to operate either with hydrogen or methane with little losses in terms of performance [1]. This capability can facilitate the use of in-situ propellant systems for space exploration applications. In this framework, oxygen/methane can be considered a good compromise able to combine good performance and low cost handling processes.

Because of these advantages, oxygen/methane liquid rocket engines represent promising solutions in the present liquid rocket engine research panorama all around the world. Many international research programs include oxygen/methane propellant combination in their schedule focusing on different aspects. In Europe, the Future Launcher Preparatory Programme (FLPP), supported by ESA, encloses feasibility studies about oxygen/methane high thrust engine for liquid booster stages [2, 3]. Basic knowledge about oxygen/methane combustion, heat transfer processes and cooling methods are investigated in the frame of the In-Space Propulsion 1 (ISP1) program included in the the European 7^{th} Framework [4]. In Italy oxygen/methane upper stages and in-orbit transfer stages are part of the ASI's LYRA Program to assess Vega launcher possible evolution [5]. Moreover, ASI supports the HYPROB program which includes basic research and system and technology demonstrators of oxygen/methane liquid rocket engine. In Germany, in view of a next generation launcher (NGL) vehicle development, industries and research centers were involved in complementary technology efforts to investigate key-enabling hydrocarbon technologies focusing on engine combustion devices [6]. To investigate oxygen/methane combustion features as a candidate propellant combination for reusable launch vehicles, French combustion facility MASCOTTE was upgraded to operate with oxygen/methane [7].

Thanks to their experience in LOX/hydrocarbon liquid rocket engines, Russian industries have been involved in international research programs together with Germany in the TEHORA program [8] and with Italy in the LYRA program [5].

In USA, in the late 90's oxygen/methane propellant combination has been of interest for low-cost small launchers and lunar or Mars missions. In that framework, the main idea was to rely on a robust and proven design and evaluate which component should be modified/re-designed to operate with oxygen/methane [9, 10]. Basic research has been conducted by universities focusing on single system components such as single injector elements [11, 12]. Recently, NASA's Propulsion and Cryogenic Advanced Development (PCAD) project supported the design and development of a oxygen/methane integrated propulsion test bed to study system steady state and transient performance, operational characteristics, and validate fluid and thermal models for an oxygen/methane propulsion system [13].

In Japan, oxygen/methane propellant combination has been studied to achieve diversity and flexibility for next generation space propulsion systems. JAXA's studies start from simpler engine systems to more complex configurations with the goal to minimize the development risk and the time to get the methane technology [14][15].

Thrust chamber thermal control

The thrust chamber is the key assembly of a liquid rocket engine. Its main function is to generate thrust by converting propellant chemical energy into kinetic energy. This goal is accomplished by liquid propellant injection, atomization, vaporization, mixing,

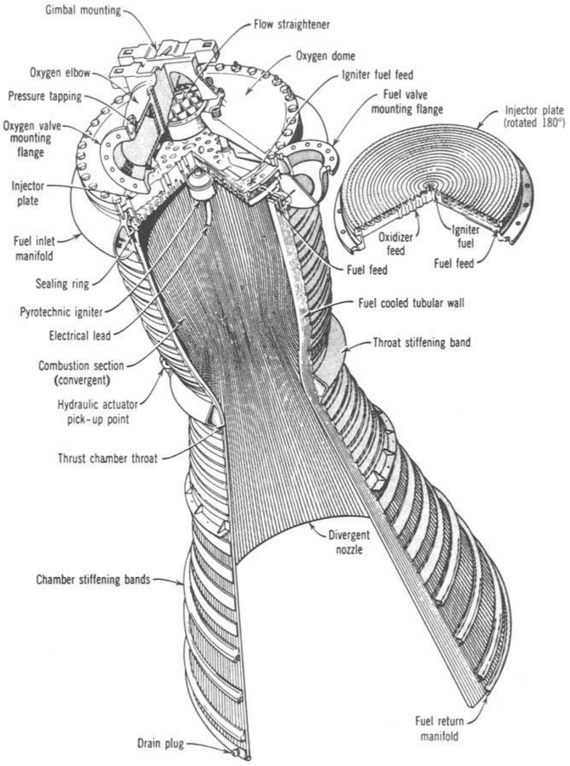

Figure 1.2: Example of thrust chamber assembly [16]

and combustion obtaining hot combustion products, which are accelerated and ejected at high velocity through the nozzle.

A rocket thrust chamber assembly is mainly composed by injectors mounted on the injector plate, a combustion chamber and a supersonic nozzle (see Fig. 1.2). All these components have to withstand the high temperatures (above 3000 K) and heat fluxes (from 10 to 100 MW/m^2) produced by combustion [16]. Inside the combustion chamber, combustion product temperature exceeds by far melting points of most chamber wall materials. If heat transfer is too high and wall temperature raises locally, the thrust chamber will fail. The largest part of the heat is transferred by means of convection. The amount of heat transferred by radiation can vary from 5% to 35% depending on the propellant combination and the chamber volume. The maximum heat flux is located just upstream of the throat of the nozzle. As a consequence, all thrust chambers, whose operative life exceeds the maximum time the material can withstand these high thermal stresses, need cooling systems.

Cooling methods can be either active or passive [17]: the first approach consists in actively controlling heat transfer by means of coolant fluids; the second relies on flow and material properties.

Medium to high thrust engines rely on active cooling such as regenerative cooling, film cooling and transpiration cooling. Regenerative cooling consists in convectively cool the wall by flowing coolant inside channels surrounding the chamber. Film cooling provides protection to the chamber wall by injecting a thin film of coolant parallel to the wall. It is usually associated to regenerative cooling to locally control wall temperature in critical regions such as chamber wall near the injector plate and the nozzle throat. Furthermore, it can be employed in uncooled walls to locally relief the wall from high heat fluxes such as film cooling in the divergent part of the nozzle. Transpiration cooling consists in injecting gaseous or liquid coolant through a porous material inside the thrust chamber and is particularly suitable for the injector plate cooling of high thrust engines.

Passive cooling techniques include radiation cooling, ablative cooling and heat sink cooling. Radiation cooling is a steady state cooling method characterized by the establishment of thermal equilibrium between hot gas flow and wall materials which radiate heat away to the surrounding or to vacuum. It is generally used for low heat transfer rates occurring in thrust chamber of low thrust engines or in the diverging part of the nozzle in high thrust engines. Ablative cooling is realized by absorbing heat in an inner liner made of ablative materials. Heat sink cooling relies on wall material heat capacity and it is widely employed in ground experimental facilities, where weight and volumes are not a constraint for the design and heat capacity can be increased by means of thick walls to extend the maximum experiment duration. Heat sink cooling is also employed for low thrust engines which operate for short time, such as attitude control systems.

High performance liquid rocket engines require optimized and reliable cooling systems. Thermal control becomes more challenging in the case of an expander cycle engine when the entire engine performance depends on the cooling system performance. In this specific cycle, the thrust chamber has to provide the required heat pick-up for operating the fuel and oxidizer turbo-machinery. Consequently, heat loading and cooling should be in an optimal balance to reduce the thrust chamber mass while maximizing overall engine performance. From the hot-gas side point of view, it can be important to enhance the heat transfer to the coolant depending on engine dimension and coolant properties. Heat transfer enhancement can be achieved with several design options which lead to an increase of the chamber surface: increasing chamber length and increasing chamber perimeter. The first option has been adopted in the VINCI engine [18] and consists in lengthening the thrust chamber cylindrical section and consequently increasing cooling channel length. This solution leads to increasing the integral heat transfer from the hot gas side to the coolant but has to face increasing pressure drop in the cooling channels due to friction. Moreover, the increase of the engine global length is one of the main drawbacks of the present option recalling that expander cycle engines are employed as upper stage engines which have to fulfill stringent overall dimension constrains. The increasing perimeter design option can be achieved by means of a tubular wall design as in the RL-10 [19] or by axial ribs on the hot gas side walls as in the RD0146 [20]. The first is a result of the thrust chamber manufacturing technique which consists in tubular copper or steel cooling channels brazed together to shape the thrust chamber (see Fig. 1.3(a)). Hence the inner thrust chamber profile is not smooth but is composed by the exposed arc of the cooling tubes. The second option consists in axial ribs, with rectangular or trapezoidal

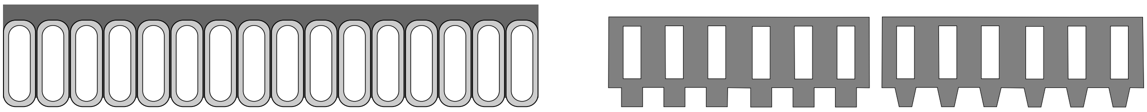

(a) Tubular wall section (b) Ribbed wall section

Figure 1.3: Increasing perimeter design options.

sections, placed in the inner thrust chamber wall in correspondence of the base of the cooling channels (see Fig. 1.3(b)).

Objectives

In this work, the main goal is to study the flow field and heat transfer characteristics in oxygen/methane liquid rocket engine thrust chambers by means of simplified approached as a compromise between detailed analysis and low cost numerical simulations. Different applications are investigated to highlight the capability of the simplified approaches to support engineering studies of liquid rocket engine thrust chamber thermal loads.

An in-house three dimensional finite volume Reynolds Averaged Navier-Stokes (RANS) equations solver able to treat mixtures of thermally perfect gases is described in Part I. The multi-species feature and the thermodynamic and transport properties treatment are validated comparing numerical solutions and available experimental data for three different test cases whose details are described in Ch. 4: a supersonic nozzle operated with hot air where wall temperature and wall heat fluxes are available, air/air film cooling along an adiabatic flat plate where film cooling efficiency is evaluated and helium/air supersonic mixing layer where helium mass fraction is measured to trace the mixing layer spreading rate.

In Part II, liquid rocket engine thrust chamber heat transfer features in different configurations are analyzed in details. Simplified approaches to study each problem are presented and validated against experimental data and then applied to perform parametric analysis of the main properties.

Film cooled thrust chamber characteristics are discussed in Ch. 5 by means of a simplified approach where near injector plate phenomena are neglected and equilibrium combustion products are injected matching the main geometrical characteristics of the injector plate. The approach is validated comparing the wall heat flux along the chamber against experimental data for an oxygen/hydrogen sub-scale thrust chamber. Then, this approach is adopted to perform a parametric analysis on a film cooled oxygen/methane subscale thrust chamber in the frame of the ISP1 project.

Regeneratively cooled thrust chambers are studied in Ch. 6 by means of a loose coupling technique to capture the heat transfer balance between hot-gas side, wall and coolant side heat transfer. The main goal of this study is to assess the capability of a simplified approach to evaluate the thermal environment in regeneratively cooled thrust chambers.

Flow field and heat transfer enhancement due to ribbed walls are analyzed in Ch. 7 focusing on expander cycle engine thrust chamber like configurations. The capability of the solver to capture heat transfer enhancement in this configuration is validated reproducing an experimental test case where hot air flows inside a test chamber with different rib configurations and heat transfer is measured as the increase in water coolant temperature. Then, a parametric analysis is performed over rib height to evaluate its effects on the flow field and heat transfer.

Finally, in Ch. 8 the thermal analysis of the LM-10 MIRA full scale expander cycle engine thrust chamber operated with oxygen/methane propellant combination is performed taking advantage of the simplified approaches discussed.

I

Model

2

Governing equations

Liquid rocket engine thrust chambers are characterized by three-dimensional turbulent flows involving mixtures of hot gases coming from the combustion of oxidizer and fuel at high pressure. Many complex phenomena take place in the thrust chamber: injection, atomization, vaporization, combustion are confined near the injector plate, then combustion products are accelerated through the nozzle. Focusing on the thrust chamber heat load analysis, in the present study near injector plate phenomena are neglected and the flow of the mixture composed by equilibrium combustion products is assumed frozen, along the chamber toward the nozzle.

Due to the strong temperature gradients inside the chamber, the dependence on temperature of thermodynamic and transport properties of the combustion products mixture cannot be neglected. Moreover, in case of active cooling technique in the hot gas side of the thrust chamber, mixing of different species may occur.

To capture these features, the considered governing equations are the Navier-Stokes equations for a mixture of $\mathcal{N}$ species whose thermodynamic and transport properties vary with temperature i.e. mixture of thermally perfect gas. In particular, momentum equation is considered together with $\mathcal{N}$ species continuity equations to treat mixture of gases and energy equation including the energy transport due to molecular diffusion [21].

The flow inside the thrust chamber is fully turbulent due to the large Reynolds number involved. The turbulent flow has been modeled by means of Reynolds Averaged Navier-Stokes (RANS) equations. The Spalart-Allmaras one equation turbulence model [22] is adopted to close the set of equations.

2.1 Governing equations

The integral form of the governing equations derives directly from the physical principles that describe the behavior of a moving fluid:

- mass continuity;
- momentum balance;
- conservation of energy.

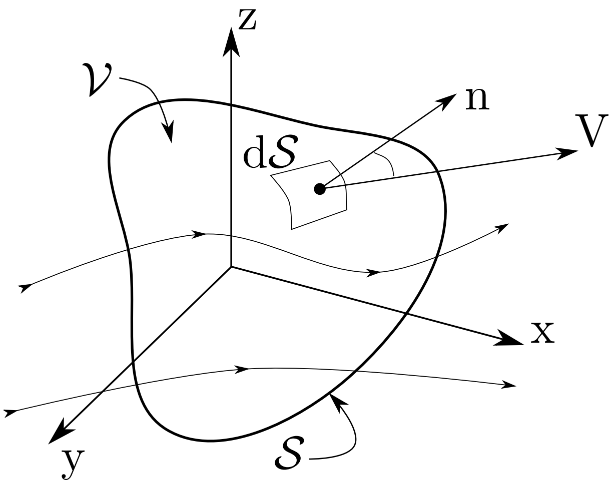

Figure 2.1: Fixed finite control volume.

In case of a mixture of $\mathcal{N}$ gases, mass continuity is the sum of the $\mathcal{N}$ species transport equations.

The conservation laws apply to a fixed finite control volume characterized by its volume $\mathcal{V}$ and a control surface $\mathcal{S}$ as sketched in Fig. 2.1.

2.1.1 Species continuity

The conservation of mass principle states that the net time rate of change of the mass of species s inside the control volume is due to the net flux of species s through the surface and the creation or extinction of species s inside the control volume due to chemical reactions.

$$\frac{d}{dt}\int_{\mathcal{V}} \rho_s \, d\mathcal{V} = -\oint_{\mathcal{S}} \rho_s \boldsymbol{v}_s \, d\mathcal{S} + \int_{\mathcal{V}} \dot{w}_s \, d\mathcal{V} \tag{2.1}$$

where ρ_s is the density of species s, $\boldsymbol{v}_s$ is the mass motion velocity of species s and $\dot{w}_s$ is the local rate of change of ρ_s due to chemical reactions inside the control volume. In particular, $\boldsymbol{v}_s$ can be written as the sum of the velocity of the mixture and the diffusion velocity of each species s: $\boldsymbol{v}_s = \boldsymbol{v} + \boldsymbol{u}_s$.

$$\frac{d}{dt}\int_{\mathcal{V}} \rho_s \, d\mathcal{V} + \oint_{\mathcal{S}} \rho_s \boldsymbol{v} \cdot \boldsymbol{n} d\mathcal{S} = -\oint_{\mathcal{S}} \rho_s \boldsymbol{u}_s d\mathcal{S} + \int_{\mathcal{V}} \dot{w}_s d\mathcal{V} \tag{2.2}$$

Using the definition of mixture density as the sum of each species density:

$$\rho = \sum_{s=1}^{\mathcal{N}} \rho_s \tag{2.3}$$

summing the continuity equations of all species $\mathcal{N}$, the sum of $\dot{w}_s$ is zero:

$$\sum_{s=1}^{\mathcal{N}} \dot{w}_s = 0$$

and the diffusion velocity contribution relevant to each species must sum zero:

$$\sum_{s=1}^{\mathcal{N}} \rho_s \boldsymbol{u}_s = 0 \tag{2.4}$$

2.1.2 Momentum balance

The momentum balance principle states that the momentum variation in time of a fluid element is equal to the total force acting on the volume $\mathcal{V}$ and on the surface $\mathcal{S}$, that is:

$$\frac{d}{dt}\int_{\mathcal{V}} \rho\, \boldsymbol{v}\, d\mathcal{V} + \oint_{\mathcal{S}} (\rho \boldsymbol{v} \cdot \boldsymbol{n}) \boldsymbol{v} d\mathcal{S} = \int_{\mathcal{V}} \rho\, \boldsymbol{f}\, d\mathcal{V} + \oint_{\mathcal{S}} \boldsymbol{t}\, d\mathcal{S} \tag{2.5}$$

The first term on the right hand side represents the sum of the forces acting on the volume $\mathcal{V}$ ($\boldsymbol{f}$ is the volumetric force per unit mass) while the second term is the sum of the forces acting on the external surface $\mathcal{S}$ ($\boldsymbol{t}$ is the surface force per unit area).

The i-th component of vector $\boldsymbol{t}$ can be expressed as a function of the stress tensor σ_{ij}:

$$t_i = \sigma_{ij}\, n_j$$

where n_j is the j-th component of the vector $\boldsymbol{n}$, that is the unit vector orthogonal to the surface $\mathcal{S}$ and it is considered positive as it is outward-facing the volume $\mathcal{V}$. The stress tensor can be decomposed into two parts: the spherical tensor (based on the pressure p) and the viscous stress tensor τ_{ij}:

$$\sigma_{ij} = -p\, \delta_{ij} + \tau_{ij} \tag{2.6}$$

where $\delta_{ij} = 0$ if $i \neq j$ and $\delta_{ij} = 1$ if $i = j$. In case of Newtonian fluid, the viscous stress tensor can be expressed by assuming the Stokes hypothesis for the viscosity coefficient:

$$\tau_{ij} = \mu \left(\frac{\partial v_i}{\partial x_j} + \frac{\partial v_j}{\partial x_i} - \frac{2}{3} \frac{\partial v_k}{\partial x_k} \delta_{ij} \right) \tag{2.7}$$

where v_i is the i-th component of the mixture velocity $\boldsymbol{v}$, x_i is the i-th orthogonal axis, μ is the dynamic viscosity of the mixture.

2.1.3 Conservation of energy

The conservation of energy principle states that the total energy variation in time of a fluid element is equal to the heat transfer rate entering through the surface $\mathcal{S}$ and the total work made by the forces acting on the volume $\mathcal{V}$ and on the surface $\mathcal{S}$, that is:

$$\frac{d}{dt}\int_{\mathcal{V}} \left(e + \frac{\boldsymbol{v}^2}{2} \right) \rho\, d\mathcal{V} + \oint_{\mathcal{S}} \left(e + \frac{\boldsymbol{v}^2}{2} \right) \rho \boldsymbol{v} \cdot \boldsymbol{n}\, d\mathcal{S} = \int_{\mathcal{V}} \rho (\boldsymbol{f} \cdot \boldsymbol{v})\, d\mathcal{V} + \oint_{\mathcal{S}} (\boldsymbol{t} \cdot \boldsymbol{v})\, d\mathcal{S} - \oint_{\mathcal{S}} \boldsymbol{q} \cdot \boldsymbol{n}\, d\mathcal{S} \tag{2.8}$$

where the total energy per unit volume is: $E = \rho\left(e + \frac{1}{2}v_j\, v_j\right)$; e is the specific internal energy and $\boldsymbol{q}$ is the vector of heat flux, considered positive as it is outward-facing the volume $\mathcal{V}$.

The heat flux is composed by the conductive heat flux related to the temperature gradient using the Fourier's law and the energy flux caused by diffusion of all species. In the present analysis, radiative heat flux is not modeled and it is not taken into account in the heat flux evaluation.

$$\boldsymbol{q} = \boldsymbol{q}_c + \boldsymbol{q}_d \tag{2.9}$$

$$q_j = -k\frac{\partial T}{\partial x_j} + \sum_{s=1}^{\mathcal{N}} \rho_s u_{s,j} h_s \tag{2.10}$$

where k is the thermal conductivity of the mixture, $u_{s,j}$ is the j-th component of the diffusion velocity $\boldsymbol{u}_s$ of species s and h_s is the absolute enthalpy of species s per unit mass of s.

2.2 Vectorial form of the conservation laws

Species continuity, momentum and energy equations can be written in a compact, vectorial form:

$$\frac{d}{dt}\int_{\mathcal{V}} \boldsymbol{U}\, d\mathcal{V} + \oint_{\mathcal{S}} \boldsymbol{F_j}\, n_j\, d\mathcal{S} = \int_{\mathcal{V}} \boldsymbol{Q}\, d\mathcal{V} + \oint_{\mathcal{S}} \boldsymbol{G_j}\, n_j\, d\mathcal{S} \tag{2.11}$$

where the vector $\boldsymbol{F_j}$ is defined by:

$$\boldsymbol{F_j} = \boldsymbol{U} v_j + \boldsymbol{P_j}$$

where $\boldsymbol{U}$ is the vector of conserved variables, $\boldsymbol{F_j}$ is the vector of the Eulerian fluxes, $\boldsymbol{G_j}$ is the vector of viscous fluxes and $\boldsymbol{Q}$ is the vector of external forces and chemical sources (source terms).

$$\boldsymbol{U} = \begin{pmatrix} \rho_1 \\ \vdots \\ \rho_{\mathcal{N}} \\ \rho v_i \\ E \end{pmatrix}, \quad \boldsymbol{P_j} = \begin{pmatrix} 0 \\ \vdots \\ 0 \\ p\delta_{ij} \\ p v_j \end{pmatrix}, \tag{2.12}$$

$$\boldsymbol{Q} = \begin{pmatrix} \dot{w}_1 \\ \vdots \\ \dot{w}_{\mathcal{N}} \\ \rho f_i \\ \rho f_j v_j \end{pmatrix} \quad \text{and} \quad \boldsymbol{G_j} = \begin{pmatrix} 0 \\ \vdots \\ 0 \\ \tau_{ij} \\ \tau_{ij} v_i + k\dfrac{\partial T}{\partial x_j} + \displaystyle\sum_{s=1}^{\mathcal{N}} \rho_s u_{s,j} h_s \end{pmatrix} \tag{2.13}$$

Since only multi-species non-reacting mixtures are of interest in this study and since volumetric external forces (such as gravity) can be neglected for the present applications, the vector $\boldsymbol{Q}$ will be assumed null hereafter.

The variables ρ_s, ρv_i, and E are called conserved variables because they originate from the conservation laws (i.e. integral governing equation).

The vectorial equation Eq. (2.11) is composed by $\mathcal{N}+1$ scalar equations ($\mathcal{N}$ species mass and energy) and one vectorial equation (momentum) while it depends on $6+2\mathcal{N}$ scalar variables (ρ_s, ρ, p, T, e, μ, k, h_s) and $\mathcal{N}+1$ vectorial variables ($\boldsymbol{u}_s$, $\boldsymbol{v}$). Thus $4\mathcal{N}+5$ fluid property relations must be added to close the system of equations:

- definition of mixture density (1)
- equation of state (1)
- energy equation of state (1)
- mixture viscosity (1)
- mixture thermal conductivity (1)
- species diffusion velocity model ($3\mathcal{N}$)
- species absolute enthalpy model ($\mathcal{N}$)

Note that the multi-component mixture problem can be closed in two ways: solving $\mathcal{N}-1$ transport equations for $\mathcal{N}-1$ species and the mixture continuity equation (Eq. 2.1) or solving $\mathcal{N}$ transport equations for $\mathcal{N}$ species. In the first solving method, the $\mathcal{N}^{th}$ species continuity is not explicitly resolved and its partial density is evaluated from the $\mathcal{N}-1$ species density and the mixture density from Eq. (2.3).

2.3 Thermodynamic model

In the following, the equation of state will be defined for the mixture. Then absolute enthalpy and internal energy will be derived in the case of mixture of thermally perfect gases. Finally, the speed of sound and the practical thermodynamic models adopted in the numerical simulations will be discussed.

2.3.1 Equation of state

Perfect gas equation of state is adopted to relate pressure and temperature.

$$p = \rho \mathcal{R} T \tag{2.14}$$

Mixture composition can be expressed in terms of mass fraction, which is the ratio between species density and mixture density, and mole fraction, that is the ratio between number of moles of species s per mole of mixture:

$$y_s = \frac{\rho_s}{\rho} \quad , \quad X_s = \frac{N_s}{N}$$

The relation between mass fractions and mole fractions depends on the ratio between the molecular weight of the species s and the molecular weight of the mixture:

$$y_s = \frac{\rho_s}{\rho} = \frac{N_s}{N} \frac{\mathcal{M}_s}{\mathcal{M}} = \frac{\mathcal{M}_s}{\mathcal{M}} X_s$$

$\mathcal{R}$ is the mixture gas constant defined as the ratio between the universal gas constant $\mathscr{R}$ and the mixture molecular weight $\mathcal{M}$:

$$\mathcal{R} = \frac{\mathscr{R}}{\mathcal{M}} \tag{2.15}$$

Mixture gas constant can be obtained by summation of each species gas constant:

$$\mathcal{R} = \sum_{s=1}^{\mathcal{N}} y_s \mathcal{R}_s \quad \text{where} \quad \mathcal{R}_s = \frac{\mathscr{R}}{\mathcal{M}_s} \tag{2.16}$$

where $\mathcal{M}_s$ is the molecular weight of the s-th species. Comparing Eqs. (2.15) and (2.16), the molecular weight of the mixture can be expressed in terms of each species molecular weight as follows:

$$\mathcal{R} = \frac{\mathscr{R}}{\mathcal{M}} = \sum_{s=1}^{\mathcal{N}} y_s \frac{\mathscr{R}}{\mathcal{M}_s} \quad \rightarrow \quad \mathcal{M} = \frac{1}{\displaystyle\sum_{s=1}^{\mathcal{N}} \frac{y_s}{\mathcal{M}_s}} \tag{2.17}$$

2.3.2 Enthalpy

Absolute enthalpy of species s can be written as the sum of the sensible enthalpy of species s and its formation enthalpy.

$$h_s = h_{s,sens} + \left(\Delta h_f\right)_s^{T_{ref}} \tag{2.18}$$

where $\left(\Delta h_f\right)_s^{T_{ref}}$ is the heat of formation of species s at $T = T_{ref}$ and the sensible enthalpy is the enthalpy measured above the reference temperature T_{ref}. In case of local thermodynamic equilibrium, the sensible enthalpy can be written as:

$$c_{p,s} = \left(\frac{dh_s}{dT}\right)_{p=const} \qquad \text{and} \qquad h_{s,sens} = \int_{T_{ref}}^{T} c_{p,s}(\tau)\, d\tau \tag{2.19}$$

Then absolute enthalpy of species s can be defined as a function of the temperature in terms of a specific heat:

$$h_s = \int_{T_{ref}}^{T} c_{p,s}(\tau)\, d\tau + \left(\Delta h_f\right)_s^{T_{ref}} \tag{2.20}$$

The evaluation of the absolute enthalpy of species s is described in Sec. 2.3.4. Mixture absolute enthalpy is obtained by summation of species absolute enthalpy:

$$h = \sum_{s=1}^{\mathcal{N}} y_s\, h_s = \sum_{s=1}^{\mathcal{N}} y_s\, h_{s,sens} + \sum_{s=1}^{\mathcal{N}} y_s\, \left(\Delta h_f\right)_s^{T_{ref}} \tag{2.21}$$

2.3.3 Internal energy

Internal energy of species s can be written as a function of the temperature in terms of specific heat at constant volume:

$$e_s = \int_{T_{ref}}^{T} c_{v,s}(\tau)\, d\tau + \left(\Delta h_f\right)_s^{T_{ref}} \quad , \quad c_{v,s} = \left(\frac{de_s}{dT}\right)_{v=const} \tag{2.22}$$

where $c_{v,s}$ is the specific heat for species s. For a mixture composed by $\mathcal{N}$ species, the internal energy per unit mass may be written as:

$$e = \sum_{s=1}^{\mathcal{N}} y_s\, e_s \tag{2.23}$$

It is convenient to define the mixture specific heats as:

$$c_v = \sum_{s=1}^{\mathcal{N}} y_s\, c_{v,s} \quad , \quad c_p = \sum_{s=1}^{\mathcal{N}} y_s\, c_{p,s} \tag{2.24}$$

and the mixture gas constant as:

$$\mathcal{R} = \sum_{s=1}^{\mathcal{N}} y_s \mathcal{R}_s = c_p - c_v \tag{2.25}$$

Finally the ratio between mixture specific heats reads:

$$\gamma = \frac{c_p}{c_v} \tag{2.26}$$

Internal energy can be related to the absolute enthalpy recalling its definition and applying Eq. 2.21:

$$e = h - \frac{p}{\rho} = \sum_{s=1}^{\mathcal{N}} y_s\, h_s - \frac{p}{\rho} = \sum_{s=1}^{\mathcal{N}} y_s \left[\int_{T_{ref}}^{T} c_{p,s}(\tau)\ d\tau + \left(\Delta h_f\right)_s^{T_{ref}} \right] - \frac{p}{\rho} \tag{2.27}$$

2.3.4 Mathematical model

In the numerical simulations, thermodynamic properties of thermally perfect gases are treated by means of lookup tables. These tables are arranged in terms of species s and temperature and collects all the thermodynamic properties of each species of the mixture in a range of temperature. Thermodynamic properties such as absolute enthalpy, entropy and specific heat at constant pressure are evaluated starting from the thermodynamic database of the “Chemical Equilibrium and Applications” (CEA) program [23] which relies on NASA polynomial form. It consists in seven terms for the specific heat at constant pressure and corresponding terms for enthalpy and entropy together with their integration constants. For each chemical species the thermodynamic functions (specific heat, enthalpy, and entropy) as functions of temperature are given in the form of least-square coefficients whose general form is as follows:

$$\frac{C^0_{p,s}}{\mathscr{R}} = \sum a_i T^{q_i} \quad , \quad \frac{H^0_s}{\mathscr{R}T} = \frac{\int C^0_{p,s}\, dT}{\mathscr{R}\ T} \quad , \quad \frac{S^0_s}{\mathscr{R}} = \int \frac{C^0_{p,s}}{\mathscr{R}\ T} dT \tag{2.28}$$

Generally the three functions $C^0_{p,s}/\mathscr{R}$, $H^0_s/(\mathscr{R}T)$ and $S^0_s/\mathscr{R}$ are fit simultaneously, with the fit constrained at $T = 298.15\ K$. Thus the least-squares coefficients reproduce heats of formation at $T = 298.15\ K$ exactly.

2.4 Transport properties

In the governing partial differential equations derived in Sec. 2.1, the vector of viscous fluxes ($\boldsymbol{G}$) accounts for transport of mass, momentum and energy. In the viscous fluxes evaluation, diffusion induced by temperature, pressure and body forces is neglected, and only molecular diffusion related to species concentration gradients is modeled [24]. In the following sections, viscosity and thermal conductivity models and molecular diffusion treatment will be discussed.

2.4.1 Viscosity

For a multi-component gas, the mixture values of the viscosity coefficient are usually evaluated with the Wilke's semi-empirical rule [24] obtained on the basis of the kinetic theory and several simplifying assumptions. In particular, the mixture value of viscosity can be evaluated from the values of viscosity of each of the species s (μ_s) by means of mixture rules:

$$\mu = \sum_{s=1}^{\mathcal{N}} \frac{X_s \mu_s}{\sum_j X_j \phi_{sj}}, \quad \phi_{sj} = \frac{1}{\sqrt{8}} \left(1 + \frac{\mathcal{M}_s}{\mathcal{M}_j}\right)^{-1/2} \left[1 + \sqrt{\frac{\mu_s}{\mu_j}} \left(\frac{\mathcal{M}_j}{\mathcal{M}_s}\right)^{1/4}\right]^2 \tag{2.29}$$

where X_s is the mole fraction of species s. To evaluate mixture viscosity, viscosity for each species s has to be quantified. In this study, they are evaluated as described in Sec. 2.4.4.

2.4.2 Thermal conductivity

Mixture thermal conductivity can be evaluated assuming a constant Prandtl number which is the ratio between viscous diffusion and thermal diffusion. This simplified approach is valid in a wide range of physical conditions, so that k can be evaluated from:

$$k = \frac{\mu c_p}{Pr}\ , \quad Pr = constant \tag{2.30}$$

whose constant value depends on the gas (for air and other gases $Pr = 0.7$ [24]). This model avoids the determination of species thermal conductivities.

To take into account for the multi-component nature of the mixture, similarly to viscosity, thermal conductivity of the mixture can be evaluated from thermal conductivity of the chemical species s by means of Wilke's mixture rules [21]:

$$k = \sum_{s=1}^{\mathcal{N}} \frac{X_s k_s}{\sum_j X_j \phi_{sj}}, \quad \phi_{sj} = \frac{1}{\sqrt{8}}\left(1 + \frac{\mathcal{M}_s}{\mathcal{M}_j}\right)^{-1/2}\left[1 + \sqrt{\frac{\mu_s}{\mu_j}}\left(\frac{\mathcal{M}_j}{\mathcal{M}_s}\right)^{1/4}\right]^2 \tag{2.31}$$

where ϕ_{sj} coefficients are the same of Eq. 2.29. As for the species viscosity, thermal conductivity for each species is evaluated as described in Sec. 2.4.4.

2.4.3 Molecular diffusion

Molecular diffusion is a physical phenomenon that arises mostly because of the presence of gradients of mass or mole concentrations in the mixture. Although pressure and temperature gradients as well as the effect of body forces can influence diffusion, for a simple analysis these dependencies are often neglected. For a binary mixture of species i and j, the mass flux of species i can be written by the Fick's Law [24]:

$$\rho_i \boldsymbol{u}_i = -\rho \mathcal{D}_{ij} \nabla y_i \tag{2.32}$$

where $\mathcal{D}_{ij}$ is the binary diffusion coefficient. For binary mixtures, the binary diffusion coefficient can be evaluated as follows [25]:

$$\rho \mathcal{D}_{ij} = 7.1613 \times 10^{-25} \frac{\mathcal{M}\sqrt{T\left(\frac{1}{\mathcal{M}_i} + \frac{1}{\mathcal{M}_j}\right)}}{\Omega_{ij}} \tag{2.33}$$

where Ω_{ij} are the collision cross section values function of temperature. Direct consequence of Eq. (2.33) are that binary diffusion coefficient is mutual and the self-diffusion coefficient is not null:

$$\mathcal{D}_{ji} = \mathcal{D}_{ij} \quad , \quad \mathcal{D}_{ii} \neq 0$$

For a gas with more than two species, a multicomponent diffusion coefficient must be used, denoted by $\mathcal{D}_{im}$ for the diffusion species i through the mixture. The multicomponent diffusion coefficient $\mathcal{D}_{im}$ is related to the binary diffusion coefficients $\mathcal{D}_{ij}$ defined in Eq. (2.33) by means of the approximate expression [26]:

$$\mathcal{D}_{im} = \frac{1 - X_i}{\sum_{j \neq i} X_j / \mathcal{D}_{ij}}$$

In the present study, assuming that all species i diffuse with the same velocity through the mixture, the diffusion is modeled by means of a unique diffusion coefficient for all the species, $\mathcal{D}$, evaluated assuming a constant Schmidt number:

$$\mathcal{D}_{im} = \mathcal{D} = \frac{\mu}{\rho\, Sc}, \quad Sc = constant \tag{2.34}$$

where Schmidt number is $Sc = 1$ that is a reasonable value for most gases [24].

2.4.4 Mathematical model

Similarly to thermodynamic properties, described in Sec. 2.3.4, transport properties can be expressed as a function of temperature. In particular, the data for each species are fitted to the following form:

$$\left.\begin{array}{l}\ln \mu_s\\ \ln k_s\end{array}\right\} = A \ln T + \frac{B}{T} + \frac{C}{T^2} + D \tag{2.35}$$

whose coefficients (A, B, C and D) are available for many species in the transport property database of CEA program [23].

2.5 Turbulence modeling

The turbulent flow is a flow regime which is characterized by strong, chaotic, non stationary and three-dimensional fluctuations, both in time and in space, of velocity, temperature, pressure, etc.

To correctly solve Eq. (2.11) capturing all scales, computational volumes must be proportional to $1/Re^3$. The flows of interest are characterized by high Reynolds number $\left(10^6\right)$ and to capture all scales of motion the volume dimension decreases dramatically with a consequent increase of volume number to discretize a given physical domain.

For this reason a turbulence model to describe the macroscopic effect of the "small" scales is generally adopted and the average main flow can be described by Eq. (2.11). This simplified approach consists in considering the generic variable ϕ as composed by two part: a mean value $\overline{\phi}$ and a fluctuation (in time) ϕ':

$$\phi = \overline{\phi} + \phi'$$

where

$$\overline{\phi}(t) = \frac{1}{T} \int_{-T/2}^{+T/2} \phi(t+\tau) d\tau$$

and time T is much bigger than the period of turbulent fluctuations. The above decomposition is called Reynolds average modeling and the averaged Eq. (2.11) are called Reynolds Averaged Navier Stokes (RANS) equations. In case of compressible flow the Favre decomposition is used:

$$\phi = \widetilde{\phi} + \phi''$$

where

$$\widetilde{\phi}(t) = \frac{\overline{\rho\phi}}{\overline{\phi}} = \frac{1}{T} \frac{1}{\overline{\rho}} \int_{-T/2}^{+T/2} \rho \, \phi(t+\tau) d\tau$$

where $\widetilde{\phi}$ is the average value and ϕ'' is the fluctuation. Using this decomposition on Eq. (2.11), the governing equations are called Favre Averaged Navier Stokes (FANS) equations [27]. These equations present additional terms in the momentum, energy and species continuity equation:

$$-\bar{\rho}\,\widetilde{v_i''v_j''} \quad , \quad \bar{\rho}\,\widetilde{v_j''h''}, \quad \bar{\rho}\,\widetilde{v_j''u_{s,j}''}$$

called Reynolds stress tensor and Reynolds fluxes, respectively. These terms represent the macroscopic effect of the turbulent fluctuations (v_i'', h'' and $u_{s,j}''$) which must be modeled using a proper turbulence model. Bussinesque supposed that the Reynolds turbulent terms can be related to the velocity and temperature gradients (as for the Newtonian-fluid law Eq. 2.7, the Fourier's law Eq. 2.10 and the Fick's law Eq. 2.32):

$$\begin{cases} -\ \bar{\rho}\,\widetilde{v_i''v_j''} & = & \mu_T\left(\dfrac{\partial\tilde{v}_i}{\partial x_j}+\dfrac{\partial\tilde{v}_j}{\partial x_i}\right) \\ \bar{\rho}\,\widetilde{v_j''h''} & = & -\ k_T\dfrac{\partial\tilde{T}}{\partial x_j}+\displaystyle\sum_{s=1}^{\mathcal{N}}\rho_s\widetilde{u_{s,j}h_s} \\ \bar{\rho}\,\widetilde{v_j''u_{s,j}''} & = & -\ \rho\mathcal{D}_T\dfrac{\partial\tilde{y}_s}{\partial x_j} \end{cases}$$

where μ_T, k_T and $\mathcal{D}_T$ are the turbulent dynamic viscosity, thermal conductivity and mass diffusion which can be related via the turbulent Prandtl number and Schmidt number:

$$Pr_T = \frac{\mu_T\, c_p}{k_T} \quad , \quad Sc_T = \frac{\mu_T}{\rho\mathcal{D}_T}$$

A reasonable value for Pr_T is 0.9. Turbulent Schmidt number may assume different values depending on the mixing layer configuration: for mixing layers between parallel streams $Sc_T = 0.7$ [28], for mixing layers between orthogonal streams $Sc_T = 0.2 - 0.3$ [29].

Note that turbulent Schmidt number values strongly depend on the flow configuration, thus variable turbulent Schmidt number models have been presented [30]. In these models, the constant value is replaced by an additional turbulent transport equation for the turbulent Schmidt number to be integrated together with the turbulent properties transport. In this work, the constant turbulent Schmidt number model is adopted being interested to flow configurations involving mixing of parallel streams ($Sc_T = 0.7$). Different turbulent diffusion models are compared in Sec. 4.3 reproducing a supersonic helium/air mixing layer.

Differently from the molecular properties (μ, k and $\mathcal{D}$), the turbulent dynamic viscosity, thermal conductivity and mass diffusion are not properties of the fluid, since they are related to the flow behavior and they can be much higher than the molecular properties: $\mu_T \gg \mu$, $k_T \gg k$ and $\mathcal{D}_T \gg \mathcal{D}$.

The turbulent property μ_T is evaluated by the Spalart-Allmaras [22] turbulence model while k_T and $\mathcal{D}_T$ are evaluated considering a constant value for Pr_T and Sc_T, respectively.

2.5.1 Spalart-Allmaras model

In the one-equation Spalart-Allmaras model [22] the kinematic turbulent viscosity $\nu_T = \mu_T/\rho$ is computed by a partial differential equation. In particular, this equation is a function of the intermediary variable $\widetilde{\nu}$ that is related to ν_T by:

$$\nu_T = \widetilde{\nu}\, f_{v1}(\chi)$$

where χ is the ratio between local and global kinematic viscosity, $\chi = \widetilde{\nu}/\nu$, and f_{v1} is a damping function:

$$f_{v1}(\chi) = \frac{\chi^3}{\chi^3 + c_{v1}^3}$$

The constant c_{v1} is set equal to 7.1. The partial differential equation that describes the behavior of the intermediary variable $\widetilde{\nu}$ is:

$$\frac{D\widetilde{\nu}}{Dt} = b_{prod}(S, \widetilde{\nu}, d) - b_{dest}(\widetilde{\nu}, d) + \frac{1}{\sigma}\left[\nabla \cdot ((\nu + \widetilde{\nu})\nabla\widetilde{\nu}) + c_{b2}\,(\nabla\widetilde{\nu})^2\right] \tag{2.36}$$

where S is the modulus of the vorticity, d is the distance from the wall and σ is set equal to 2/3. The last term of Eq. 2.36 is the diffusion term and the constant c_{b2} is calibrated to 0.662. The functions b_{prod} and b_{dest} describe the production and destruction of the turbulent viscosity, respectively. The production function is:

$$b_{prod} = c_{b1}\, \widetilde{S}\, \widetilde{\nu}$$

where

$$\widetilde{S} = S + \frac{\widetilde{\nu}}{\kappa^2 d^2} f_{v2}(\chi)$$

and f_{v2} is a second damping function:

$$f_{v2}(\chi) = 1 - \frac{\chi}{1 + \chi f_{v1}(\chi)}$$

and κ is the Von Karman constant ($\kappa = 0.41$). The calibration constant c_{b1} is set equal to 0.135. The destruction function is directly related to the wall distance d:

$$b_{dest} = c_{w1} f_w(r) \left(\frac{\widetilde{\nu}}{d}\right)^2$$

where r is a characteristic length:

$$r = \frac{\widetilde{\nu}}{\widetilde{S}\kappa^2 d^2}$$

and the function $f_w(r)$ is:

$$f_w(r) = g(r)\left[\frac{1 + c_{w3}^6}{g^6(r) + c_{w3}^6}\right]^{1/6}$$

where:

$$g(r) = r + c_{w2}\left(r^6 - r\right)$$

The calibration constants are:

$$c_{w1} = \frac{c_{b1}}{\kappa^2} + \frac{1 + c_{b2}}{\sigma} \ , \ c_{w2} = 0.2 \ , \ c_{w3} = 2$$

where c_{w1} has been chosen to balance the production and destruction term. Since a finite volume numerical scheme has been adopted, the turbulence equation Eq. (2.36) must be written in the "conservative law" form (i.e., integral form for a fixed volume):

$$\frac{d}{dt}\int_{\mathcal{V}} \widetilde{\nu}\, d\mathcal{V} + \oint_{\mathcal{S}} \underbrace{\widetilde{\nu}(\boldsymbol{v}\cdot\boldsymbol{n})}_{\text{convective term}} \, d\mathcal{S} - \oint_{\mathcal{S}} \underbrace{\frac{\nu+\widetilde{\nu}}{\sigma}\nabla\widetilde{\nu}\cdot\boldsymbol{n}}_{\text{diffusion term}} \, d\mathcal{S} - \int_{\mathcal{V}} \underbrace{\frac{c_{b2}}{\sigma}(\nabla\widetilde{\nu})^2}_{\text{diffusion term}} \, d\mathcal{V} =$$

$$\int_{\mathcal{V}} \underbrace{b_{prod}(S,\widetilde{\nu},d) - b_{dest}(\widetilde{\nu},d)}_{\text{production term}} \, d\mathcal{V}$$

where the convective term and the first diffusion term are expressed in conservative form, whereas the second diffusion term is expressed in non-conservative form and the production term is a source term expressed in non-conservative form.

Compressibility correction

Turbulent flows can be strongly affected by fluid compressibility effects. Although the phenomenology of the compressible turbulence is not completely clear, several important effects have been identified and investigated. Experimental studies about compressibility effects have been conducted over mixing layers between the same gas [31, 32, 33, 34], and different gases to include density variation effects [35]. Experiments show that as stream velocity increases, the mixing layer thickness reduces. Thickness reduction is generally attributed to compressibility effects related to turbulence features changing with high velocity regime. In order to quantify compressibility effects, convective Mach number M_c has been widely assumed as a reference parameter [31, 32, 36]:

$$M_c = \frac{u_1 - u_2}{a_1 + a_2} \tag{2.37}$$

where u_i and a_i are velocity and speed of sound for each of the streams ($i = 1, 2$) of the mixing layer. Mixing layer thickness can be measured by vorticity thickness δ_ω[31] and its growing rate can be defined as:

$$\left(\frac{d\delta_\omega}{dx}\right) = C_\omega(M_c)\frac{1-r}{1+r} \ , \ r = \frac{u_2}{u_1}$$

For low velocity ($M_c < 0.4$), $C_\omega = 0.168$, whereas it decreases up to half this value for $M_c > 1$. Compressibility effects on growth rate can be evaluated comparing compressible and incompressible growth rate $f_1(M_c) = (\delta_\omega)_c/(\delta_\omega)_i$. Similarly, compressibility

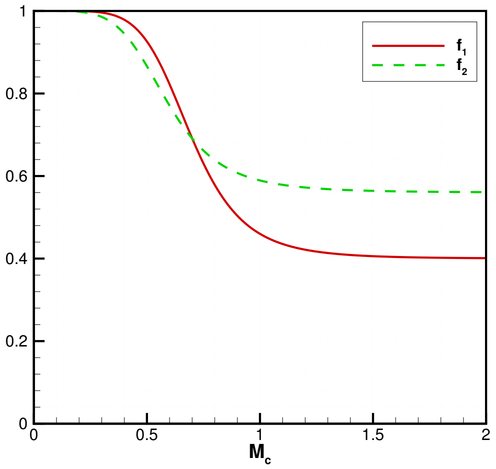

Figure 2.2: Compressibility effect functions f_1 and f_2 function of M_c

effects on turbulent shear stresses can be described as $f_2(M_c) = \tau_c/\tau_i$. Functions f_1 and f_2 are fitted to experimental data and depend on M_c only.

$$f_1 = 0.6\left[\frac{1}{1+9M_c^6}\right]+0.4 \ , \ \ f_2 = 0.44\left[\frac{1}{1+14M_c^5}\right]+0.56$$

Compressibility effects have been included in the present turbulence model as described in [37]. In particular, compressibility correction acts in reducing turbulent viscosity production term by a factor of $f_1 \times f_2$. Moreover, a generalization of this approach is obtained replacing the global convective Mach number M_c with the local convective Mach number $\tilde{M}_c$.

3

Numerical method

The governing partial differential equations for multi-species mixture of thermally perfect gases have been presented in Ch. 2. The choice of the discretization method of the selected mathematical model involves two components: the space discretization and the equation discretization. The space discretization consists in designing a mesh by which the continuum of space is replaced by a finite number of volumes where the averaged values of the variables will have to be determined. Once a mesh has been generated, the equations can be discretized leading to the transformation of the the integral form of the governing equations given in Eq. 2.11 to discrete algebraic operations involving the values of the unknowns related to the mesh volumes.

The finite volume method is a discretization method which is suited for the numerical simulation of various types of conservation laws and it has been extensively used in CFD. Its formulation enables its use on arbitrary geometries, discretized with structured or unstructured meshes.

3.1 Finite volume approach

The physical domain of interest is divided into hexahedral sub-domains of volume $\mathbb{V}$ and closed by N faces $\mathbb{S}_b$ with $b = 1, N$ [38].

Each flux contribution in the governing equations Eqs. 2.11 can then be written as the sum of fluxes through the face $\mathbb{S}_b$ with $\boldsymbol{n}_b$ normal to the face of interest:

$$\frac{d}{dt}\left(\overline{\boldsymbol{U}}\mathbb{V}\right) + \sum_{b=1}^{N} \overline{\boldsymbol{F}_b} \cdot \boldsymbol{n}_b \mathbb{S}_b - \sum_{b=1}^{N} \overline{\boldsymbol{G}_b} \cdot \boldsymbol{n}_b \mathbb{S}_b = 0 \tag{3.1}$$

where $\overline{\boldsymbol{U}}$ are averaged values of $\boldsymbol{U}$ with respect to the volume $\mathbb{V}$ and $\overline{\boldsymbol{F}}$ and $\overline{\boldsymbol{G}}$ are averaged values of $\boldsymbol{F}$ and $\boldsymbol{G}$ with respect to the surface $\mathbb{S}_b$

$$\overline{\boldsymbol{U}} = \frac{1}{\mathbb{V}} \int_{\mathbb{V}} \boldsymbol{U} d\mathbb{V}, \;\; \overline{\boldsymbol{F}_b} = \frac{1}{\mathbb{S}_b} \int_{\mathbb{S}_b} \boldsymbol{F}_b d\mathbb{S}, \;\; \overline{\boldsymbol{G}_b} = \frac{1}{\mathbb{S}_b} \int_{\mathbb{S}_b} \boldsymbol{G}_b d\mathbb{S} \tag{3.2}$$

Then, integrating in time from t to $t + \Delta t$ Eq. 3.1 becomes:

$$\left(\overline{\boldsymbol{U}}(t + \Delta t) - \overline{\boldsymbol{U}}(t)\right)\mathbb{V} + \sum_{b=1}^{N} \int_{t}^{t+\Delta t} \overline{\boldsymbol{F}_b} \cdot \boldsymbol{n}_b \mathbb{S}_b \, dt - \sum_{b=1}^{N} \int_{t}^{t+\Delta t} \overline{\boldsymbol{G}_b} \cdot \boldsymbol{n}_b \mathbb{S}_b \, dt = 0 \tag{3.3}$$

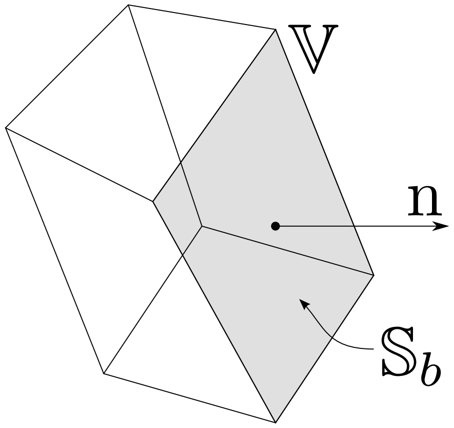

Figure 3.1: Hexahedral subdomain

In the time interval $(t, t+\Delta t)$ both inviscid and viscous fluxes can be averaged as follows:

$$\breve{\boldsymbol{F}}_b = \frac{1}{\Delta t}\int_t^{t+\Delta t} \overline{\boldsymbol{F}_b}\,dt\ ,\ \ \breve{\boldsymbol{G}}_b = \frac{1}{\Delta t}\int_t^{t+\Delta t} \overline{\boldsymbol{G}_b}\,dt \tag{3.4}$$

Recalling Eq. 3.3 and applying Eq. 3.4, the discrete time evolution of the averaged value in the volume $\mathbb{V}$ can be expressed as:

$$\overline{\boldsymbol{U}}(t+\Delta t) = \overline{\boldsymbol{U}}(t) - \frac{\Delta t}{\mathbb{V}}\left(\sum_{b=1}^{N} \breve{\boldsymbol{F}}_b \cdot \boldsymbol{n}_b \mathbb{S}_b - \sum_{b=1}^{N} \breve{\boldsymbol{G}}_b \cdot \boldsymbol{n}_b \mathbb{S}_b\right) \tag{3.5}$$

Hence the solution at time $t+\Delta t$, $\overline{\boldsymbol{U}}(t+\Delta t)$ is obtained by the solution at the previous time step $\overline{\boldsymbol{U}}(t)$ and the inviscid and viscous fluxes, $\breve{\boldsymbol{F}}_b$ and $\breve{\boldsymbol{G}}_b$.

Viscous fluxes are evaluated at the interface location by means of a second order central difference scheme involving the contiguous cells. In case of multi-component mixture, the numerical solution must satisfy Eq. 2.4. Solving for all the $\mathcal{N}$ species continuity equations (see Sec. 2.2), species mass fluxes must be corrected distributing the residual with respect to Eq. 2.4 according to the species mass fraction sharing the numerical error among all species [25]:

$$\breve{\boldsymbol{G}}_b^s\Big|_{corrected} = \breve{\boldsymbol{G}}_b^s - y_s \sum_{i=1}^{\mathcal{N}} \breve{\boldsymbol{G}}_b^i\ , \quad s = 1, \mathcal{N}$$

where $\breve{\boldsymbol{G}}_b^s$ is the average viscous mass flux of species s through interface b.

The inviscid flux at a generic interface is evaluated considering a one-dimensional Riemann problem between the two adjacent cells that overlooks the interface.

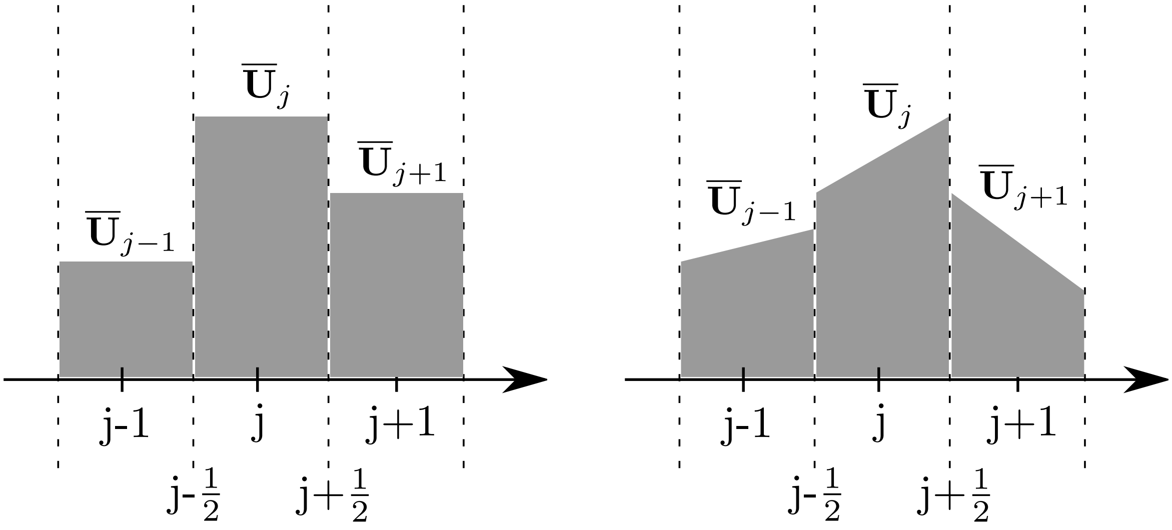

(a) First order accurate (b) Second order accurate

Figure 3.2: Reconstrution step

3.2 Inviscid fluxes

A one-dimensional Riemann problem is solved to provide the inviscid fluxes through the six interfaces of the hexahedral volume assuming the velocity component orthogonal to the interface surface as the scalar velocity for each Riemann problem. In particular, a three step strategy is applied:

- reconstruction of the variables value at the cell interfaces;
- local evolution of the solution at the cell interfaces;
- evolution of the cell average variables.

3.2.1 Reconstruction

The reconstruction step provides a distribution of the conservative variables in the cell. In the finite volume scheme proposed by Godunov [39] the cell variables are considered as piecewise constant as shown in Fig. 3.2(a).

Using this type of reconstruction the method is first-order accurate in space. If a linear piecewise reconstruction is used for the variables, a second-order accuracy in space is reached. The slope of the linear cell reconstruction is selected with respect to the average values of the cell $\overline{\boldsymbol{U}}_j$ and of the contiguous cell $\overline{\boldsymbol{U}}_{j-1}$ and $\overline{\boldsymbol{U}}_{j+1}$ as shown in Fig. 3.2(b).

Since the linear cell reconstruction can originate non-physical oscillations and thus unstable solutions, a slope limiter must be employed to ensure the stability of the numerical scheme (TVD condition). In the present code, a *minmod* slope limiter has been considered. If r is the ratio between the slope at the previous cell and the slope at the actual cell, the *minmod* limiter is:

$$\Psi = \max(0, \min(r, 1))$$

Such that if the slope sign of the local cell is the same as the previous cell, the minimum slope is considered for the local cell; otherwise a constant value is considered for the local cell.

3.2.2 Local evolution

In the local evolution step, the vector of inviscid fluxes at the generic interface $\breve{\boldsymbol{F}}_{j+\frac{1}{2}}$ is evaluated as the solution of a Riemann problem (see Sec. 3.3) between the right state $\overline{\boldsymbol{U}}^{R}_{j+\frac{1}{2}}$ and the left state $\overline{\boldsymbol{U}}^{L}_{j+\frac{1}{2}}$. The first is defined as the value of the solution reconstruction in the cell $j+1$ at the space abscissa $x_{j+\frac{1}{2}}$ and the second is defined as the value of the solution reconstruction in the cell j at the space abscissa $x_{j+\frac{1}{2}}$ The solution of the Riemann problem provides the interface value of the variable vector $\overline{\boldsymbol{U}}^{\mathcal{RP}}_{j+\frac{1}{2}}$.

3.2.3 Global evolution

In the final step , the difference between the average variables at time t and $t+\Delta t$ are evaluated as the inviscid fluxes time integral at the interface. The solution of the Riemann problem is constant between time t and time $t+\Delta t$. After that time the waves originated from the contiguous Riemann problems interact, and thus the interface solution is not constant any more (Fig. 3.3).

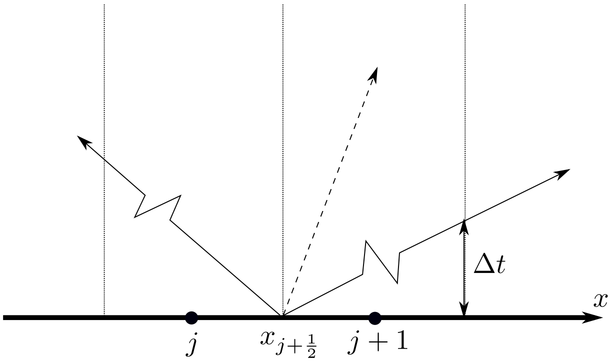

Figure 3.3: Waves originated by Riemann problem at the interface $x_{j+\frac{1}{2}}$.

If λ_{max} is the fastest wave velocity originated by the Riemann problem, the time step Δt must therefore satisfy the condition (called CFL condition from Courant, Friedrichs and Lewy):

$$\Delta t \leq \frac{\Delta x}{\lambda_{max}} \tag{3.6}$$

where Δx is the cell spacing. The CFL condition ensures that the solution at the new time step $t+\Delta t$ is consistent with the previous time step solution. If the interface fluxes are constant through time Δt (that is, Eq. 3.6 is satisfied), once the previous time step solution $\overline{\boldsymbol{U}}(t)$ is known, the new solution $\overline{\boldsymbol{U}}(t+\Delta t)$ is evaluated as:

$$\left[\overline{\boldsymbol{U}}(t+\Delta t)\right]_{inviscid} = \overline{\boldsymbol{U}}(t) - \frac{\Delta t}{\Delta x}\left(\breve{\boldsymbol{F}}_{j+\frac{1}{2}} - \breve{\boldsymbol{F}}_{j-\frac{1}{2}}\right) \tag{3.7}$$

If the global inviscid time step Δt is the minimum between the entire space domain at time t, time accuracy is preserved but the smallest cell slows down the time evolution of the biggest cells. This problem becomes critical in case of stretched grids where the biggest cells can be several orders of magnitude greater than the smallest ones. If the steady-state solution is the only goal of the computation, time accuracy can be sacrificed by considering the local time step which verifies the local CFL condition $(\Delta t)_{inv}$ for every finite volume. Using this method, convergence to steady-state solution is reached much faster.

In the three-dimensional case, the inviscid fluxes $\breve{\boldsymbol{F}}$ have to be evaluated for each face $\mathbb{S}_b$ of the sub-domain. Hence a Riemann problem is evaluated at each interface, reducing the interface problem to a one-dimensional problem taking into account only the orthogonal component of the velocity to the interface and preserving the tangential component.

3.3 Riemann problem

The interface inviscid fluxes are evaluated as a function of the variable values at the interface location as the solution of the Riemann problem:

$$\boldsymbol{U}^{\mathcal{RP}}_{j+\frac{1}{2}} = \mathcal{RP}\left(\boldsymbol{U}^{L}_{j+\frac{1}{2}}, \boldsymbol{U}^{R}_{j+\frac{1}{2}}\right)$$

The Riemann problem is the interface solution ($x = x_0$) of the one-dimensional problem:

$$\left\{\begin{array}{l} \boldsymbol{U}_t + \boldsymbol{F}(\boldsymbol{U})_x = 0 \\ \boldsymbol{U}(x,t=0) = \left\{\begin{array}{ll} \boldsymbol{U}^L & \text{if } \; x < x_0 \\ \boldsymbol{U}^R & \text{if } \; x > x_0 \end{array}\right. \end{array}\right. \tag{3.8}$$

where $\boldsymbol{U}_t + \boldsymbol{F}(\boldsymbol{U})_x = 0$ is the one-dimensional differential form of the Eulerian conservation law (Eq. (2.11)) and $\boldsymbol{U}(x,t=0)$ is the initial condition of the Riemann problem. The interface solution of the problem Eq. (3.8) is a function of the two piecewise left and right initial conditions $\boldsymbol{U}^L$ and $\boldsymbol{U}^R$ and thus it is represented by:

$$\boldsymbol{U}(x = x_0, t) = \boldsymbol{U}^{\mathcal{RP}} = \mathcal{RP}\left(\boldsymbol{U}^L, \boldsymbol{U}^R\right)$$

The function $\mathcal{RP}$ can be evaluated using an exact or an approximate solver. In the next subsections the one-dimensional Eulerian problem for a multi-component mixture of thermally perfect gases will be introduced and then an approximate Riemann solver will be presented.

3.3.1 1D Euler equation for a multi-component mixture of thermally perfect gases

The conservation laws described in Sec. 2.2 can be also written in the quasi-linear form:

$$\frac{\partial \boldsymbol{U}}{\partial t} + \underline{\underline{\boldsymbol{A}}}(\boldsymbol{U})\frac{\partial \boldsymbol{U}}{\partial x} = 0$$

where the Jacobian matrix $\underline{\underline{\boldsymbol{A}}}(\boldsymbol{U})$ referred to the variable vector of Eq. 2.12 is:

$$\underline{\underline{\boldsymbol{A}}}(\boldsymbol{U}) = \frac{\partial \boldsymbol{F}(\boldsymbol{U})}{\partial \boldsymbol{U}}$$

whose components are

$$\underline{\underline{\boldsymbol{A}}}(\boldsymbol{U}) = \left(\begin{array}{ccc|cc} v\,(1-y_1) & \cdots & -vy_1 & y_1 & 0 \\ -vy_2 & \cdots & -vy_2 & y_2 & 0 \\ \vdots & \vdots & \vdots & \vdots & \vdots \\ -vy_{\mathcal{N}} & \cdots & v\,(1-y_{\mathcal{N}}) & y_{\mathcal{N}} & 0 \\ \hline v^2 + \dfrac{\partial p}{\partial \rho_1} & \cdots & v^2 + \dfrac{\partial p}{\partial \rho_{\mathcal{N}}} & 2v - v\,(\gamma-1) & -(\gamma-1) \\ v\left(\dfrac{\partial p}{\partial \rho_1} - h_0\right) & \cdots & v\left(\dfrac{\partial p}{\partial \rho_{\mathcal{N}}} - h_0\right) & h_0 - v^2\,(\gamma-1) & \gamma v \end{array}\right)$$

The eigenvalues of the Jacobian matrix $\underline{\underline{\boldsymbol{A}}}(\boldsymbol{U})$ are:

$$\lambda_i = \begin{cases} v & , \quad i = 1, \mathcal{N} \\ v + a & , \quad i = \mathcal{N}+1 \\ v - a & , \quad i = \mathcal{N}+2 \end{cases} \tag{3.9}$$

where the first $\mathcal{N}$ eigenvalues have the same values and represent the waves which lead the species transport. The corresponding eigenvectors are:

$$\mathcal{E}_i = \begin{bmatrix} 0 \\ \vdots \\ y_i \\ \vdots \\ 0 \\ y_i v \\ \rho_i\left(v^2 - c_{p,i}\right) \end{bmatrix} \text{ with } i = 1, \mathcal{N}; \quad \mathcal{E}_{\mathcal{N}+1} = \begin{bmatrix} y_1 \\ \vdots \\ y_{\mathcal{N}} \\ v + a \\ h_0 + va \end{bmatrix} ; \quad \mathcal{E}_{\mathcal{N}+2} = \begin{bmatrix} y_1 \\ \vdots \\ y_{\mathcal{N}} \\ v - a \\ h_0 - va \end{bmatrix} \tag{3.10}$$

Using the eigenvectors, the compatibility equations along the characteristic directions identified by the eigenvalues can be derived [21].

3.3.2 Exact Riemann problem solver for multi-component gas

The exact solution of the Riemann problem relies on three waves which are associated to the $\mathcal{N}+2$ eigenvalues of the Jacobian matrix of the system: the first is associated to $\mathcal{N}$ coincident eigenvalues $\lambda_s = v$, with $s = 1, \mathcal{N}$, the second wave is associated to $\lambda_{\mathcal{N}+1} = v + a$ and the third wave to $\lambda_{\mathcal{N}+2} = v - a$ (Fig. 3.4).

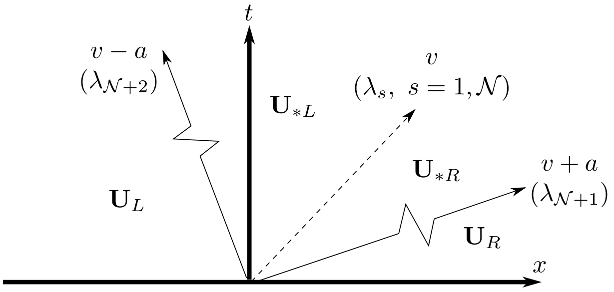

Figure 3.4: Schematic of the generic Riemann problem.

The three waves separate four constant states, which from the left to the right are U_L, U_{*L}, U_{*R}, and U_R. The unknown region between the left and the right waves, the star region, is divided by a contact discontinuity, which is the wave associated to the $\mathcal{N}$ eigenvalues $\lambda_s = u$. The left and the right waves can be either shock or rarefaction waves. Both pressure p_* and velocity u_* between the left and right waves are constant, while each species density has two constant values: $\rho_{s,*L}$ and $\rho_{s,*R}$. It is noteworthy that the specific heat ratio in the present formulation depends on temperature, dealing with a thermally perfect gas. Since the exact solution of the Riemann problem is a non trivial and time consuming computation, approximate Riemann solvers can be employed to provide an approximation of the interface solution $\boldsymbol{U}^{\mathcal{RP}}_{j+\frac{1}{2}}$ of the Riemann problem (Eq. (3.8)).

3.3.3 Approximate Riemann problem solver for multi-component gas

Several approximate Riemann solvers exist for ideal gas. Some of these solvers have been extended for a multi-component gas [21, 40]. In the following, the Roe Riemann solver is presented. It has been tested on a simple one-dimensional inviscid problem with variable composition and no appreciable differences between the exact and the approximate solver solution have been identified.

The Riemann solver of Roe

The Roe approximate Riemann solver [21] for a multi-component mixture of thermally perfect gas consists in evaluating the interface inviscid fluxes as function of the left and right state through the intermediate state of Roe. In particular, the interface fluxes

fluxes are evaluated as:

$$\breve{\boldsymbol{F}}_{j+\frac{1}{2}} = \frac{1}{2}\left(\breve{\boldsymbol{F}}^L + \breve{\boldsymbol{F}}^R\right) - \frac{1}{2}\sum_{i=1}^{m} \breve{\alpha}_i \left|\breve{\lambda}_i\right| \breve{\mathcal{E}}_i \tag{3.11}$$

where $\breve{\boldsymbol{F}}^L$ and $\breve{\boldsymbol{F}}^R$ are the left and the right state, respectively; $\breve{\alpha}_i$ are the average wave strengths function of the left and right state of the variable vector $\overline{\boldsymbol{U}}$ defined as follows:

$$\breve{\alpha}_i = \begin{cases} \dfrac{[\rho_i]}{\breve{\rho}_i} - \dfrac{[p]}{\breve{a}^2} & i = 1, \mathcal{N} \\[2ex] \dfrac{1}{2\breve{a}^2}\left([p] + \breve{\rho}\breve{a}[v]\right) & i = \mathcal{N}+1 \\[2ex] \dfrac{1}{2\breve{a}^2}\left([p] - \breve{\rho}\breve{a}[v]\right) & i = \mathcal{N}+2 \end{cases} \tag{3.12}$$

$\breve{\lambda}_i$ is the i-th average eigenvalue (Eq. 3.9) and $\breve{\mathcal{E}}_i$ is the i-th average eigenvector (Eq. 3.10). The average state $\breve{(\cdot)}$ is evaluated as:

$$\breve{(\cdot)} = \frac{(\cdot)_R\sqrt{\rho_R} + (\cdot)_L\sqrt{\rho_L}}{\sqrt{\rho_R} + \sqrt{\rho_L}}$$

The thermodynamic properties in the average state needed to evaluate the average wave strengths of Eq. 3.12 are defined as:

$$\breve{\rho} = \sqrt{\rho^L \rho^R}$$

$$\breve{a}^2 = (\breve{\gamma} - 1)\left[\breve{h}_0 - \frac{\breve{v}^2}{2} + \breve{c}_v^* \breve{T} - \textstyle\sum_{i=1}^{\mathcal{N}} \breve{y}_i \breve{e}_i\right]$$
$$\breve{\gamma} = 1 + \frac{\breve{\mathcal{R}}}{\breve{c}_v^*}$$
$$\breve{c}_v^* = \sum_{i=1}^{\mathcal{N}} \breve{y}_i \breve{c}_{v,i}^* = \sum_{i=1}^{\mathcal{N}} \breve{y}_i \frac{1}{[T]} \int_{T_L}^{T_R} c_{v,i}\, dT = \sum_{i=1}^{\mathcal{N}} \breve{y}_i \left(\overline{c_{p,i}} - \mathcal{R}_i\right)$$

3.4 Thermodynamic and transport model: numerical implementation

Recalling the definition of the properties given in Sec. 2.3, thermodynamic properties can be evaluated from the polynomial function for a given temperature and composition. However, the use of a database is necessary since the direct evaluation of the properties in a CFD code can drastically slow down the single step evaluation. A one-dimensional database with regular discretization ΔT for each species s is adopted where $\mathbb{T}_s(T)$ is the stored thermodynamic variable or transport property variable, described in Secs. 2.3.4 and 2.4.4, respectively. This kind of discretization enable the evaluation of the property $\mathbb{T}_s(\overline{T})$ at the desired temperature $T_i \geq \overline{T} \geq T_{i+1}$ for species s via a linear interpolation between the $\mathbb{T}_s\,(T_i)$ and $\mathbb{T}_s\,(T_{i+1})$

3.5 Boundary conditions

The inviscid and viscous fluxes at the interface are evaluated by considering the variables in the contiguous cells at the interface. However, contiguous cells are not available at the boundaries of the physical domain where boundary conditions must be enforced to evaluate the interface fluxes. In the present approach boundary conditions are obtained considering a "shell" of ghost cells surrounding the physical domain. In particular, the variables in the ghost cells are assigned in different ways depending on the nature of the boundary condition (wall, inflow/outflow, connection to another block, etc.). In the following sections, subscripts $()_O$ and $()_I$ will be adopted for outside and inside values, respectively; the interface state will be identified by the subscript $()_{int}$. The inside and outside values might be left or right state depending on the boundary under scrutiny.

3.5.1 Supersonic outflow

In the case of supersonic outflow ($v > a$) the three waves v, $v + a$ and $v - a$ are directed outwards the physical domain (see Fig. 3.5). The interface state ($\rho_{s,int}$, v_{int}, and p_{int}) is directly given by the solution inside the physical domain:

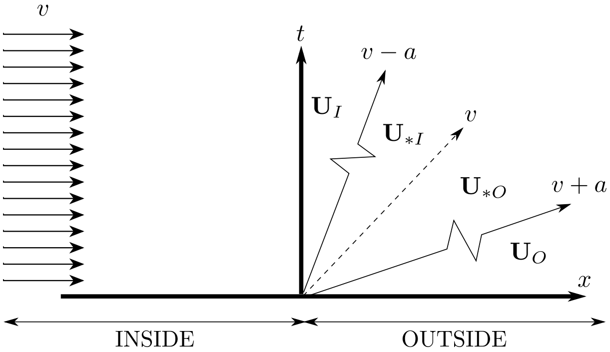

Figure 3.5: Schematic of the Riemann problem in case of supersonic outflow.

$$\begin{cases} \rho_{s,int} &= \rho_{s,I}\ , \quad s = 1, \mathcal{N} \\ v_{int} &= v_I \\ p_{int} &= p_I \end{cases}$$

Hence, in the case of supersonic outflow, no boundary conditions need to be provided.

3.5.2 Supersonic inflow

In the case of supersonic inflow ($u > a$) the three waves are directed inwards the physical domain (see Fig. 3.6).

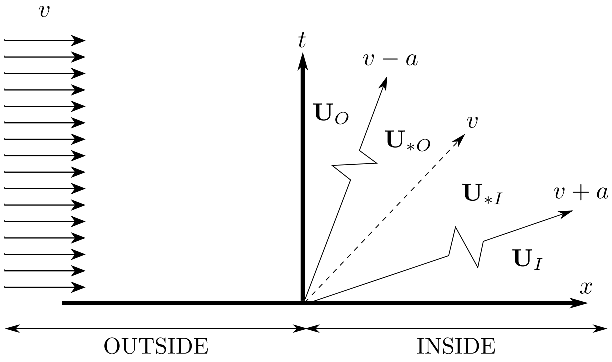

Figure 3.6: Schematic of the Riemann problem in case of supersonic inflow.

The solution at the interface is completely given by the outer conditions:

$$\begin{cases} \rho_{s,int} &= \rho_{s,O}\ , \quad s = 1, \mathcal{N} \\ v_{int} &= v_O \\ p_{int} &= p_O \end{cases}$$

where the subscript O stands for "outside". The whole outside state must be provided by the boundary condition.

3.5.3 Subsonic outflow

In the case of subsonic outflow ($v < a$), two waves v and $v + a$ are directed outwards the physical domain while the third wave $v - a$ travels inwards (see Fig. 3.7).

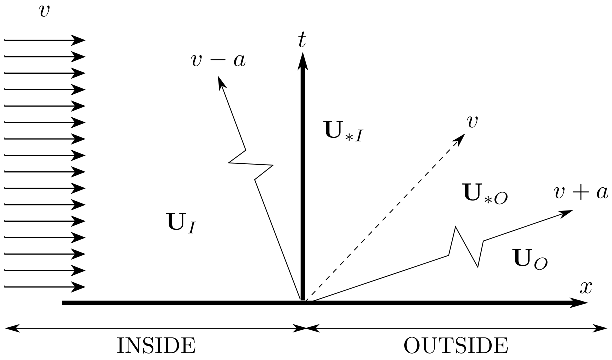

Figure 3.7: Schematic of the Riemann problem in case of subsonic outflow.

The inside state is known while the the outside state has to be prescribed. in the present study, static pressure outside the numerical domain p_O is assigned. To evaluate the interface solution some assumptions are made:

- the wave $v - a$ is an isentropic wave (that is, $\boldsymbol{U}_O \simeq \boldsymbol{U}_I$);
- $p_{*I} = p_O$

The isentropic relation to evaluate the temperature at the interface cannot be explicitly resolved due to the dependence of the specific heat from the temperature. Hence, the solution is evaluated by means of the Newton-Raphson method.

$$\begin{cases} \displaystyle\int_{T_I}^{T_{int}} c_p(T)\frac{dT}{T} & = \mathcal{R}_I \ln \dfrac{p_{int}}{p_I} \qquad\qquad \rightarrow T_{int} \\ v_{n,int} & = v_{n,I} - \displaystyle\int_{T_I}^{T_{int}} \frac{\sqrt{\gamma(T)\mathcal{R}T}}{\gamma(T)-1}\,\frac{dT}{T} \\ a_{int} & = \sqrt{\gamma(T_{int})\mathcal{R}_{int}T_{int}} \qquad\qquad \text{where } \mathcal{R}_{int} = \mathcal{R}_I \\ \rho_{int} & = \dfrac{p_{int}}{\mathcal{R}_{int}T_{int}} \\ \rho_{s,int} & = \dfrac{\rho_{s,I}}{\rho_I}\,\rho_{int}\,, \quad s = 1, \mathcal{N} \end{cases}$$

where $v_{n,int}$ is the interface orthogonal component of the velocity vector.

3.5.4 Subsonic inflow

In the case of subsonic inflow ($v < a$), two waves v and $v + a$ are directed inwards the physical domain while the third wave $v - a$ travels outwards (see Fig. 3.8). The inside state is known while the the outside state has to be prescribed. In the present study, stagnation temperature T_0, mixture composition in terms of mass fraction y_s and stagnation pressure p_0 or mass flow rate per unit area $\dot{m}/A_{int}$ are enforced as boundary conditions. In both cases, the three waves v, $v - a$ and $v + a$ are assumed to be isentropic waves to evaluate the interface state (that is, $\boldsymbol{U}_I \simeq \boldsymbol{U}_O$).

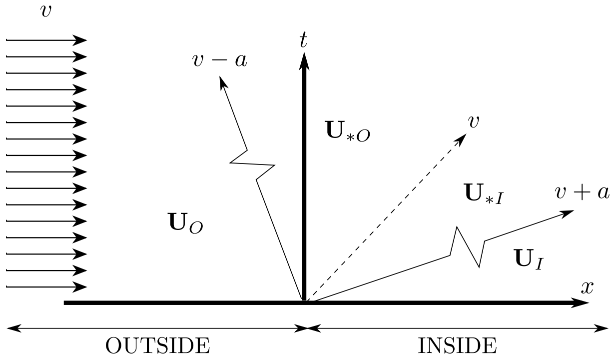

Figure 3.8: Schematic of the Riemann problem in case of subsonic inflow.

3.5.5 Inviscid wall or symmetry

In case of inviscid wall, the flow have to satisfies the following properties: the wall is impermeable then the flow cannot pass through it; the wall is non-catalytic then the mixture composition is not affected by the wall; pressure gradients normal to the wall are null. When treating with inviscid walls or symmetry, boundary condition must ensure the following interface properties:

- wall orthogonal velocity component is reflected (same module, opposite direction);

- wall non-orthogonal velocity components are not modified (same module, same direction);

- mixture composition is preserved;

- pressure is preserved.

The interface values are evaluated as the solution of an approximate Riemann problem between the inner state (known state) and the outer state (mirrored state) assigned to the facing ghost cells.

3.5.6 Multi-block connection

A basic multi-block approach is that of considering several structured grids whose volumes have a face in common [41]. With this constrain, boundary condition is trivial because the variables of the contiguous faced volume are extracted and assigned to the ghost cell of the volume of interest. After this procedure, an approximate Riemann problem between the known state and the ghost cell state is solved. This procedure ensures the conservative form of the scheme between blocks but it is too limiting to treat complex geometries.

In this study, complex geometries are analyzed reproducing experimental tests hence the basic multi-block approach has been extended to treat multi-block grids whose volumes have arbitrary position and dimension with respect to those of the contiguous block. In Fig. 3.9, the basic approach and the generalized approach are shown for two cartesian blocks.

This is realized by evaluating the properties of the ghost cell by interpolation from the inner values of the contiguous block. The developed algorithm is described in details in App. A. Once the ghost cell state has been evaluated from the neighboring volumes, an approximate Riemann problem is solved between the known state and the ghost cell state. In order to preserve the second order accuracy in space, two ghost cells are needed.

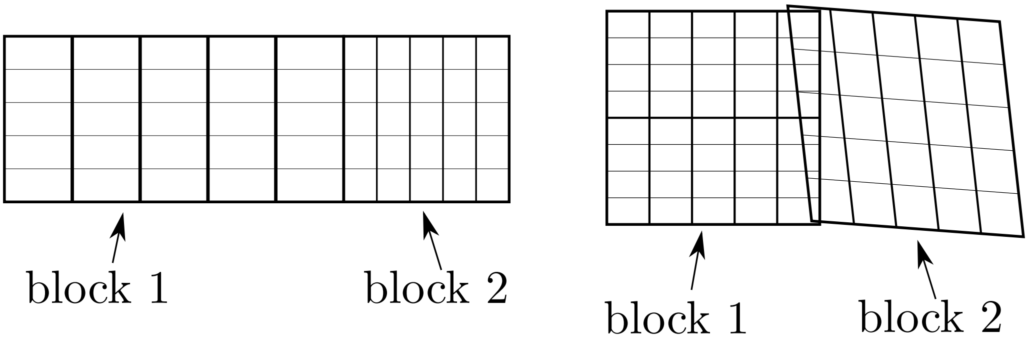

(a) Blocks with a face in common (b) Generic blocks connection

Figure 3.9: Multi-block grid approach

3.5.7 Viscous terms boundary conditions

Viscous fluxes at domain boundaries are evaluated as inside the domain resorting on one ghost cell whose variables are assigned depending on the boundary conditions enforced:

- Inflow/Outflow: null gradients are enforced for all variables in the ghost cells;

- Symmetry: ghost cells have the same values of boundary cells for all variables but velocity vector which is mirrored (face orthogonal component has the same module with opposite direction, face non-orthogonal components have same module and direction);

- Viscous wall: the wall does not induce molecular diffusion (non-catalytic wall), velocity is null, energy equation viscous fluxes are evaluated with enforced temperature or enforced heat flux;

- Multi-block connection: ghost cells are evaluated interpolating the inner values of the contiguous block.

4

Verification and Validation

Verification and validation are key processes to quantify the correctness of computational simulations in order to assess the reliability of numerical solvers as analysis tools for engineering systems[42]. In particular, verification evaluates the correct implementation in terms of coding and solution, whereas validation assesses if the implemented model is able to describe the physical phenomena of interest. For steady-state problems, solution verification is carried out checking iterative convergence and grid convergence. The first is a measure of the difference between the solution marching in the pseudo-time and the steady-state. The second is the evaluation of the capability of the mesh to properly capture the flow-field features.

In grid convergence analysis, for solution verification two conditions must be satisfied:

1. spatial order of accuracy should be equal to the theoretical spatial order of accuracy of the discretization method;
2. numerical solution obtained with three grid levels must be in the asymptotic grid convergence range.

Spatial order of accuracy can be evaluated assuming that the approximated solution f_k with a given grid k with a spacing factor h_k is affected by a single dominant error term of order p with respect to the exact solution:

$$f_k = f_{exact} + g_p h_k^p + \mathcal{O}(h_k^{p+1})$$

When three discrete solutions with a constant grid refinement factor ($r = h_2/h_1 = h_3/h_2$) are used, the previous equation written for the three grids can be solved for the order of accuracy:

$$p = \frac{\ln(\varepsilon_{32}/\varepsilon_{21})}{\ln r} \ , \ \ \varepsilon_{32} = f_3 - f_2 \ , \ \ \varepsilon_{21} = f_2 - f_1 \tag{4.1}$$

Once the spatial order of accuracy is verified and the three grid level solutions are in the asymptotic grid convergence range, an approximation of the continuum solution can be computed using two of the three discrete solutions with a constant grid refinement factor. Richardson extrapolated solution, f_{RE}, can be evaluated as follows[42]:

$$f_{exact} \approx f_{RE} = \frac{r^p f_1 - f_2}{r^p - 1} \tag{4.2}$$

Hence, the numerical error can be quantified with respect to the Richardson extrapolated solution.

Validation can be performed for submodels and for the overall computational model through comparison with experimental data. Model validation for a given set of conditions evaluates the adequacy of the proposed model to capture physical phenomena of interest. After validation, the implemented model can be employed to study similar conditions and configurations close to the validated ones.

The aim of this chapter is to verify and validate the multi-species features of the present numerical solver.

In the following sections, four test cases are presented for verification and validation:

1. convergent-divergent nozzle: wall heat flux evaluation.
2. air subsonic film cooling: film cooling efficiency evaluation;
3. helium/air supersonic/supersonic mixing layer: mixing layer spreading rate evaluation;

For the first test case, verification and validation is performed. The second test case is employed to validate the capability to capture the subsonic thermal boundary layer, whereas the third test case is reproduced to validate mass diffusion mixing layer in case of mixing with strong composition gradients.

4.1 Convergent-divergent nozzle

The hot air flow in a supersonic nozzle is reproduced focusing on wall heat transfer. The selected configuration has been designed as a benchmark test case for which experimental point measurements for pressure, temperature and heat flux along the nozzle wall are collected [43]. It has been widely reproduced to validate the capability to capture heat transfer features of a large number of numerical solvers with different turbulence models [44, 45, 46, 47]. In the present section, test case No. 313 is selected whose setup is summarized in Tab. 4.1. The goal of this numerical rebuild is to verify the present implementation of the thermally perfect gas model by means of thermodynamic and transport property look-up tables. Hence, the solver is validated comparing the numerical solution with experimental data to prove the capability to reproduce the thermal boundary layer enforcing wall temperature and evaluating wall heat transfer.

Stagnation temperature (K)	842.78
Stagnation pressure (bar)	11.91
Flowing fluid	air

Table 4.1: Supersonic nozzle: test case setup No. 313

The numerical simulation is carried out by means of 2D axis-symmetric computations with grid and boundary conditions shown in Fig. 4.1. Stagnation pressure, stagnation temperature, mixture composition and velocity direction are enforced at the inlet boundary. The outlet boundary is set as supersonic then no condition has to be prescribed. The upper boundary is set as a no-slip wall with enforced wall temperature, whose values are interpolated from the experimental measurements. Due to the small difference between wall temperature and stagnation temperature, wall heat flux evaluation depends on the wall temperature interpolation. Hence a sensitivity analysis of wall heat flux to the wall temperature interpolation is performed in the following. The lower boundary is the axis of symmetry. Three grid levels are employed to verify grid convergence, with the fine grid having 200 × 180 cells in the axial and radial directions, respectively. The medium grid is obtained by removing one node out of two, in each coordinate direction, from the fine grid. In the same way the coarse grid is obtained from the medium grid. The volumes adopted in the three grids are summarized in Tab. 4.2 together with minimum cell height.

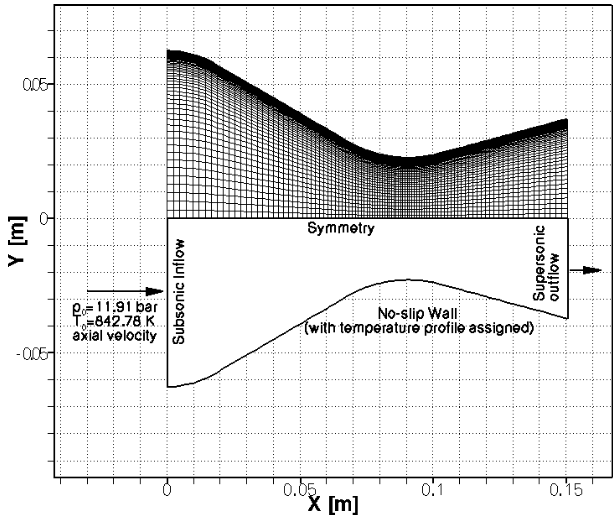

Figure 4.1: Supersonic nozzle: computational grid (medium grid level) and boundary conditions enforced (test No. 313 [43]).

Grid Levels	Number of volumes	Δy_{min}
Coarse grid	50 × 45	0.8 μm
Medium grid	100 × 90	0.4 μm
Fine grid	200 × 180	0.2 μm

Table 4.2: Supersonic nozzle: grid verification

The grid independence of the solution is assessed comparing axial velocity profiles at the throat (x=0.0823 m) and wall heat flux along the nozzle. In Fig. 4.2(a) and in Fig. 4.2(b), the numerical solutions obtained with the fine, the medium and the coarse grid are plotted together with the estimation of the medium grid size numerical error referred to the Richardson extrapolated numerical solution for the axial velocity component in the throat section and the wall heat flux along the nozzle, respectively.

Comparing the numerical solution obtained with coarse, medium and fine grids, grid independence is reached. As a reference, Richardson extrapolated numerical solution is evaluated by Eq. 4.2. Spatial accuracy p is evaluated with Eq. 4.1 and it is near the theoretical spatial order of accuracy far from regions where strong gradients occur (for example outside the boundary layer in Y=0.0207 m, the spatial order of accuracy is p=1.9799). Where strong gradients occur, the *minmod* flux limiter acts locally reducing the spatial order of accuracy to preserve numerical stability (for example in the boundary layer in Y=0.0235 m, the spatial order of accuracy is p=1.306).

As example of integrated variable convergence, axial velocity profile shows errors lower than 0.25 % with the medium grid size. As example of derived variable convergence, wall heat flux along the nozzle shows errors up to 7 % with the medium grid in the region near the inlet section where boundary layer develops whereas it reduces lower then 2% downstream.

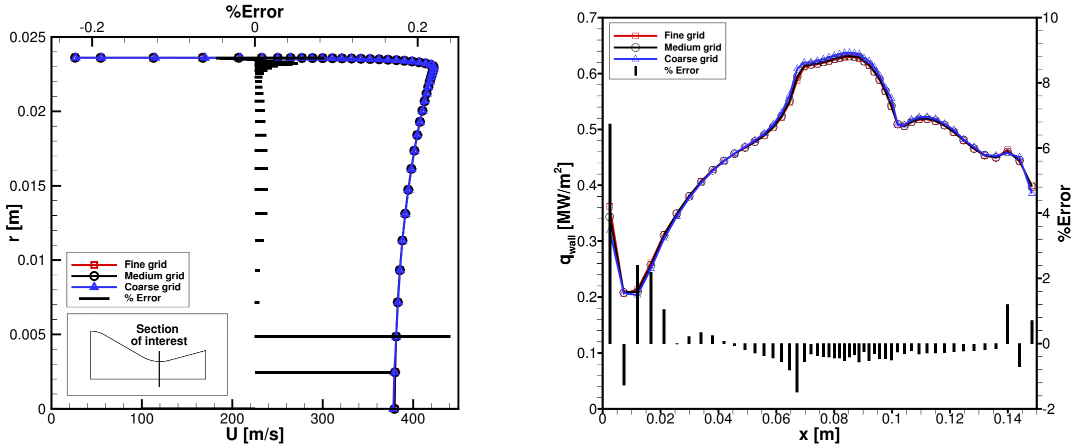

(a) Axial velocity profile at the throat section. (b) Wall heat flux along the chamber.

Figure 4.2: Supersonic nozzle numerical error estimation: numerical solutions obtained with fine, medium and coarse grids and medium grid size numerical error referred to Richardson extrapolated solution.

Once numerical solution has been verified and numerical error estimated, wall heat flux has been compared to experimental data available in the reference work. Wall temperature and wall heat flux measurement uncertainties are ±1% and ±8%, respectively, and are included in the experimental measurement plots by means of error bars. Note that wall temperature and flow stagnation temperature are quite similar hence wall heat flux evaluation may be affected by the wall temperature interpolation law.

Different reconstructions of wall temperature starting from experimental data are compared to quantify their influence on wall heat flux evaluation: piecewise linear reconstruction, least square polynomial interpolation and spline interpolation. The resulting wall heat fluxes are plotted in Fig. 4.3(a).

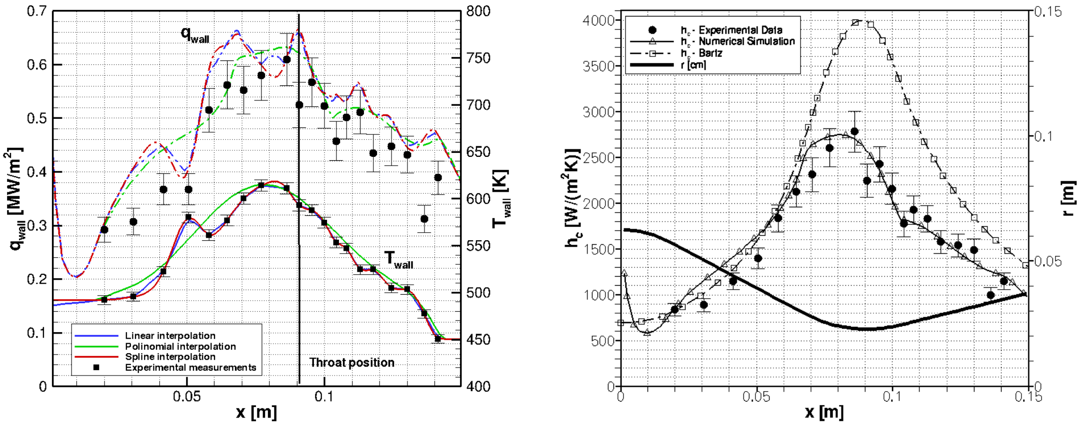

(a) Wall heat flux: experimental measurements and numerical evaluation with different wall temperature interpolation: piecewise linear, least square and spline.

(b) Convective heat transfer coefficient: experimental data, CFD numerical solution and Bartz's semi-empirical model (Eq. 4.4).

Figure 4.3: Supersonic nozzle: comparison between experimental data [43] and numerical solution

The high scatter of the experimental measurements clearly reflects on wall heat flux with local minimum and maximum values. Nevertheless, numerical wall heat flux follows experimental trend, despite the wall temperature reconstruction method, as shown in Fig. 4.3(a). In particular, in the convergent section wall heat flux is overestimated, whereas from the throat region downstream, wall heat flux numerical evaluation is close to experimental data within measurements uncertainties. The overestimation in the convergent section of the nozzle can be addressed to a thinner boundary layer caused by the inlet boundary condition: a uniform velocity profile is enforced and the boundary layer begins to grow downstream of the inlet section.

Moreover, numerical convective heat transfer coefficient is evaluated as the ratio between the wall heat flux and the difference between the adiabatic wall temperature and the experimental wall temperature:

$$h_c = \frac{q_{wall}}{T_{w,ad} - T_w} \tag{4.3}$$

and compared with experimental data (Fig. 4.3(b)) taking advantage of its weak dependence on wall temperature and, as a consequence, on its reconstruction method. As a reference, convective heat transfer coefficient evaluated by Bartz's correlation [48] is also included:

$$h_c = \left[\frac{0.026}{D_*^{0.2}} \left(\frac{\mu^{0.2} c_p}{Pr^{0.6}} \right) \left(\frac{p_c}{c^*} \right)^{0.8} \right] \cdot \left(\frac{A_*}{A} \right)^{0.9} \cdot \sigma \tag{4.4}$$

In Eq. (4.4), μ, c_p and Pr are the viscosity, the specific heat and the Prandtl number of the combustion gases, respectively, evaluated at the chamber conditions, p_c is the chamber pressure, c^* is the characteristic exhaust velocity, D_* is the nozzle diameter at the throat, A_*/A is the nozzle area ratio at the actual axial position and σ is a factor which contains the correction for property variations across the boundary layer.

As shown in Fig. 4.3(b), Bartz's correlation clearly overpredicts the convective heat transfer coefficient along the nozzle reaching a value 45 % higher than experimental measurement at the throat, whereas CFD numerical solution follows the experimental data within the error estimated in the reference work along the nozzle. The comparison between accurate numerical tools and semi-empirical models against experimental data shows that one-dimensional semi-empirical models cannot be employed for hot-gas side heat transfer predictive evaluation due to their low accuracy, especially in the throat region where the maximum heat flux occurs. The Bartz's correlation can be calibrated to fit the experimental data as described in [48], loosing its predictive ability for hot gas side heat transfer analysis, still remaining an efficient engineering correlation for preliminary heat flux estimation.

This test case has shown the capability of the solver to properly reproduce thermal boundary layers near the wall in accelerated flows, enforcing the experimental temperature ate the wall.

4.2 Air subsonic film cooling

A subsonic film cooling configuration over a flat plate is investigated focusing on film cooling efficiency evaluation. Cold air is injected parallel to an adiabatic wall to establish a layer that protects the wall from the main stream hot flow[49]. Film is injected through a two dimensional slot, whose height s is taken as a reference length. Upstream of the film injection, a splitter plate divides the film and the main stream. In the present configuration, the splitter plate thickness is not negligible compared to the slot height, hence it influences the flow downstream of the film injection, the mixing layer between film and main stream and, as a consequence, the film breaking point position, defined as the streamwise location where wall boundary layer and mixing layer merge. A schematic of the experimental layout is plotted in Fig. 4.4, where splitter plate thickness t, slot height s and film breaking point are identified.

Test case properties are summarized in Tab. 4.3. In this experimental test case, wall temperature measurements have been collected and analyzed in terms of adiabatic film cooling efficiency which is a measure of the ability of the film to protect the wall from the hot gas of the main stream. It is defined as[50]:

$$\eta = \frac{T_{main} - T_{w,ad}}{T_{main} - T_{film}} \tag{4.5}$$

where T_{main} and T_{film} are main stream and film temperature, respectively, and $T_{w,ad}$ is the measured temperature of the adiabatic wall with film cooling. It depends on the

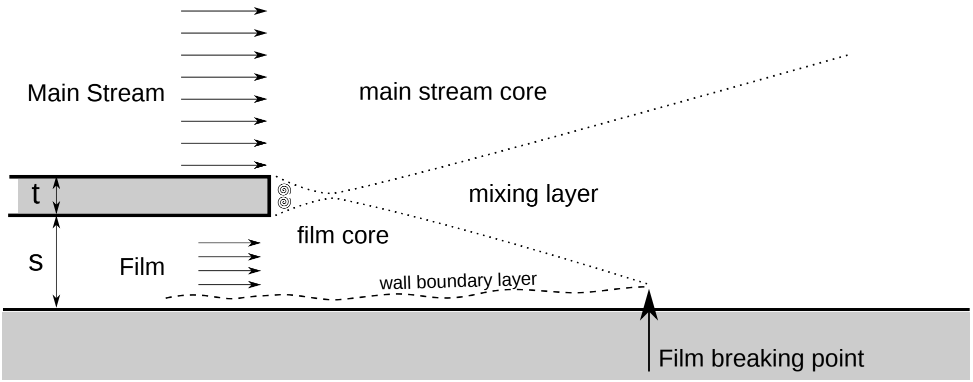

Figure 4.4: Film cooling experimental layout

	Main stream	Film stream
Velocity (m/s)	11.10	24.70
Temperature (K)	462.92	296.33
Pressure (bar)	1.0	1.0
Mach	0.0253	0.0704
Gas	Air	Air
Slot height s (mm)	4.00	
Splitter plate thickness t (mm)	0.76	

Table 4.3: Subsonic film cooling experimental setup data [49]

distance from the slot injection, the slot height and the blowing ratio:

$$\mathfrak{m} = \frac{\rho_{film} U_{film}}{\rho_{main} U_{main}}$$

and can be analytically evaluated by the Simon jet model [51] in case the blowing ratio is $\mathfrak{m} > 1.3$ [49] as in the present test case.

This experimental test case has been selected to investigate the capability of the solver to capture film cooling features as film cooling breaking and efficiency decay along the wall.

Two dimensional multi-block computational grid and boundary conditions are shown in Fig. 4.5, together with enlargements of the inlet section. Volumes are clustered towards the walls and in the region where mixing layer occurs. To ensure a fully developed flow at the end of the splitter plate, as prescribed in the experimental setup, the numerical domain extends to 50 s upstream of the splitter plate end. The overall domain where mixing occurs extends to 50 s downstream of the splitter plate end. In Fig. 4.5, the numerical domain is cut from 1 s upstream of the splitter plate end to 50 s downstream. The lower boundary is a no-slip adiabatic wall, the upper boundary is a slip wall and a constant static pressure distribution is specified at the outlet. At both inlets, stagnation temperature, stagnation pressure, mixture composition and flow direction are specified from the data available in [49] as summarized in Tab. 4.3.

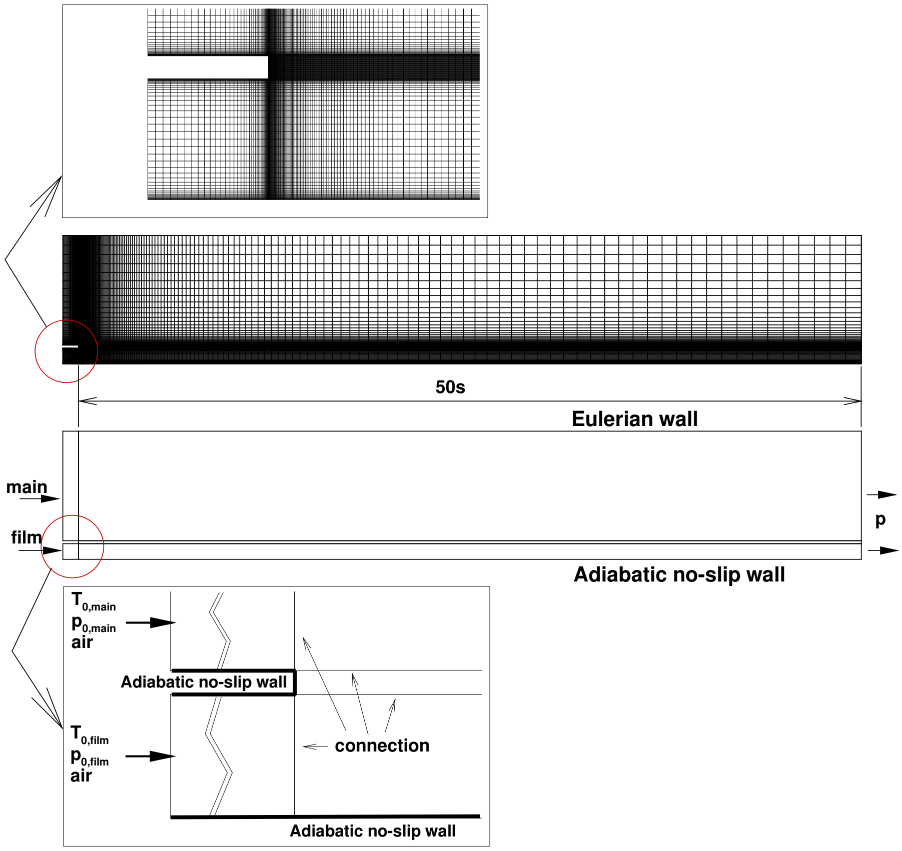

Figure 4.5: Multi-block computational domain (cut from 1 *s* upstream to 50 *s* downstream of the splitter plate end). Top: mesh grid with enlargement of the inlet section. Bottom: boundary conditions with enlargement of the inlet section.

In Fig. 4.6, temperature and velocity field are shown. The temperature mixing layer spreads stream-wise towards the wall with a consequent increasing of the wall temperature. The field of the streamwise velocity component shows the boundary layer growth along the wall, the shear layer spreading from the splitter plate end to the wall and the film breaking point where the shear layer reaches the wall boundary layer. Computed film cooling efficiency along the adiabatic wall is plotted in Fig. 4.7, where it is compared to experimental measurements which are affected by a small uncertainty ($\leq$0.76%) [49]. As a reference, numerical results obtained from the literature [52] obtained by a finite volume RANS equations solver with Menter's Shear Stress Transport (SST) turbulence model are also shown. Moreover, the film efficiency evaluated by means of the Simon jet model is included in Fig. 4.7. The efficiency of the film along the wall is governed by the growth of the shear layer separating the film from the main flow as well as the growth of the boundary layer along the wall. A discrepancy between experimental data and numerical solutions is evident in the origin of the decay, which identifies the film breaking point. This can be ascribed to three dimensional mixing effects which are not taken into account in both numerical simu-

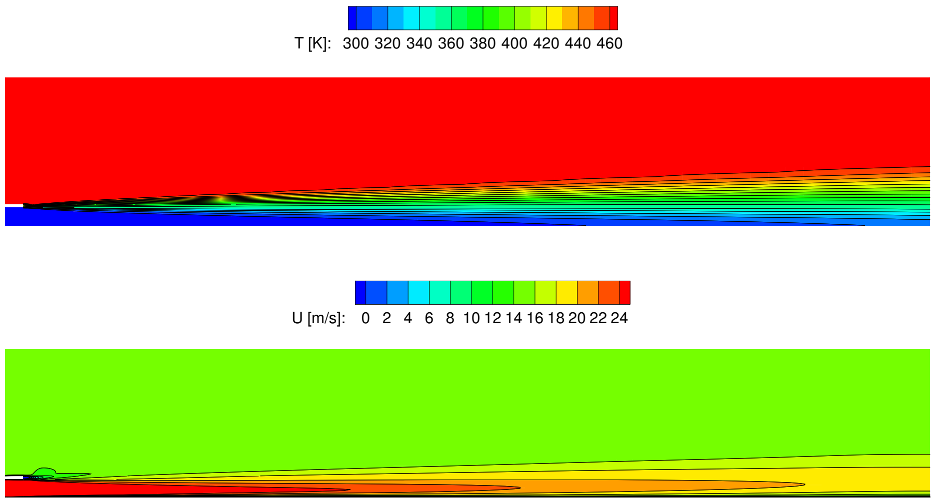

Figure 4.6: Subsonic film cooling: fields of temperature and stream-wise velocity component

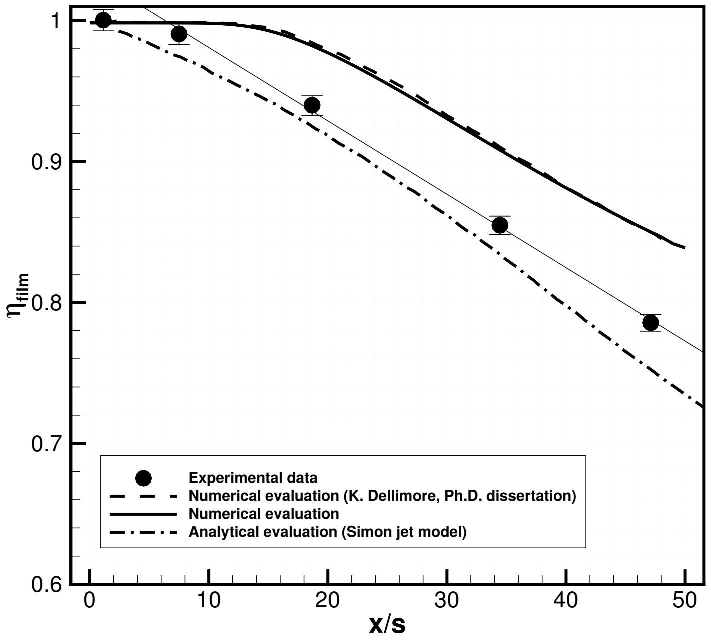

Figure 4.7: Film cooling efficiency η_{film}: comparison of experimental [49] versus present and literature[52] numerical data and Simon analytical jet model [51] (x/s =axial distance normalized with slot height).

lations performed solving the RANS equations. The analytical Simon jet model is in better agreement with the experimental data breaking point taking into account the turbulence intensity at the inlet of the film, which cannot be enforced as a boundary condition in the RANS numerical simulation. Nevertheless, numerical solutions are in good agreement with each other and are able to correctly predict the slope of the efficiency decay, even if they adopt different turbulence models. This result shows that the solver is able to capture the film cooling efficiency decay feature in the subsonic regime.

4.3 Helium/air supersonic/supersonic mixing layer

Multi-component mixture approach is validated by reproducing the mixing layer between two coaxial supersonic jets of helium and air, experimentally investigated in [53] and numerically reproduced in [30]. The experiment consists in a supersonic coaxial jet which discharges into stagnant air, with the center jet composed by a light gas (a mixture of 95 % helium and 5 % oxygen by volume) and the co-flow jet of air. Helium mass fraction in the field is measured to identify the mixing layer spreading rate. Note that oxygen seeding in the center jet is provided for the RELIEF (Raman excitation plus laser induced electronic fluorescence) O_2 flow-tagging technique to measure the instantaneous axial component of velocity. Due to the large difference in molecular weight between helium and the seeding oxygen, the mixture composition of the center jet is approximately 70 % helium by mass and 30 % oxygen by mass. Both co-flow and center jet nozzles have been designed to provide exit flow at 1 bar pressure and nominal exit Mach number of 1.8. Because of the higher speed of sound of the center jet gas, the exit velocity of the center jet is more than twice that of the co-flow jet. The mixing layer between the center jet and the co-flow is compressible with convective Mach number (Eq. 2.37) $M_c = 0.7$. Thus, compressibility effects cannot be neglected and turbulence model compressibility correction described in Sec. 2.5.1 is adopted to account for mixing layer thickness reduction. The test case experimental conditions are summarized in Tab. 4.4.

	Inner jet	Annular jet
Velocity (m/s)	1097.89	490.20
Temperature (K)	146.31	182.12
Pressure (bar)	1.0	1.0
Mach	1.8	1.8
Mixture composition	$He + O_2$	Air

Table 4.4: Supersonic mixing layer experimental operating condition [53].

Center jet and co-flow are separated by a thin nozzle lip, whose thickness is negligible with respect to the center jet nozzle diameter. Hence, in the numerical simulation a zero thickness lip has been assumed neglecting the recirculation zone downstream of the lip. The experimental test configuration is shown in Fig. 4.8(a) where mixing layer thickness and spreading rate are defined. A single block axis-symmetric numerical

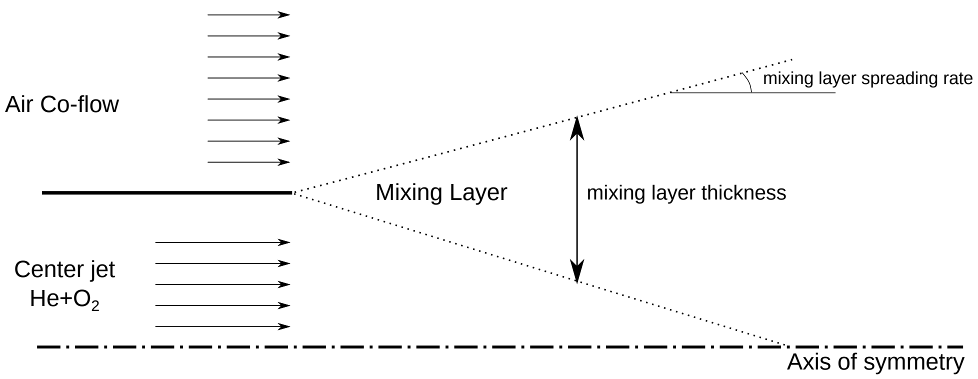

(a) Experimental test configuration.

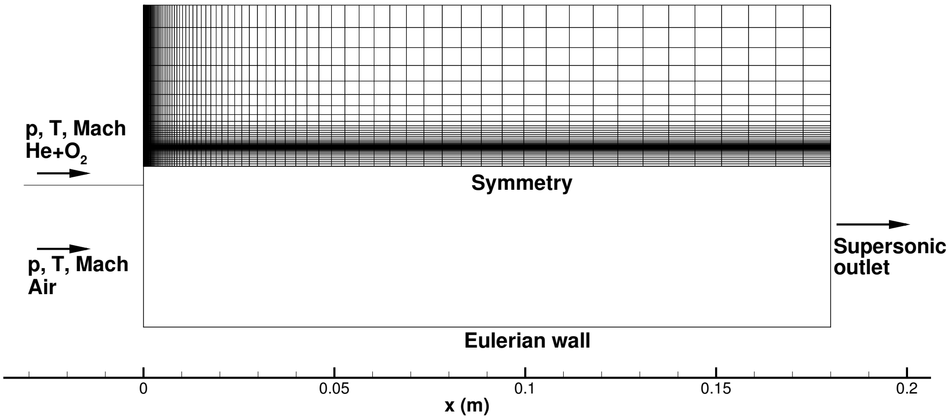

(b) Medium grid size numerical grid and boundary conditions enforced.

Figure 4.8: He/air supersonic mixing layer.

grid has been designed, where different injection boundary conditions are enforced in the inlet boundary as shown in Fig. 4.8(b). Cells are clustered in cross-wise and stream-wise direction in order to resolve properly the mixing layer region between center jet and co-flow. Two supersonic inlets are enforced in the left boundary (one for the lighter center jet and the other one for air), where Mach number, static pressure, static temperature, flow direction and mixture composition are specified, and supersonic outlet is prescribed at the right side of the domain. The lower boundary is an axis of symmetry and the upper boundary is a slip wall. Solution verification is performed with three grid levels starting from a fine grid removing one node out of two in each coordinate direction to obtain the medium grid level and in the same way the coarse grid is obtained from the medium grid. Volumes for each grid level are summarized in Tab. 4.5 together with the value of the minimum cell dimension at wall. The solution convergence history evaluated on the sum of the residuals of the species continuity equations for the three grid levels is shown in Fig. 4.9. Iterative convergence

	Volumes	Δy_{min}
Coarse grid	50×29	22 μm
Medium grid	100×58	11 μm
Fine grid	200×116	5.5 μm

Table 4.5: He/air supersonic mixing layer: solution verification grid levels and minimum cell dimension.

is assessed checking the $L2$ norms of the residuals for the governing equations over the entire domain because they approach to zero as convergence is reached. The grid

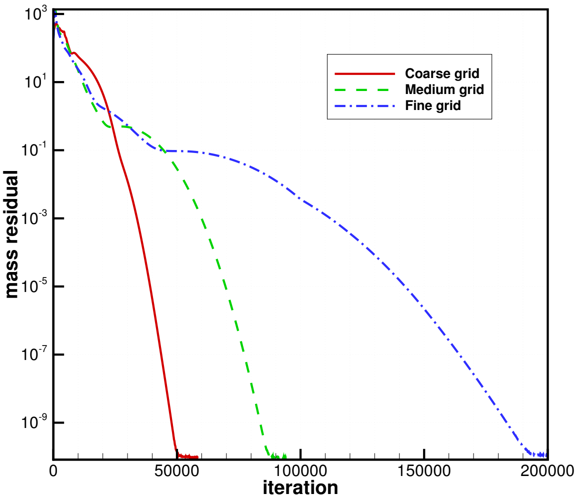

Figure 4.9: Sum of the species continuity equation residuals against iterations for the three mesh refinements: coarse, medium and fine grid.

independence of the solution is verified comparing axial velocity profiles (Fig. 4.10(a)) and oxygen partial density profiles (Fig. 4.10(b)) obtained with the three grid levels. Richardson extrapolated solution is taken as a reference for numerical error estimation. Note that profiles have been plotted in the mixing layer area to focus on the region where strong gradients occur. The three grid solutions are in the grid asymptotic convergence regime and the numerical error for the medium grid size is lower than 0.5% for the velocity profiles, whereas the oxygen mass fraction profile shows a numerical error up to 1%. The different numerical error obtained for axial velocity and oxygen partial density profiles can be ascribed to the different gradients involved in the shear layer and in the mixing layer. In particular, the velocity gradient between the two streams is lower than the mass fraction gradient inside the mixing layer. In the following, the numerical solution obtained with the medium grid is analyzed and compared to the experimental measurements of the helium molar fraction spreading rate provided in [53].

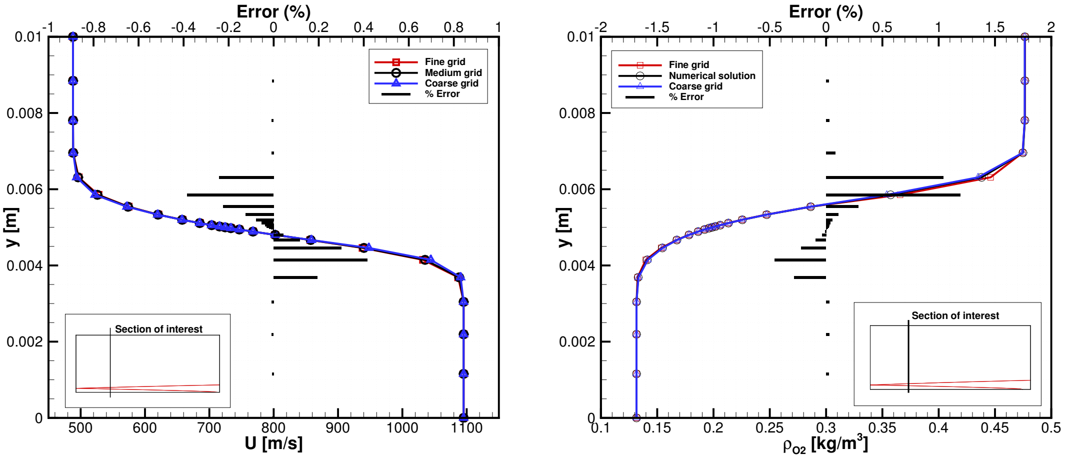

(a) Axial velocity profile at x=0.043 m (b) Oxygen partial density at x=0.043 m.

Figure 4.10: Numerical error estimation: numerical solution obtained with fine, medium and coarse grid size and medium grid size numerical error referred to the Richardson extrapolated solution.

Helium molar fraction field is shown in Fig. 4.11 where mixing layer spreading rate is identified within the iso-contour lines where helium molar fraction is 1% (top line) and 99% (bottom line) of the maximum helium molar fraction.

Fig. 4.12 shows the comparison between the experimental and the numerical helium molar fraction spreading rate. As described in [53], experimental measurements are affected by an error lower than 1.5% which is enclosed in the experimental dots plotted in Fig. 4.12. The numerical solution has been shifted upstream in order to compare the spreading rate slope with the experimental data. This is required because the splitter plate thickness has been neglected in the numerical simulation. Hence, the wake region just downstream of the splitter plate end is not resolved and the

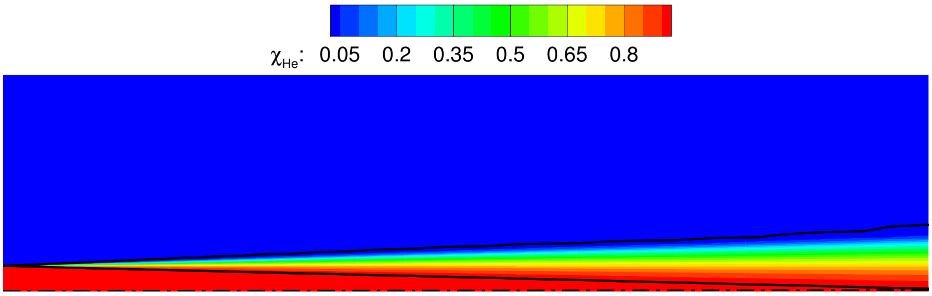

Figure 4.11: Helium molar fraction field.

numerical mixing layer begins to grow before the experimental one. Moreover, the present numerical solution is compared to other numerical solutions [30] obtained with a two-equation turbulence model once assuming different turbulent diffusion models: constant turbulent Schmidt number (Sc_T=0.6 and Sc_T=0.9) and variable turbulent Schmidt number coupled with the turbulence model. The last model is adopted for turbulent reacting flows at high Mach numbers where concentration fluctuations play a major role in predicting the ignition of the mixture for example in scramjet applications.

The present numerical solution is able to reproduce the experimental test case capturing the mixing layer spreading rate in the domain. Compared to the same turbulent diffusion model, the present turbulence model with a constant turbulent Schmidt number Sc_T=0.7 and with the compressibility correction described in Sec. 2.5.1 is able to evaluate the mixing layer spreading rate with an error lower than the other two numerical solutions shown in Fig. 4.12. Moreover, compared to the variable turbulent Schmidt number model solution, the present model applied to a non-reacting flow is able to evaluate the mixing layer spreading rate within a comparable error with a simpler turbulence model and turbulent diffusion model.

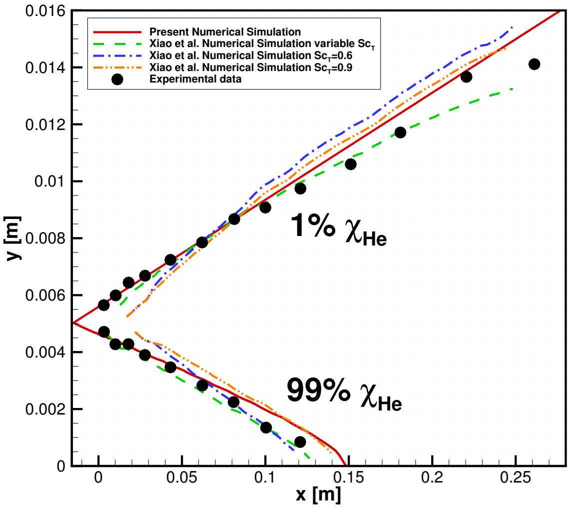

Figure 4.12: Helium molar fraction spreading rate: experimental measurements (circles) against present numerical solution ($Sc_T = 0.7$ solid line) and [30] numerical solution with constant ($Sc_T = 0.6$ dash-dot-dotted line and $Sc_T = 0.9$ dash-dotted line) and variable (dashed line) Sc_T.

The results obtained in the present validation test confirm the capability of the solver to properly evaluate the spatial evolution of mixing layers with strong mixture composition gradients and strong velocity gradients.

II

Results

5

Film cooled thrust chambers

In the frame of liquid rocket engine thrust chambers, active cooling techniques are required to withstand the high heat fluxes and high temperatures produced by the combustion of oxidant and fuel at high pressure. In particular, film cooling can be effectively employed as an active cooling technique inside the thrust chamber with low performance decrease in terms of specific impulse. It is adopted in critical regions such as walls near the injector plate and the nozzle throat where high temperature and heat flux occurs. Film cooling consists in injecting a cold film of gas or liquid tangential to the wall to protect it from hot gas.

Near the injector plate, film injection is provided by a single circumferential slot (*curtain cooling*) or through a number of finite width slots (*slot film cooling*) placed in correspondence of the outer injector ring arrangement. This active cooling technique has been widely adopted for high performance thrust chamber such as Space Shuttle main engine (SSME) and Vulcain 2 for the European launcher Ariane 5. For these engines thermal and structural loads are reduced by the combined use of film and regenerative cooling.

The influence of main governing parameters on film cooling efficiency has been included in several analytical models [50, 51, 54, 55]. Air-air and foreign gas-air film cooling have been extensively investigated by experimental studies [50, 49], and numerical simulations [56, 52, 57]. Recently, film cooling in oxygen/hydrogen thrust chambers has been investigated by experimental studies [58, 59, 60, 61] and numerical simulations [62, 63, 64, 65]. Film cooling has been also experimentally investigated for oxygen/kerosene [66, 67] and oxygen/methane [68] propellant combinations.

In Sec. 4.2, the film cooling experimental test case described in [49] has been reproduced and the evaluated adiabatic film cooling efficiency has been compared to experimental measurements, literature numerical solution and analytical solution. The goal of the test case was to validate the capability of the numerical solver to capture film cooling breaking point and efficiency decay.

In the present chapter, numerical simulation of film cooled thrust chambers is of interest, with particular attention to heat transfer evaluation. Then, typical thrust chamber operative conditions and configurations are investigated and a simplified approach is adopted to model hot gas inflow inside the chamber. Firstly, in Sec. 5.1, the capability of the simplified hot-gas injection model to provide the adequate thermal loads in thrust-chamber-like conditions is validated through the simulation of a literature sub-scale oxygen/hydrogen thrust chamber for which wall temperature and wall heat flux measurements are available. Moreover, the same configuration is numerically investigated when film cooling is activated to further validate the simplified approach for film slot injection configuration. Finally, the validated approach is applied to study an oxygen/methane film cooled sub-scale thrust chamber tested experimentally in the frame of the 7^{th} Framework Programme inside the "In-Space Propulsion 1" project.

5.1 Hot-gas simplified approach

Many different physical phenomena take place in liquid rocket engine thrust chambers: injection, atomization, vaporization, mixing and combustion. All these phenomena are confined to a limited region near the injector plate where chemical energy of the propellants is transformed in internal energy of the combustion products. Downstream, hot combustion products expand in a nozzle, where thermal energy is converted into kinetic energy. Due to the complex phenomena involved, different models should be applied to capture all physical phenomena inside the thrust chamber. A detailed analysis of these phenomena can be performed in a single-element configuration [69, 70, 71, 72, 73, 74], whereas it cannot be extended to full scale dimension because it needs grids with high resolution and increasing number of equation. As a consequence increasing the problem scale directly reflects on increasing the number of volumes of the mesh hence increasing the computational cost. As a compromise between global understanding of the problem inside the thrust chamber and low computational cost, a simplified approach is adopted here to evaluate the heat load coming from the combustion products inside the thrust chamber. Note that the simplified injection procedure cannot preserve all injectors parameter. Therefore, particular attention must be paid in the choice of the characteristic parameters to be matched in order to estimate the global steady state heat load. Limits and capabilities of the present low computational cost approach will be analyzed and discussed in the following.

In the present simplified approach, near injector plate phenomena are neglected. Equilibrium combustion products are injected in the chamber at the adiabatic flame temperature. Mixture composition and adiabatic flame temperature are evaluated by means of the "Chemical Equilibrium and Application" (CEA) program [23] prescribing stagnation chamber pressure and propellant mixture ratio. Hot-gas mass flow rate is prescribed, and the axial injection velocity is a result of the choice of the inlet section.

Once the mixture is injected in the thrust chamber, mixture composition is considered frozen along the whole chamber toward the nozzle. Under this assumptions, hot gas mass flow rate are injected in the thrust chamber with the two different approaches referred to as *full inlet* and *pseudo injector* described in the following:

- *full inlet* approach: injection section is the maximum section available due to geometrical constrains, i.e. thrust chamber cross section.

- *pseudo injector* approach: injection section is the annular section within the outer and inner injector ring. Injection velocity is a consequence of preserving mass flow rate and the flow acts like in a backward facing step configuration.

The different approaches are shown in Figs. 5.1. In particular, starting from a real multi-injector plate arrangement, the inlet section for the different simplified approaches is highlighted in red in Fig. 5.1(a). In Fig. 5.1(b), boundary layer features induced by the different injection approaches are shown.

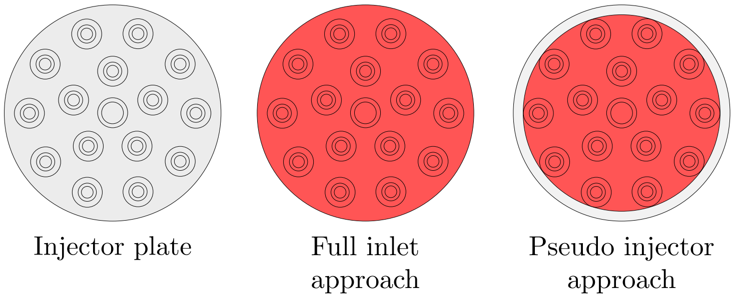

(a) Multi-injector plate: experimental layout (left), full inlet approach (center) and pseudo-injector approach (right).

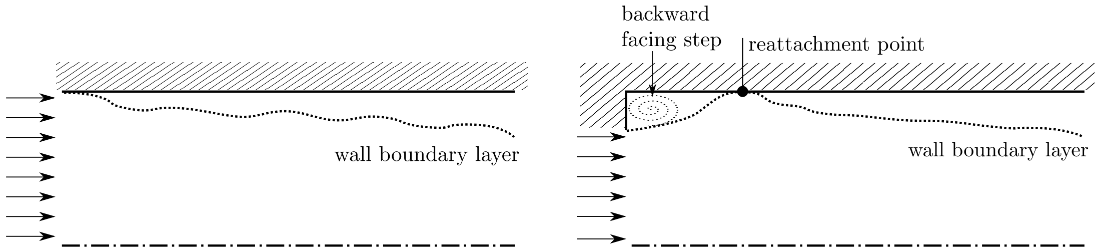

(b) Flow features: full inlet (left) and pseudo-injector (right) approach.

Figure 5.1: Simplified injection approach main features.

In the following, the simplified approach for hot-gas flow is validated reproducing an experimental test case. Prescribing experimental wall temperature, experimental wall heat flux measurements are compared to full inlet and pseudo injector approach wall heat flux evaluation.

5.1.1 Validation

The capability of the simplified modeling of the injector plate of providing an estimation of the heat load is proven comparing wall heat flux numerical solution and experimental measurements in a sub-scale thrust chamber. The experimental test case consists in a oxygen/hydrogen sub-scale calorimetric thrust chamber, where wall heat flux and wall temperature measurements are collected [65]. In particular, wall temperature are measured by means of thermocouples embedded in the thrust chamber wall material whose contact to the wall is ensured by a spring [75]. Wall heat flux is measured as the temperature increase of the coolant water collected in different sections. Hence, wall temperature measurements are local measurements whereas wall heat flux measurements are integral measurements associated to each section. The test was designed to reproduce thrust-chamber-like conditions such as high pressure and performance optimized mixture ratio. In Fig. 5.2 a sketch of the experimental test case is shown and in Tab. 5.1 the test case operative conditions are summarized.

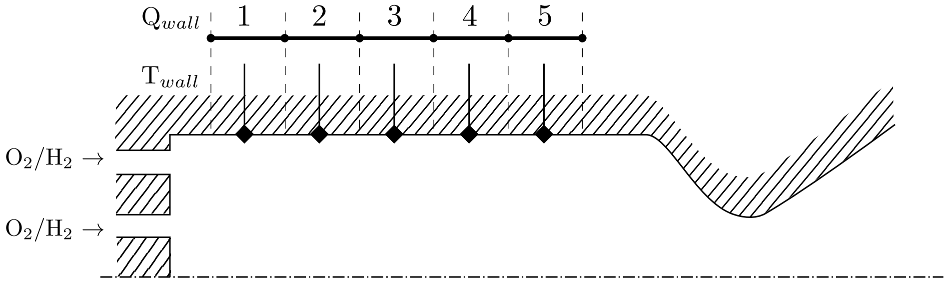

Figure 5.2: Oxygen/hydrogen sub-scale thrust chamber with wall temperature and wall heat flux measurement points [75].

Chamber pressure (bar)	116.2
Mixture ratio (O/F)	5.99
Adiabatic flame temperature (K)	3614.11
Number of injectors	15
Injectors mass flow rate (kg/s)	4.21
Chamber length (mm)	200 + nozzle
Chamber diameter (mm)	50
Nozzle throat (mm)	16.5

Table 5.1: Oxygen/hydrogen sub-scale thrust chamber experimental operative conditions.

Species	Mass fraction
H	0.0026
H_2	0.0369
H_2O	0.8849
O	0.0044
OH	0.0620
O_2	0.0092

Table 5.2: Oxygen/hydrogen equilibrium combustion products at test case conditions.

In the numerical simulation, the actual layout of the injector plate, composed by 15 coaxial injectors arranged into two rings, is replaced by the two simplified injection strategies (Fig. 5.1(a)). Numerical grid and boundary conditions enforced in the two approaches are shown in Figs. 5.3 and 5.4, respectively. The full inlet numerical simulation is carried out over a single-block grid whose cells are clustered toward the wall, On the other hand, the numerical simulation assuming the pseudo-injector approach requires a different grid strategy. In particular, a multi-block grid is considered which is composed by three adjacent blocks: the first block is clustered near the inlet section in both axial and radial direction to solve properly the recirculating flow which establishes in the backward facing step. The second and third block cells are clustered toward the wall. As a consequence the two numerical approaches have different inlet boundary conditions. Both approaches have the same enforced mixture composition and stagnation temperature evaluated under the assumption of chemical equilibrium (Tabs. 5.1 and 5.2). In the full inlet approach, stagnation pressure and velocity direction are prescribed to the whole chamber cross section, whereas in the pseudo injector

Grid Levels	No. of Volumes Block 1	 Block 2	 Block 3	Δy_{min}
Coarse grid	25x45	15x30	20x20	0.8 μm
Medium grid	50x90	30x60	40x40	0.4 μm
Fine grid	100x180	60x120	80x80	0.2 μm

Table 5.3: Pseudo-injector approach grid verification.

approach mass flow rate per unit area and velocity direction are prescribed in a part of the left boundary between the axis of symmetry and the outer injector ring; the remaining part of the left boundary is treated as an isothermal wall. For both the approaches, wall temperature values are enforced to the no-slip wall interpolating experimental measurements, the lower boundary is an axis of symmetry and the right boundary is a supersonic outflow, where no condition is prescribed.

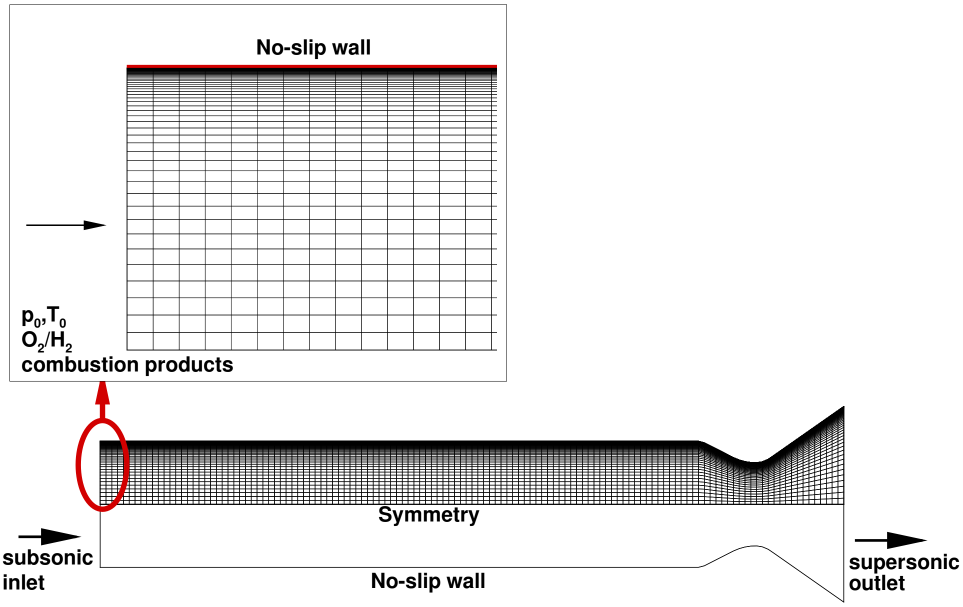

Figure 5.3: Full inlet approach: medium grid size numerical grid and boundary conditions.

Grid convergence analysis for the pseudo-injector approach is performed by simulations over three grid levels, whose volumes are reported in Tab. 5.3. Velocity profiles in the second block and wall heat flux along the chamber obtained with the three grid levels are shown in Figs. 5.5(a) and 5.5(b), respectively. Richardson extrapolated solution evaluated by means of Eq. (4.2) is adopted as a reference to evaluate medium grid

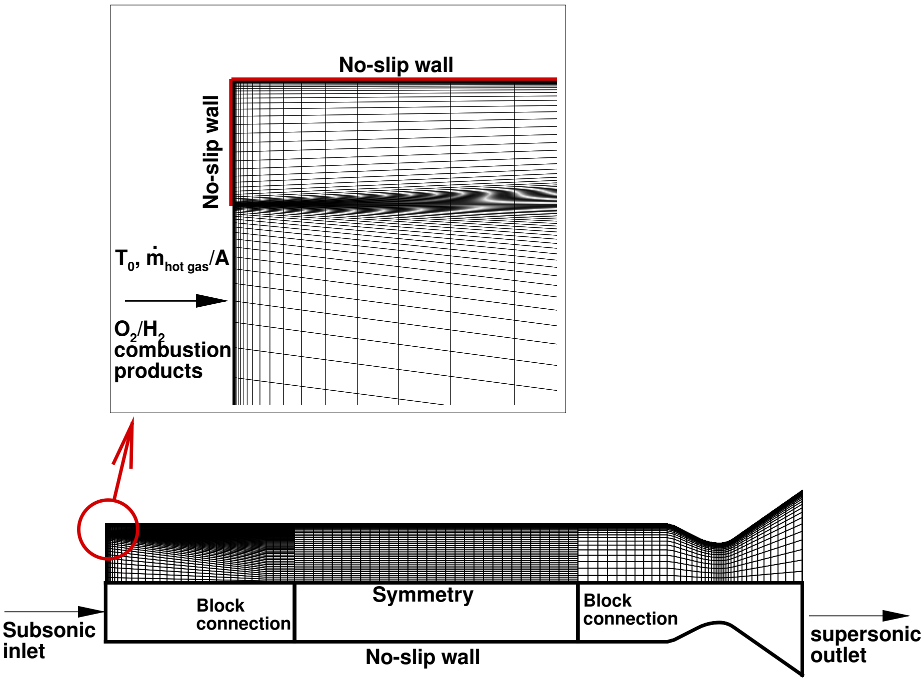

Figure 5.4: Pseudo-injector approach: medium grid size numerical grid and boundary conditions with enlargement of the inlet region.

size numerical error.

Velocity profiles obtained with the medium grid are affected by an estimated numerical error lower then 2%. The numerical solutions for the wall heat flux along the chamber evaluated with the three grids show that the grid independence is reached as the grid is refined.

Wall heat fluxes along the chamber evaluated by means of the two inlet approaches are then compared to experimental measurements, as shown in Fig. 5.6. In the full inlet approach, wall heat flux starts from a very high value, then rapidly decreases along the cylindrical section of the chamber and, finally, shows the peculiar peak associated to the strong expansion in the throat of the convergent-divergent nozzle. The wall heat flux monotonic decrease is associated to the establishment and growth of the wall boundary layer along the chamber. In the pseudo injector approach, wall heat flux trend along the chamber can be divided into three regions related to the flow field. In the first region, near the inlet section, wall heat flux shows a peak and a minimum value: the first is associated to the maximum velocity in the recirculating region; the second is associated to the reattachment point downstream of the recirculating region

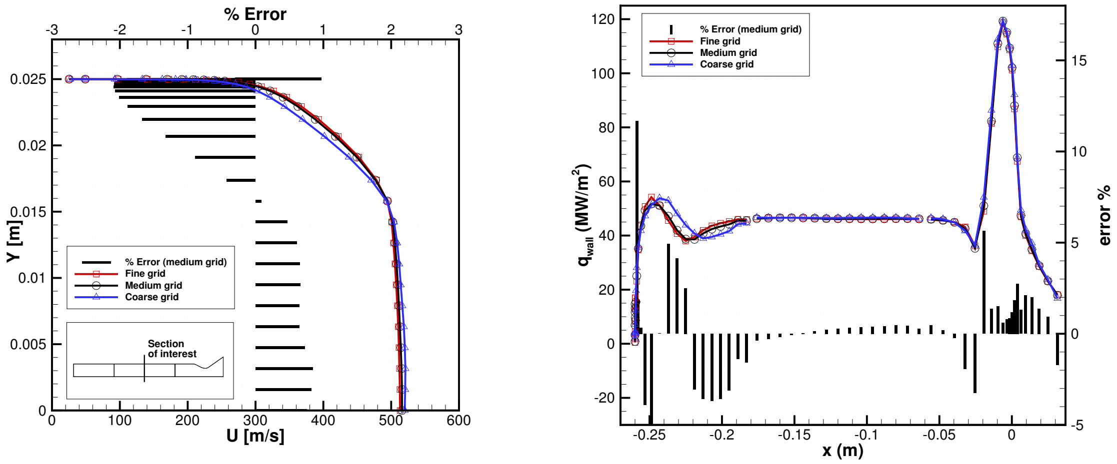

(a) Axial velocity profiles in the second block
(b) Wall heat flux along the chamber

Figure 5.5: Pseudo-injector approach numerical error evaluation: numerical solution obtained with fine, medium and coarse grid and medium grid size numerical error referred to Richardson extrapolated solution.

identified in Fig. 5.6 by means of velocity streamlines. Downstream of the reattachment point, in the second region, wall heat flux along the chamber reaches a constant value up to the nozzle, where the third region is identified by the peculiar heat flux peak due to the flow strong acceleration. Wall heat flux experimental measurements collected in the reference work are shown with their uncertainty (±8%). Both simplified approaches provide a good evaluation of the wall heat flux along the chamber. Full inlet approach largely overestimates wall heat flux in the inlet section due to its wall boundary layer behavior. Pseudo-injector approach provides a more accurate evaluation of the heat flux along the chamber, capturing the overall heat load in most of the sections where the measurements were collected within the experimental uncertainty. In this test case, no measurements where provided in the nozzle region.

5.2 Film cooled thrust chamber

Taking into account for the good results provided by the pseudo-injector approach, film cooling efficiency has been investigated in a simplified configuration. First, the same thrust chamber configuration analyzed in Sec. 5.1.1 is studied with film cooling reproducing the experimental test case described in [65, 61]. Then, the validated simplified approach is applied to an oxygen/methane film cooled thrust chamber investigated in the frame of the “In-Space Propulsion 1” project.

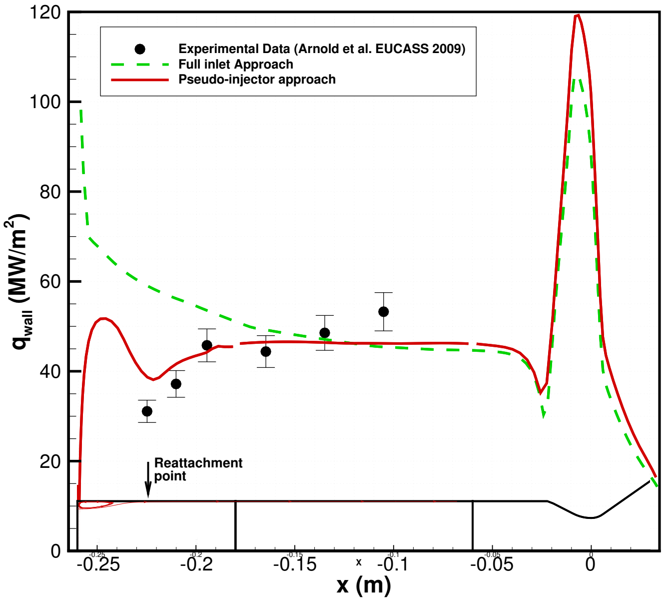

Figure 5.6: Wall heat flux along the chamber: comparison between full inlet approach (dashed line), pseudo-injector approach (solid line) numerical results and experimental measurements (circles) [65].

5.2.1 Validation

In [65, 61], the experimental setup studied in Sec. 5.1.1 was adopted to investigate film cooling characteristics, with particular attention to film mass flow rate and film slot position influence of film cooling efficiency. Due to the three-dimensional configuration of the film injection, both hot gas and film injection have been simplified to a two-dimensional axis-symmetric configuration as shown in Fig. 5.7.

The reduction from the three-dimensional slot film injection to the two-dimensional axis-symmetric configuration is performed matching the distance between the outer injector ring and the slot, the film injection slot height, velocity and temperature. Hence, film mass flow rate is not preserved. As a consequence, injecting higher film mass flow in the chamber would increase chamber pressure. To avoid the mismatch of chamber pressure that would strongly influence the heat transfer process a larger throat diameter is considered such to match experimental chamber pressure.

The numerical simulation is performed over a multi-block grid whose features are shown in Fig. 5.8 together with boundary conditions enforced. The numerical grid is divided into three blocks as in the test case without film cooling. The first block is designed to solve the mixing layer between hot gas and coolant and the wall boundary layer. The second and third blocks are clustered toward the wall to solve properly the wall boundary layer.

The left boundary is divided into three regions: hot gas injection, no-slip wall and

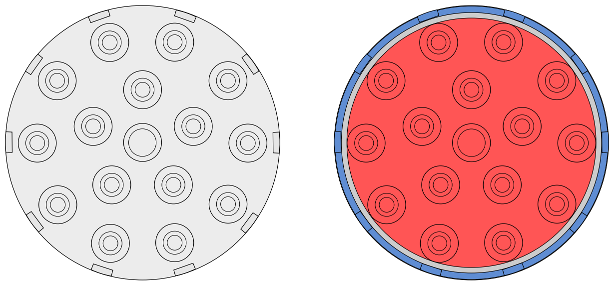

Injector plate

Pseudo injector approach

Figure 5.7: Multi-injector plate simplification with slot film cooling: experimental layout with film slot injection (left), and pseudo-injector approach with axis-symmetric film injection (right).

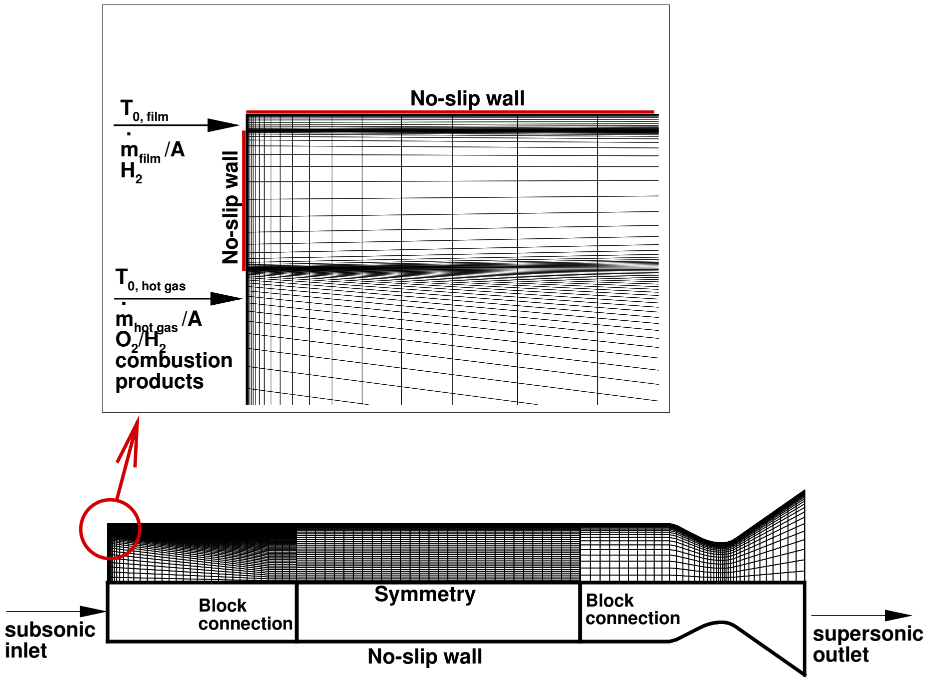

Figure 5.8: Film cooled thrust chamber: medium grid size numerical grid and boundary conditions with an enlargement of the inlet region.

film injection. Both hot gas and film injection boundaries are subsonic inlets where

Operative conditions	Chamber pressure (bar)	119.4
	Mixture ratio (O/F)	6.03
	Adiabatic flame temperature (K)	3619.46
Injector plate	Number of injectors	15
	Injectors mass flow rate (kg/s)	4.22
Film slot	Slot width (mm)	3.5
	Slot height (mm)	0.46
	Number of slots	10
	Inlet temperature (K)	299.39
Chamber	Chamber length (mm)	200 + nozzle
	Chamber diameter (mm)	50
	Nozzle throat (mm)	16.82

Table 5.4: Oxygen/hydrogen sub-scale thrust chamber with film cooling experimental operative conditions.

stagnation temperature, mass flow rate per unit area, mixture composition and velocity direction are prescribed. In the hot gas inlet section, stagnation temperature is evaluated as the adiabatic flame temperature obtained in the equilibrium combustion of oxygen and hydrogen at experimental chamber pressure and mixture ratio shown in Tab. 5.4. Mass flow rate per unit area is enforced at the inlet section preserving injectors overall mass flow rate and the same injection area of Sec. 5.1.1 is here adopted and highlighted in red in Fig. 5.7. Mixture composition is evaluated under the assumption of equilibrium combustion and is summarized in Tab. 5.2. In the film inlet section, stagnation temperature is the coolant experimental stagnation temperature. Mass flow rate per unit area is enforced preserving experimental density and velocity. The film inlet section is obtained matching film slot height and is highlighted in blue in Fig. 5.7. The coolant composition is set to be pure hydrogen and its inlet temperature is reported in Tab. 5.4. Experimental wall temperature is enforced at the no-slip walls. Supersonic outlet is set at the right boundary and the lower boundary is an axis of symmetry. Temperature field with and without film cooling are plotted in Fig. 5.9, together with velocity streamlines to highlight the backward facing step configuration for the thrust chamber without film cooling and the base recirculation region which establishes near the wall separating the hot gas and the coolant injection in the film cooled thrust chamber.

In the film cooled thrust chamber, film cooling action is persistent along the whole chamber up to the nozzle. Filled and empty circles represent wall heat flux experimental measurements by gradient method with and without film cooling, respectively [65]. Error bars (±8%) are included with the estimated error evaluated in the reference work. Wall heat flux numerical evaluation is plotted in solid red line for the case with film cooling. Wall heat flux without film cooling has been discussed in details in Sec. 5.1.1 and here is plotted in solid black line as a reference. Wall heat flux with film cooling is largely underestimated due to the larger amount of film injected in the

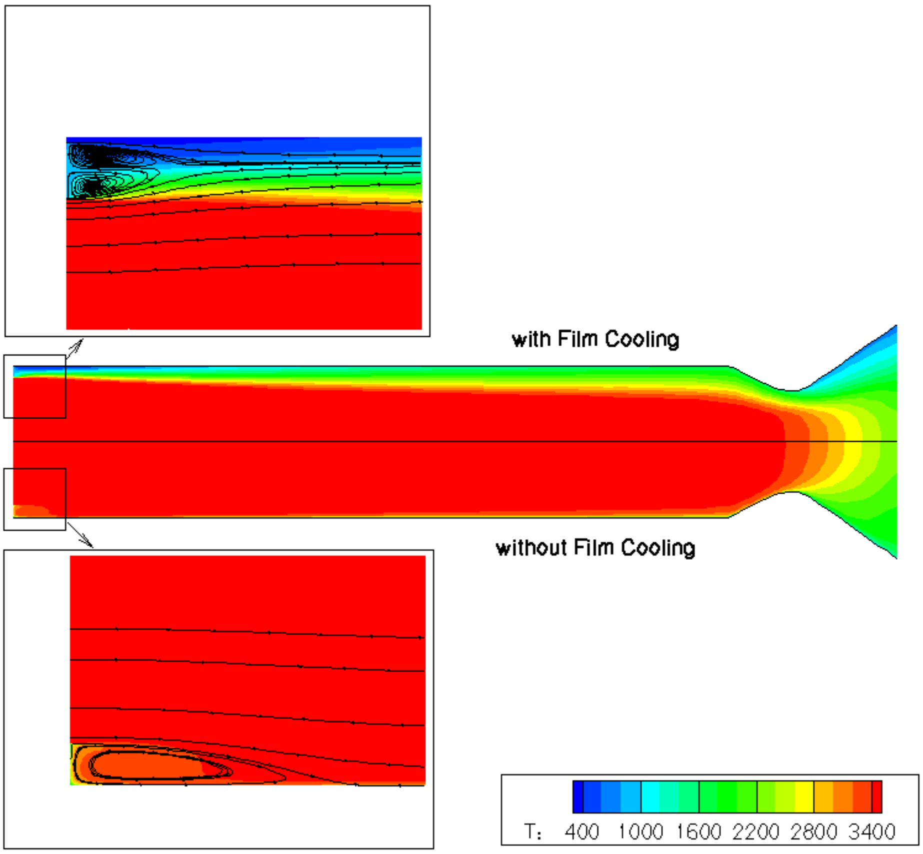

Figure 5.9: Temperature field in oxygen/hydrogen sub-scale thrust chamber with (top) and without (bottom) film cooling. Enlargement of the inlet region with velocity streamlines.

numerical simulation with respect to the experimental test. Nevertheless, numerical solution reproduces the experimental trend as can be seen comparing the red dashed line which represents the experimental trend of the last four measurement points and the red dot-dashed line which represents the numerical trend in the same spatial region. The higher film mass flow injected in the numerical simulation is due to the two-dimensional simplification of the actual geometry and to the choice of preserving film slot height and film inlet velocity rather than film mass flow percentage. To take into account the three dimensional configuration of the film slots, wall heat flux along the chamber with film cooling is evaluated by a weighted average ($q_{w,av}$) (blue solid line) between the numerical results obtained in the 2D axis-symmetric configuration with film $\left(q_{w,wfilm}\right)$ (red solid line) and without film $\left(q_{w,wofilm}\right)$ (black solid line). Weights are ϵ and $(1-\epsilon)$ where ϵ is the surface ratio between total slot width and the overall chamber perimeter:

$$q_{w,av} = \epsilon\, q_{w,w\ film} + (1-\epsilon)\, q_{w,wo\ film} \qquad \text{with: } \epsilon = \frac{N_{slot} b}{2\pi r_c} \tag{5.1}$$

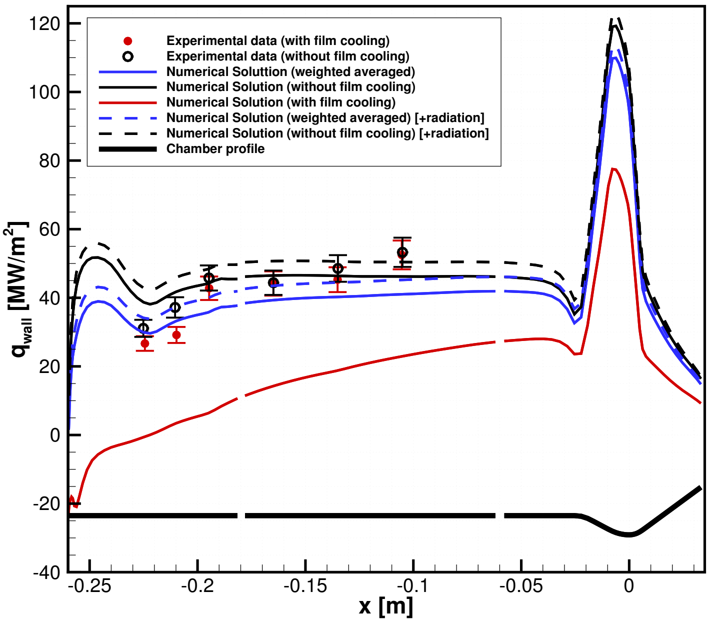

Figure 5.10: Oxygen/hydrogen film cooled thrust chamber wall heat flux: experimental measurements [65] (filled circles with film cooling; empty circles without film cooling) vs numerical solution with (red) and without (black) film cooling, and weighted averaged numerical solution with film cooling (blue) (Eq. 5.1). Dashed lines are the sum of convective and maximum radiative heat flux for the case with and without film cooling.

where N_{slot} is the number of film slots, b is the slot width and r_c is the chamber radius. The average wall heat flux evaluation proposed in Eq. 5.1 relies on two geometrical properties of the slot configuration under scrutiny: the slots high width to height ratio and the large distance of the slots between each other. The first one ensures that the film injection is mostly two dimensional along the wall. The second one allows to not take into account the interaction between near slots.

Comparing the weighted wall heat flux estimation, downstream of the two peaks related to the wall heat flux without film cooling, the plateau region follows experimental values within the measurements uncertainties. Moreover, a rough estimation of the radiative heat flux coming from the flame has been added to the convective wall heat flux and the sum of convective and radiative heat flux are shown in Fig. 5.10 as dashed lines with (blue line) and without (black line) film cooling. The maximum radiative heat flux from the hot gas to the wall has been evaluated with Eq. 5.2 valid for transparent gas and non-emitting walls:

$$q_{w,rad} = \varepsilon_g \sigma T^4_{Hot\,Gas} \tag{5.2}$$

where ε_g is the effective emissivity of hot gas, σ is the Stefan-Boltzmann constant and $T_{Hot\,Gas}$ is the maximum temperature in each section. Hot gas is supposed to be transparent in order to evaluate the maximum radiative heat flux coming to the wall assuming for each section the maximum gas temperature. Walls are supposed to be non-emitting because in thrust chambers wall temperature is always much lower than hot gas temperature to preserve the solid material from melting. In high pressure oxygen/hydrogen rocket thrust chambers, combustion products mixture is mainly composed by water vapor and the effective emissivity of this mixture has been evaluated in [76] and is assumed here to be equal to 0.45.

To validate the two dimensional numerical result reduction to take into account for the three dimensional slot injection, a three dimensional numerical simulation is performed for the same test case. Recalling the actual injector plate configuration, the film slots are placed in correspondence of the outer injectors ring position to enhance the coolant action on the wall in the azimuthal position where the flame action is supposed to be stronger. The numerical domain is identified taking advantage of the periodic arrangement of the slots around the chamber: a slice of the chamber is solved between half a slot and half empty space between two slots. Even in the three dimensional simulation, the injectors are simplified by means of the pseudo-injector approach described in Sec. 5.1. The numerical grid and boundary conditions enforced are shown in Fig. 5.11 with an enlargement of the inlet section. Following the pseudo-injector approach, equilibrium combustion products, whose composition is listed in Tab. 5.4, are injected in the inner section of the chamber slice enforcing mass flow rate per unit area and the stagnation temperature as the adiabatic flame temperature. Cold hydrogen is injected through the slot matching the film mass flow rate per unit area and the injection temperature. The distance between the outer injector ring and the distance between two slots is preserved and here the wall boundary condition is prescribed. In the whole thrust chamber, the lower boundary of the slice is an axis of symmetry and the right boundary is a supersonic outlet where no condition has to be prescribed. The upper boundary is a no slip wall where experimental wall temperature is enforced as in the two dimensional simulation, with a constant value in the spanwise direction. The numerical grid is a single block grid composed by 810000 volumes, clustered toward the walls to solve the boundary layers and near the injection section of both the combustion products and the film coolant where mixing layers establish. The present simplified approach takes into account only the film injection taking advantage of the high aspect ratio (width to height) of the slot geometry and the large distance between the outer injectors ring and the slot.

Due to the asymmetrical injection of the film coolant, the flowfield in the chamber near the injection section is characterized by a complex three dimensional recirculating region. This is a combination of two recirculating modes: the first is on the radial plane in the y direction where the recirculation zone is driven by the asymmetrical injection and establishes downstream the wall near the slot; the second is on a streamwise plane in the z direction where the recirculation zone is driven by the combustion products injection. The first mode is shown by vectors in Fig. 5.12 for two radial planes: half a slot height from the wall (y plane 1) and half the distance between the injection slot and the combustion products injection (y plane 2). The second mode is shown by vectors in Fig. 5.13 for two meridian planes: half a slot width (z plane 1) and half

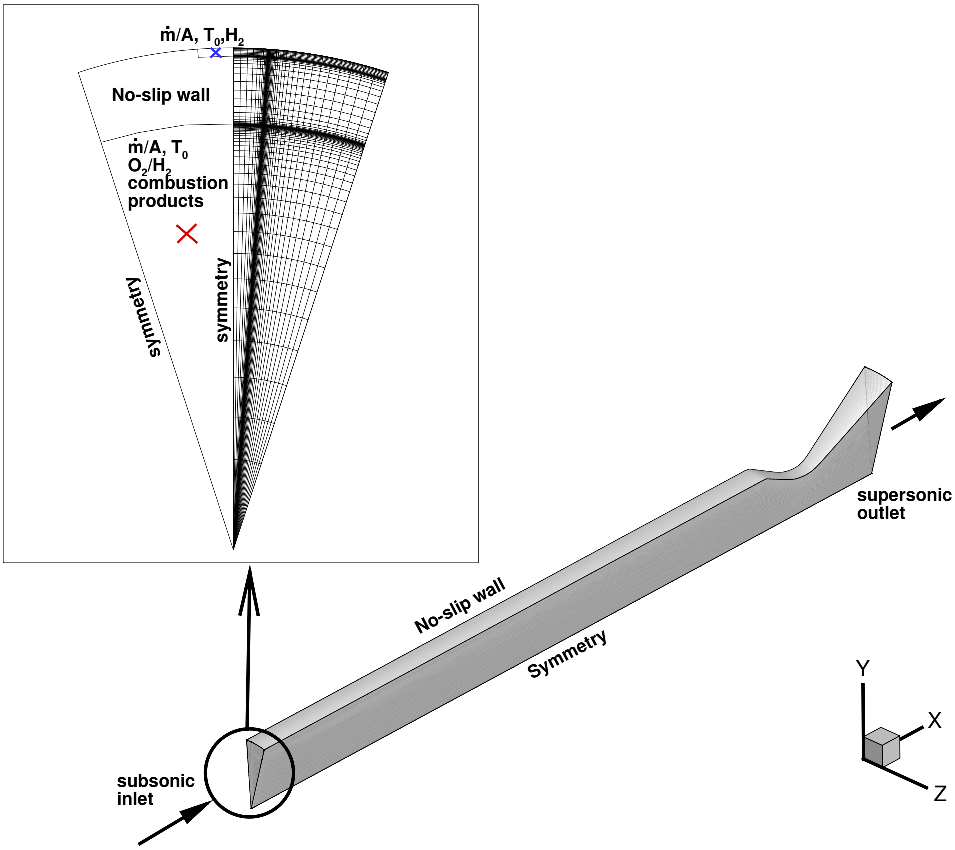

Figure 5.11: Oxygen/hydrogen film cooled thrust chamber three dimensional numerical simulation: numerical grid and boundary conditions.

empty space between two slots (z plane 2).

Two different views for the three dimensional temperature field are shown in Fig. 5.14 to highlight the film injection plane and its opposite plane. The numerical solution on these two planes are associated to the two dimensional axis-symmetric simulations described above for the thrust chamber with and without film cooling, respectively, whose solutions can be read as bounding values for the three dimensional evaluation.

The hydrogen injected through the film slot diffuses in both radial and crosswise direction as shown in Fig. 5.15, then its cooling action extends for a shorter section of the chamber, compared to the axis-symmetric configuration.

Wall heat flux for all the spanwise sections along the chamber is shown in Fig. 5.16(a) together with the two dimensional solutions obtained with and without film cooling. The two dimensional numerical solutions can be read as the bounding values for the three dimensional wall heat flux: the section near the slot shows a higher wall heat flux compared to the two dimensional solution. This can be ascribed to the spanwise diffusion which acts in reducing the efficiency of the film along the chamber with respect to the two dimensional configuration. On the other hand, the wall heat flux in the section between two slots is near the two dimensional solution without film cooling. This

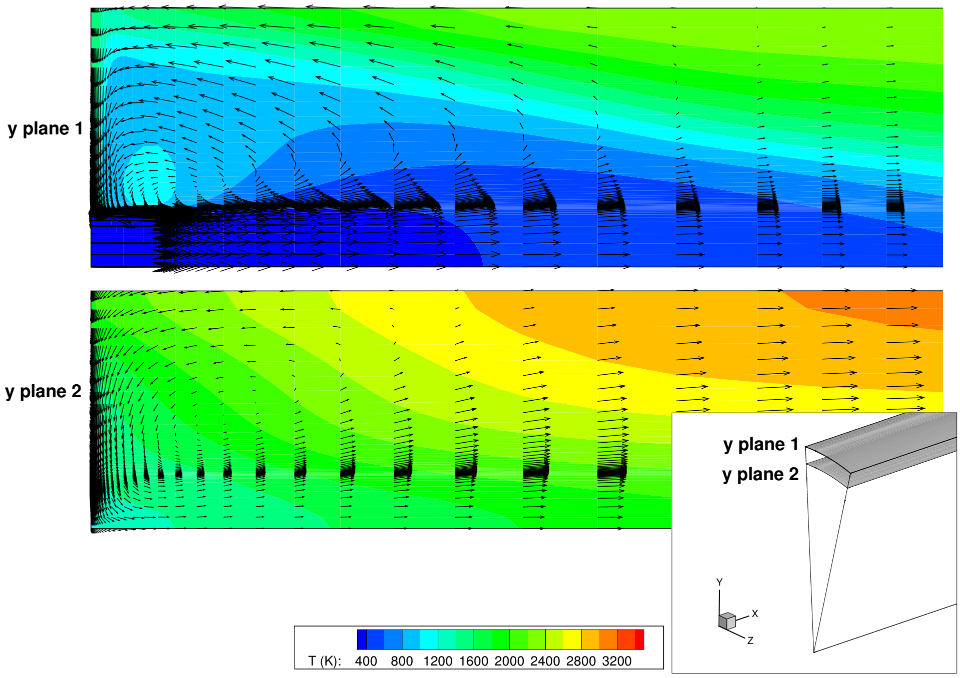

Figure 5.12: Oxygen/hydrogen film cooled thrust chamber three dimensional numerical simulation: y planes temperature fields and velocity vectors.

can be ascribed to the small influence of the film on this section because of the large distance between two adjacent slots. The comparison between numerical simulation and experimental data has been performed integrating the wall heat flux evaluated by means of the three dimensional numerical simulation in the spanwise direction. The resulting wall heat flux is shown in Fig 5.16(b) recalling the previous numerical results obtained with the two dimensional numerical simulations and the average heat flux evaluated by means of Eq. 5.1.

The average evaluation described in Eq. 5.1 neglect spanwise diffusion and overestimate the maximum wall heat flux achievable with a three dimensional configuration near the inlet section. Downstream the average heat flux underestimates the experimental wall heat flux due to the assumption that the film is still active whereas spanwise diffusion reduces film cooling efficiency along the chamber. Nevertheless, downstream of the heat peak related to the recirculation region which is visible in the average solution and does not appear in the three dimensional integral solution, the surface averaged solution slightly underestimate the three dimensional evaluation. This result confirms that in case of film slots with high width to height ratio arranged such that the distance between two slots is higher than the width of the slot, the wall heat flux along the chamber can be evaluated from two dimensional numerical simulations and than averaged as a function of the surface where the film acts. This approximation strongly reduces the computational cost for the wall heat flux estimation,

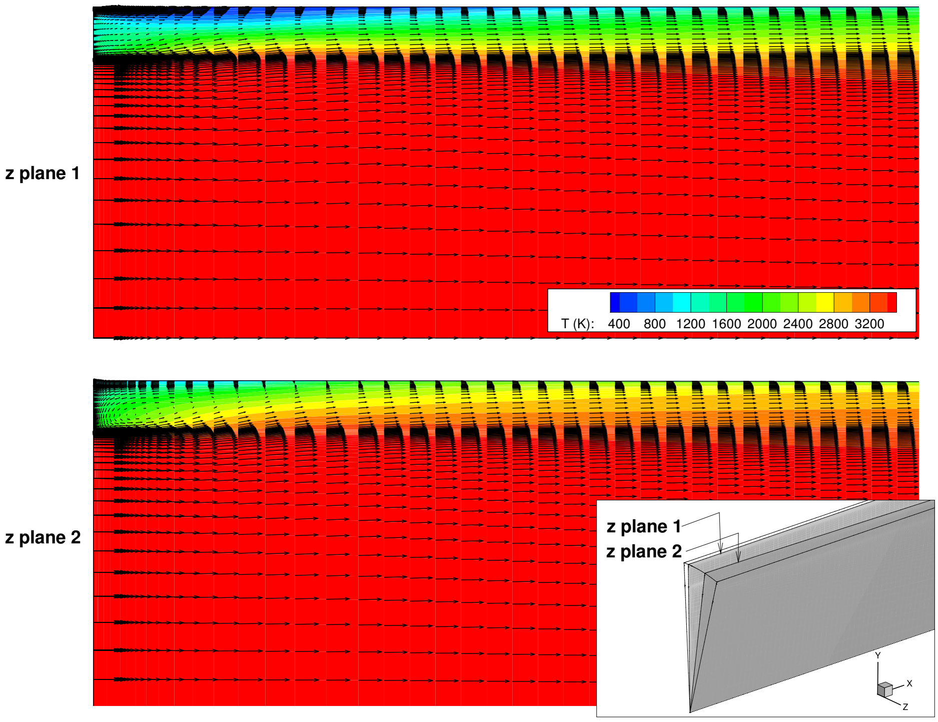

Figure 5.13: Oxygen/hydrogen film cooled thrust chamber three dimensional numerical simulation: z planes temperature fields and velocity vectors.

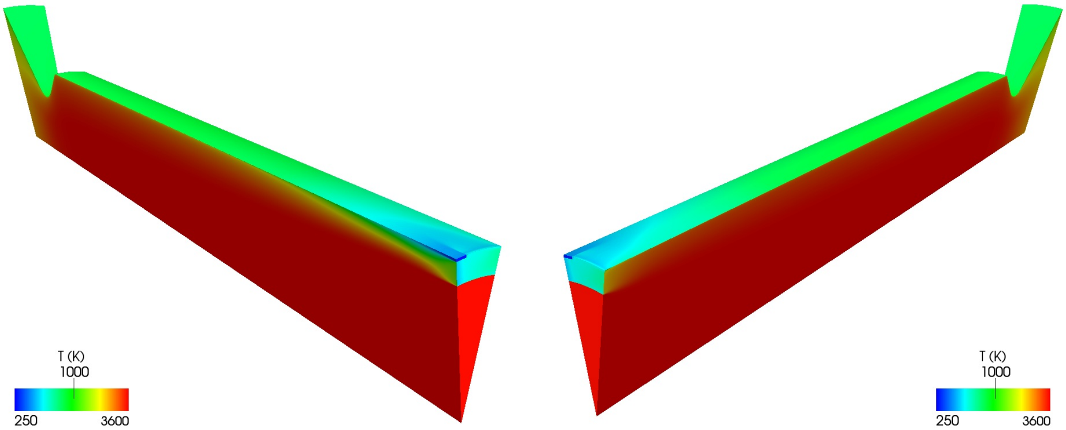

Figure 5.14: Oxygen/hydrogen film cooled thrust chamber: two views of the three dimensional temperature field. Left: film injection plane. Right: plane between two film slots.

being based on two dimensional instead of three dimensional numerical simulations.

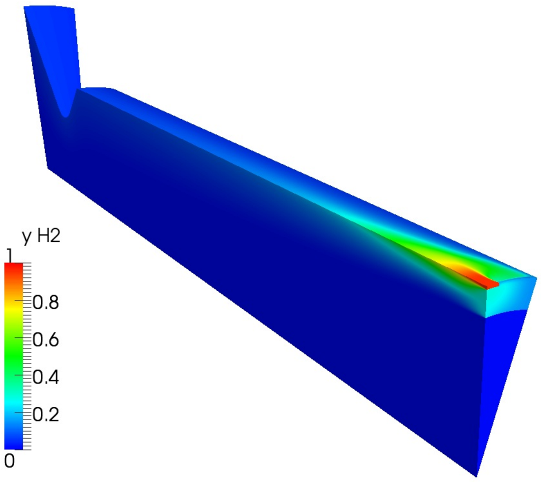

Figure 5.15: Oxygen/hydrogen film cooled thrust chamber: three dimensional view of the hydrogen mass fraction field.

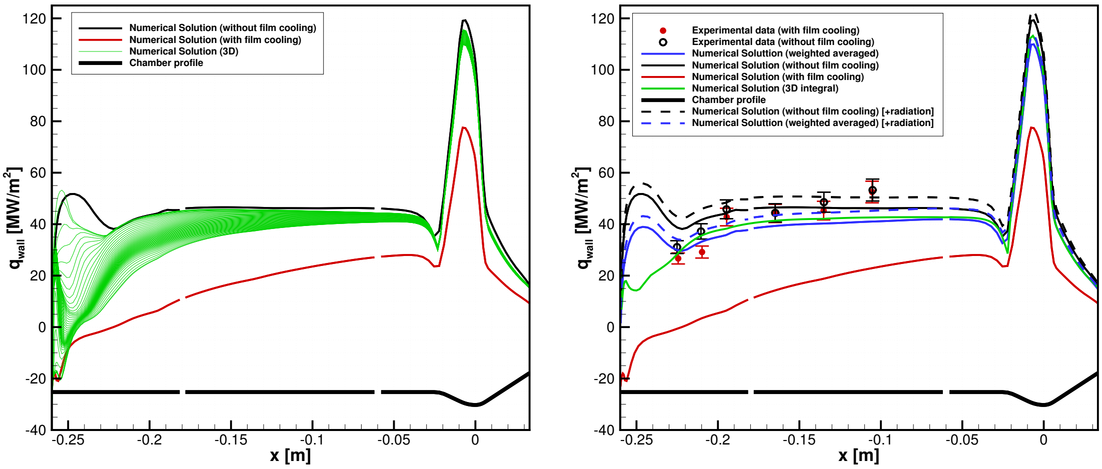

(a) Wall heat flux in spanwise sections with 2D axis-symmetric numerical solutions.

(b) Integral wall heat flux comparison against experimental data and 2D axis-symmetric numerical solution together with the weighted average wall heat flux evaluation.

Figure 5.16: Oxygen/hydrogen film cooled thrust chamber wall heat flux.

5.2.2 Oxygen/Methane film cooled thrust chamber

In the frame of the 7^{th} Framework Program within the “In-Space Propulsion 1” project, film cooling in oxygen/methane thrust chamber is being studied in terms of experiments and numerical simulations. In particular, the experimental test case[4, 77] consists in a low pressure calorimetric subscale combustion chamber where gaseous oxygen (O_2) and gaseous methane (CH_4) at ambient temperature are injected. Film

Run	Pressure [bar]	Mixture Ratio (O/F)
01 (nominal)	11.50	3.35
02	13.80	3.35
03	11.25	3.00

Table 5.5: ISP1 experimental test matrix for film slot height h=0.46 mm.

Species	Mass fraction
CO	0.258
CO_2	0.224
H	0.002
H_2	0.009
H_2O	0.378
O	0.014
OH	0.066
O_2	0.048

Table 5.6: Mixture composition in terms of mass fractions of the hot gas equilibrium combustion products at the nominal load point.

cooling is realized with gaseous methane injected through a 2D axis-symmetric circular slot. In the experimental test campaign, different chamber pressure, mixture ratio and film slot height have been investigated as shown in the test matrix summarized in Tab. 5.5 providing detailed axial distribution of heat pick-up based on water mass flow rate and surface temperatures.

Numerical simulations have been performed reproducing the experimental test matrix summarized in Tab. 5.5. Numerical grid and boundary conditions are similar to those described in Sec. 5.2.1 for the oxygen/hydrogen film cooled thrust chamber simulation. Nevertheless, in the present test cases, film cooling is injected in the thrust chamber through a circumferential slot, hence the simplified approach is able to match all the characteristic parameters relevant to the film cooling flow: film slot height, distance between film and injectors, film inlet velocity temperature and mass flow rate. Wall temperature measured by means of thermocouples is enforced as boundary condition at the wall and the resulting wall heat flux is compared to the experimental wall heat flux measurements provided. Oxygen/methane equilibrium combustion products evaluated from chamber pressure and mixture ratio are injected as a mixture whose composition is constant through the chamber ans it is listed in Tab. 5.6.

In Fig. 5.17 the multi-block grid designed for the numerical simulation is shown together with the temperature field relevant to the nominal test case (Run ♯01). In Fig. 5.18, wall heat flux along the thrust chamber is plotted comparing numerical simulation results and experimental data for Run ♯01 (nominal load point). As can be seen, numerical solution is in good agreement with the experimental data along the whole thrust chamber. In Fig. 5.19(a) the pressure effect of the wall heat flux is shown comparing the nominal load point test case (Run ♯01) and the test case with increased pressure (Run ♯02). Two different experimental test cases for the increased pressure run are plotted to highlight the experimental data scatter. Numerical simulations are able to capture the pressure increase effect over the wall heat flux, with a good agreement with experimental data. In Fig. 5.19(b) mixture ratio variation effect

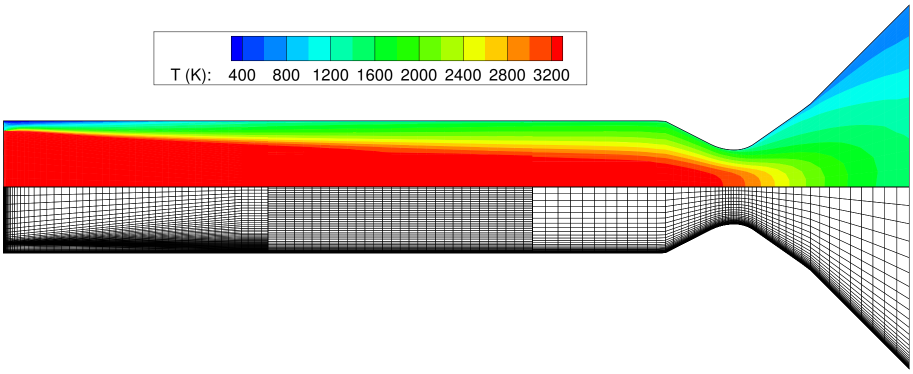

Figure 5.17: ISP1 project experimental test matrix nominal point: medium grid size numerical grid and temperature field.

is shown comparing numerical and experimental data of Run ♯01 and Run ♯03. As can be seen, both experimental and numerical wall heat flux are not affected by mixture ratio change inside the thrust chamber. This can be ascribed to the very high film mass flow rate injected (20% of the overall mass flow rate). It protects the wall from the high temperature mixture produced by combustion and its efficiency is not affected by the different mixture ratio inside the chamber.

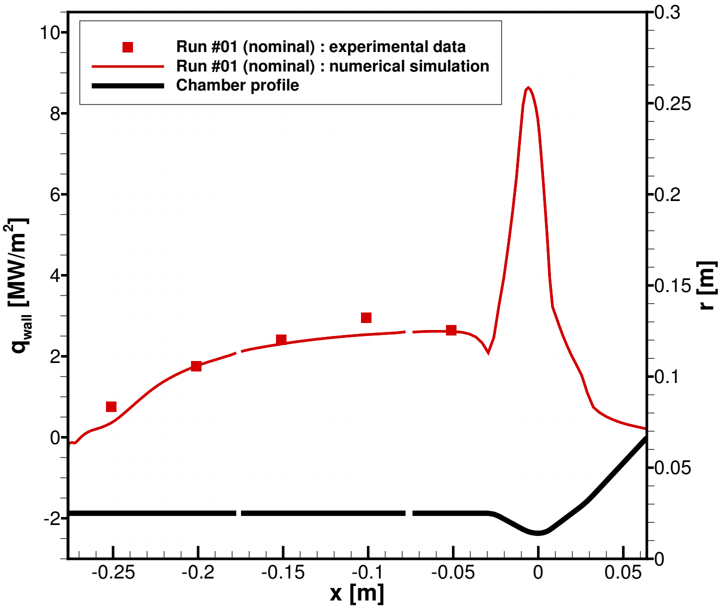

Figure 5.18: ISP1 project experimental test matrix nominal point: wall heat flux along the thrust chamber. Experimental measurements (circles) vs numerical solution (solid line).

Once the simplified approach has been validated against experimental data for

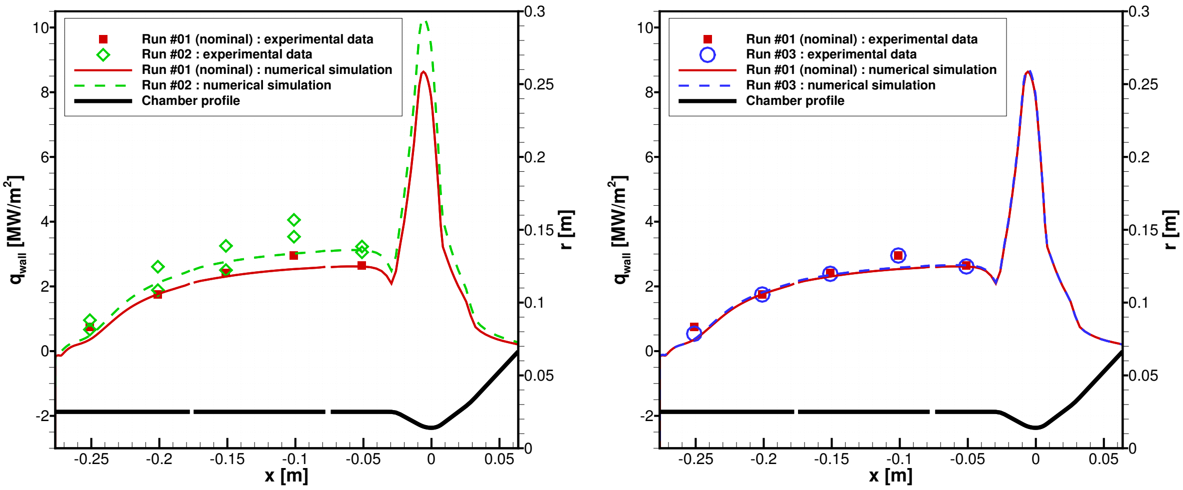

(a) Chamber pressure effect.

(b) Mixture ratio effect.

Figure 5.19: Wall heat flux along the thrust chamber: experimental measurements (symbols) vs numerical simulations (solid lines)

three different test cases evaluating its capability of reproducing pressure and mixture ratio effects on wall heat flux, a parametric analysis is performed around the nominal load point focusing on film cooling mass flow rate and film slot height effects. In particular, results are compared in terms of film cooling efficiency due to the lack of experimental data related to wall temperature and wall heat flux.

Film cooling efficiency parametric analysis

Film mass flow rate

Six different film mass flow rate percentages are investigated to evaluate their influence on the film cooling efficiency as summarized in Tab. 5.7. ISP 1 load point is reproduced in test case n. 6.

Increasing film mass flow rate with a constant slot height means to inject a faster film near the wall. As a consequence, it protects the wall from hot gas with increasing efficiency, as shown in Fig. 5.20. Nevertheless, increasing film mass flow rate considerably reduces the thrust chamber performance lowering the overall mixture ratio inside the thrust chamber.

Slot Height

Two different film slot heights are investigated with constant film mass flow rate percentage: s = 1 mm and s = 0.46 mm. These configurations are characterized by different inlet velocity and different distance between film and hot gas. In Fig. 5.21, film cooling efficiency with different slot height is plotted. Comparing film cooling efficiency initial plateau, the larger slot height ensures a wider plateau despite the lower inlet velocity because the hot core has to cover a larger distance to reach the

Test case	1	2	3	4	5	6
$\dot{m}_{film}$	7.5%	10.0%	12.5%	15.0%	17.5%	20.0%

Table 5.7: Mass flow rate parametric analysis test matrix.

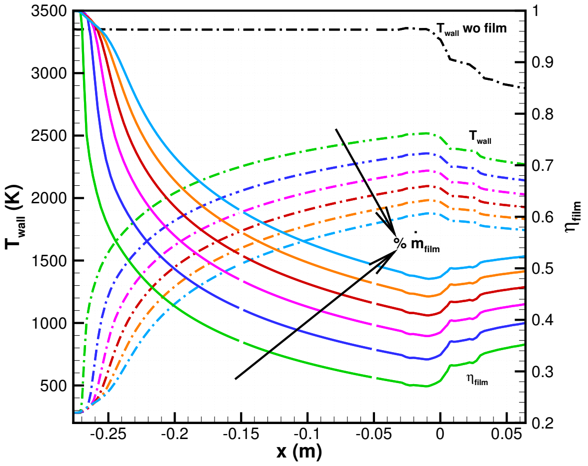

Figure 5.20: Film Cooling efficiency along the wall with different film mass flow rate.

wall. On the contrary, after film cooling breaking, the higher velocity of the smaller slot height case ensures a smoother efficiency decay.

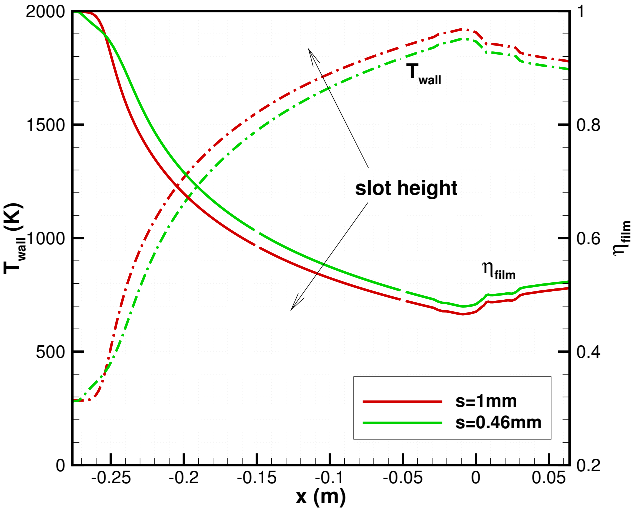

Figure 5.21: Film Cooling efficiency along the wall with different film slot height.

6

Regeneratively cooled thrust chambers

In order to keep the temperatures of the thrust chamber walls within their allowed limits, an intense cooling is necessary, which, in case of regenerative cooling, is achieved by flowing a coolant into suitable channels surrounding the thrust chamber. Due to the strongly coupled nature of the heat transfer problem, coolant and hot gas side cannot be studied independently. Coupled heat transfer problem of hot gas, chamber wall and coolant in thrust chambers is usually studied on the basis of one-dimensional analysis with Nusselt-type empirical equations [78, 79, 80]. Coupled analysis involving CFD hot-gas side evaluation, three dimensional heat conduction model and one-dimensional hydraulic model for the coolant flow has been performed by [81] for a LOX/hydrogen engine. Fully coupled multidisciplinary CFD simulation with heat conduction and quasi-one-dimensional water cooling channel model for a water cooled thruster nozzle has been conducted by [45]. Two validated thermal analysis codes have been conjugated in [82] via an interface file to design and analyze regeneratively-cooled rocket engine. Refining these models, axis-symmetric CFD model has been adopted for hot-gas side flow instead of the previous thermal analysis code in [83]. Recently, coupled analysis of a water-cooled nozzle has been performed by [84] with CFD for the coolant-cooling channel conjugate heat transfer and two different approaches for the hot-gas side: empirical models and CFD. All of these approaches have their well-defined objective that in some case leads to fast and simplified methods and in other cases to heavy computations which are not suited to engine design phase.

Objective of the present chapter is to develop a computational procedure able to describe the coupled environment among hot-gas, wall and coolant that occurs in most liquid rocket engines and to provide a quick and reliable prediction of thrust-chamber wall temperature and heat flux as well as coolant-flow characteristics, which takes into account the real fluid nature of the coolant and thermal stratification in the high-aspect-ratio cooling channels. In the present coupled analysis, hot-gas side is solved by means of the CFD solver described in Part I and the coolant flow and wall structure heat transfer is solved by a simplified *quasi-2D* approach, which widely relies on semi-empirical relations [85]. The *quasi-2D* model has been developed in [86, 87] to take into account for the thermal stratification inside the channels which cannot be neglected in rectangular cooling channels. In fact, it has a significant effect on the prediction of maximum wall temperature which is a critical design parameter.

The choice to adopt the CFD solver for the hot gas side heat transfer evaluation relies on its higher reliability to evaluate wall heat flux compared to semi-empirical relations, as shown in Sec. 4.1 for a convergent-divergent nozzle. In the following, the simplified approach adopted for the wall and coolant side heat transfer is described. Then the coupling procedure is illustrated and applied to a sample test case to prove its capability as a design support approach.

6.1 Coolant flow and wall heating model

A simplified *quasi-2D* approach [86, 87] is used to study the coupled problem of coolant flow and wall structure heat transfer in rectangular cooling channels of liquid rocket engine thrust chambers.

The cooling channel flow model is developed by using the steady-state conservation laws of mass, momentum, and energy, taking into account the effects of heat transfer and friction. In particular, the mass and momentum governing equations are written in a one-dimensional form, whereas a simplified arrangement of the 2D energy equation is considered. In fact, in the case of high aspect ratio cooling channels with asymmetric heating, the arising thermal stratification is strongly pronounced in the radial direction [88, 89, 90, 91, 92, 93, 94] and thus the fluid energy equation can be reduced to a 2D balance in the stream-wise direction and radial direction. For that reason this flow model is referred to as *quasi-2D*. Moreover, to accurately describe the wall heat flux, also the axial component of the fluid velocity u and the wall temperature T_w are assumed to vary along the radial direction. Likewise to 1D analysis the transverse velocity components v and w (radial, y, and circumferential, z, directions, respectively) are neglected because they are much smaller than u. According to the above hypotheses, the fluid pressure only depends on the stream-wise coordinate position $p = p(x)$, whereas the fluid temperature and axial velocity and wall temperature are left to vary also in radial direction: $T = T(x,y)$, $u = u(x,y)$ and $T_w = T_w(x,y)$. As a consequence also the derived thermodynamic properties, such as density and enthalpy, and the fluid molecular properties depend on both x and y. Finally, it is assumed that the velocity dependence on x and y can be expressed by separation of variables as:

$$u(x,y) = u_{mh}(x) \cdot F(y) \tag{6.1}$$

where the function $u_{mh}(x)$ represents the velocity at channel middle height while the function $F(y)$ represents the shape of the velocity profile, which is assumed also to depend on the temperature field.

The goal of the quasi-2D flow model is to describe high aspect ratio cooling channels with more detail than the 1D model, because of the energy balance discretization also in the radial direction. On the contrary, the standard 1D flow model takes into account only a single fluid temperature in a channel cross section, thus failing in the description of flow-fields with strong temperature differences.

The turbulent thermal conductivity, fluid skin friction and coolant-wall heat transfer coefficients are evaluated by semi-empirical relations provided in the literature. The model, aiming to the study of any fluid evolving through cooling channels, considers a generic equation of state, and thus the coolant fluid can be either a compressible gas, or a supercritical fluid or a liquid. To consider fluids other than perfect gas or incompressible liquid is mandatory in the case of methane as coolant in rocket engines, because its thermodynamic conditions in the cooling circuit of an expander cycle engine are quite close to the critical point. In this regime, the fluid cannot be modeled either as a perfect gas or as a liquid. The thermodynamic properties of methane can be evaluated by any accurate model or database for equation of state and transport properties like viscosity and thermal conductivity. Among them, thermophysical properties provided in [95] are selected in the present study.

Skin friction factor f_w and the Nusselt number Nu are modeled by means of Colebrook [96] and Sieder & Tate [97] semi-empirical relations, respectively. The properties are evaluated at the fluid pressure and temperature except the viscosity, which is evaluated at the wall temperature and takes into account for the variable properties of the coolant.

The capability of the present simplified approach to describe the regenerative cooling circuit has been validated comparing to detailed numerical results obtained with CFD [87], and it has been proved that it is able to capture the stratification effects inside high aspect ratio cooling channels such that generally adopted in the regenerative cooling circuit.

6.2 Hot gas - coolant flow coupling procedure

The *quasi-2D* model is able to solve the coupled wall and coolant flow evolution once thermal boundary conditions are provided. In particular, the model, suited to rectangular channels, requires thermal boundary conditions at the top and bottom walls, whereas symmetry is exploited for the channel side wall boundary conditions. The thermal boundary condition can be one of the following:

- assigned wall temperature;
- assigned heat flux;
- assigned convective heat transfer coefficient and adiabatic wall temperature.

On the outer side of the rectangular channel an “assigned heat flux” boundary condition is given, assuming zero heat flux, that is adiabatic wall. On the inner side, the hot gas side, where heat enters the channel, thermal boundary condition is obtained by the RANS solver. Of course, in principle, neither temperature nor wall heat flux are known, because they depend on the thermal equilibrium between flows and wall, so a first tentative solution has to be computed. This could be done for instance enforcing a first tentative distribution of wall temperature, then passing the resulting heat flux to the *quasi-2D* solver, compare the wall temperature computed by the *quasi-2D* model with the first tentative value and repeat the CFD computation enforcing the wall temperature computed by the *quasi-2D* solver iteratively until convergence is reached. Analogously it could be done by enforcing a first tentative heat flux distribution. Although this process could successfully converge, a more efficient way is that of enforcing convective heat transfer coefficient and adiabatic wall temperature. In fact in this case only the heat transfer coefficient has to be adjusted which only weakly depends on wall temperature. Therefore, the convective heat transfer coefficient approach is used to provide the boundary condition to the *quasi-2D* solver. In particular, the coupling procedure is described by the following steps:

1. RANS computation of the hot-gas flow, enforcing the wall temperature (T_w = 800 K at first iteration, the result provided by *quasi-2D* computation for the next iterations) as boundary condition and evaluation of the heat transfer coefficient h_c from the computed heat flux, the enforced wall temperature and the adiabatic wall temperature $T_{w,ad}$:
$$h_c = \frac{q_{wall}}{T_{w,ad} - T_w} \tag{6.2}$$
2. *quasi-2D* computation of the coupled coolant flow and wall thermal evolution using h_c values from step 2 and $T_{w,ad}$; the coupled coolant flow and wall analysis provides a new value of T_w.

Iterations are made repeating steps 1 & 2. The process ends when the difference between the computed values of T_w in two consecutive iterations is smaller than an assigned tolerance. The adiabatic wall temperature $T_{w,ad}$, needed to evaluate the convective heat transfer coefficient, can be evaluated by means of the recovery temperature definition as function of the Prandtl number and the static and stagnation temperature or by means of a CFD numerical simulation where the wall boundary condition is set as adiabatic.

6.3 Sample results

6.3.1 Test case description

The selected reference liquid rocket engine is the one discussed in [10], which is a oxygen/methane expander cycle engine studied theoretically with particular focus on regenerative cooling jacket design. On the basis of the system and parametric analysis carried out in [10], the following features of the thrust chamber, nozzle and cooling channel have been selected. Being interested in the coupling procedure, a full inlet approach (see Sec. 5.1) is adopted for the hot-gas side heat transfer evaluation. For the thrust chamber the assumed data are reported in Tab. 6.1. Gas mixture composition and chamber total temperature are calculated under the assumption of equilibrium combustion [23]. The resulting adiabatic flame temperature is 3603.20 K, and the most important species accounted for the mixture are: CO, CO_2, H, HO_2, H_2, H_2O, O, OH,

O_2. Nozzle geometry is designed by method of characteristics assuming a truncated ideal nozzle contour (Fig. 6.1). As attention was focused on cooling channel/thrust chamber coupling, only the whole convergent section and the part of the divergent section cooled with channels (up to $x_i = 25.1$ cm and $\varepsilon_i = 15$, see Tab. 6.2) have been considered in the RANS simulations.

Constant cross section cooling channels are considered whose main features are reported in Tab. 6.2.

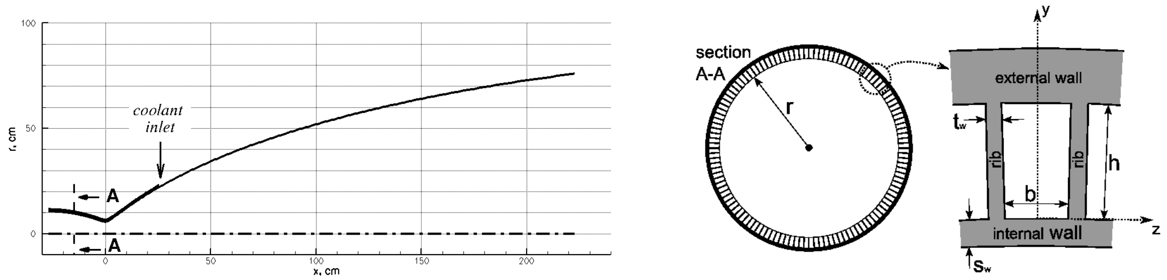

Figure 6.1: Schematic of nozzle and regenerative cooling channels.

Chamber pressure (p_c), bar	58.6
Mixture ratio (O/F)	3.5
Adiabatic flame temperature (T_{aw}), K	3603.20
Expansion ratio (ε_d)	180
Contraction ratio (ε_c)	3.5
Throat radius (r_t), cm	5.66
Divergent section length (L_d), cm	223.0
Convergent section length (L_c)	33.1

Table 6.1: Thrust chamber and nozzle data.

Note that the wall material is assumed as hydrodynamically smooth and its thermal conductivity is $k_w = 390$ W/m/K, that is typical of high-conductivity copper-alloys. The dimensions of the cooling circuit, composed of 150 rectangular channels, are plotted in Fig. 6.2 together with the thrust chamber radius.

6.3.2 Discussion

The approach described in Sec. 6.2 has been used to evaluate the performance of the regenerative cooling system of the engine test case described in Sec. 6.3.1. CFD simulations have been carried out on the grid shown in Fig. 6.3. Cells have been clustered towards the wall to correctly capture the turbulent kinematic and thermal boundary layer. Grid and clustering law have been selected after a grid convergence analysis performed over three grids halving cells in all directions at each refinement step, whose number of cells and minimum cell height are shown in Tab. 6.3.

width (b), mm	1.08
height (h), mm	8.63
Aspect ratio (λ)	8
Number of channels	150
Inlet section area ratio (ε_i)	15
Inlet section abscissa (x_i), cm	25.1
Internal wall thickness (s_w), mm	0.7

Table 6.2: Cooling channel data.

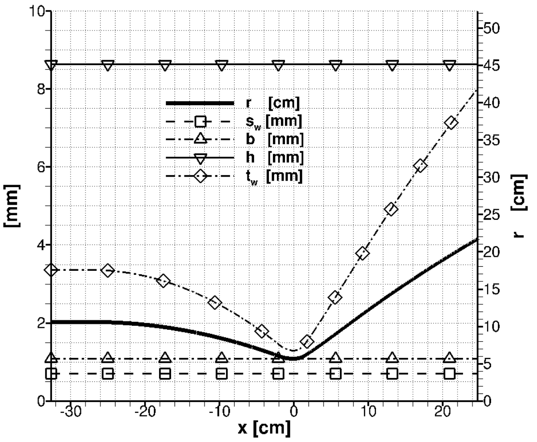

Figure 6.2: Features of the cooling circuit.

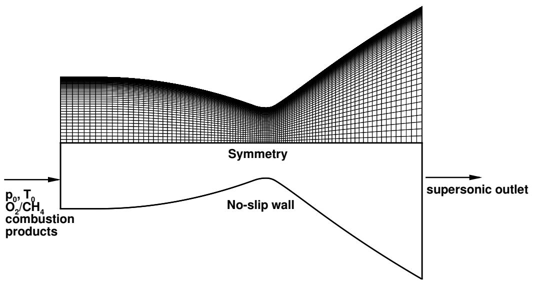

Figure 6.3: Medium grid size numerical grid and boundary conditions for the hot gas flow simulation.

Axial velocity profiles at the throat obtained with the fine, medium and coarse grids are shown in Fig. 6.4. Medium grid size numerical error evaluation is referred to the Richardson extrapolated solution (Eq. 4.2): numerical solution obtained with the medium grid size has a numerical error lower than 1% along the whole axial velocity profile.

The CFD simulation with adiabatic wall has been the first step leading to the solution shown in Fig. 6.5. The computed value of adiabatic wall temperature slightly decreases from a maximum of about 3600 K, at the combustion chamber entrance.

On the basis of the adiabatic CFD solution and of the CFD simulation carried out

Grid level	Number of cells	Δy_{min}
Coarse	50×45	2 μm
Medium	100×90	1 μm
Fine	200×180	0.5 μm

Table 6.3: Grid convergence analysis: grid number of cells and minimum cell height.

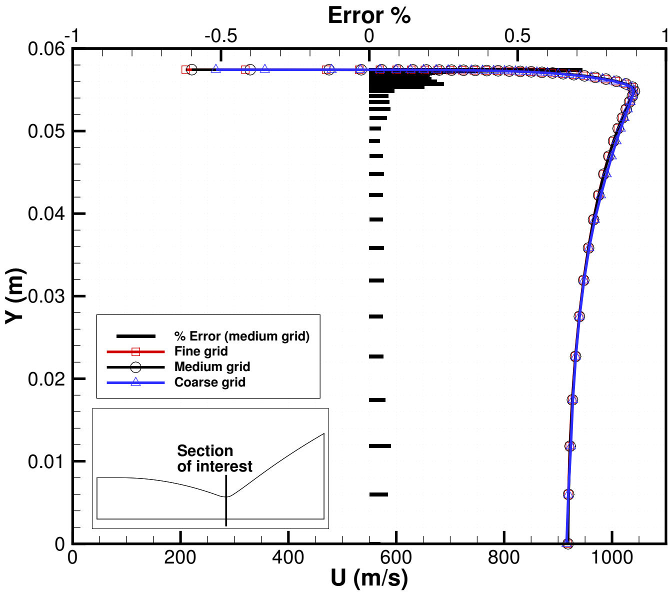

Figure 6.4: Axial velocity component profiles at the throat obtained with fine, medium and coarse grid levels. Medium grid size numerical error estimation referred to the Richardson extrapolated solution.

enforcing isothermal wall with $T_w = 800$K the first tentative solution for the convective heat transfer coefficient provided by CFD is obtained and passed to the *quasi-2D* solver of coolant flow and channel wall thermal evolution.

The computed heat transfer coefficient at the end of the first computation is shown in Fig. 6.6(a) (iter =0). Then the wall temperature computed by the *quasi-2D* model is passed as a boundary condition to the CFD solver, an updated value of h_c is evaluated on the basis of the new CFD solution and then it is passed back to the *quasi-2D* solver. The result is the new iteration solution for the heat transfer coefficient (iter=1 in Fig. 6.6(a)). Note that, convergence is rather fast and the second *quasi-2D* computation provides a result quite close. After three *quasi-2D* computations convergence is reached with a reduction of the error in the throat from 5% between the first two steps to 0.05% between the last two steps. Hot gas side wall temperature evaluated by the *quasi-2D* model for each step is shown in Fig. 6.6(b). The maximum difference in wall temperature decreases from 4% between the first two steps to 0.26% between the last two steps in section $x = -0.2$ m.

As discussed in Sec. 4.1, semi-empirical correlations such as Bartz's correlation can be used to evaluate the hot gas side convective heat transfer coefficient. Nevertheless, Bartz's correlation appears not accurate as a predictive tools but it is able to properly fit the experimental data once calibrated. Here, the influence of a different evaluation of the hot gas side heat transfer coefficient is evaluated in the coupled heat transfer problem. The test case described in Sec. 6.3.1 is reproduced evaluating the hot gas side coefficient with the Bartz's correlation (Eq. 4.4) and the CFD numerical solution

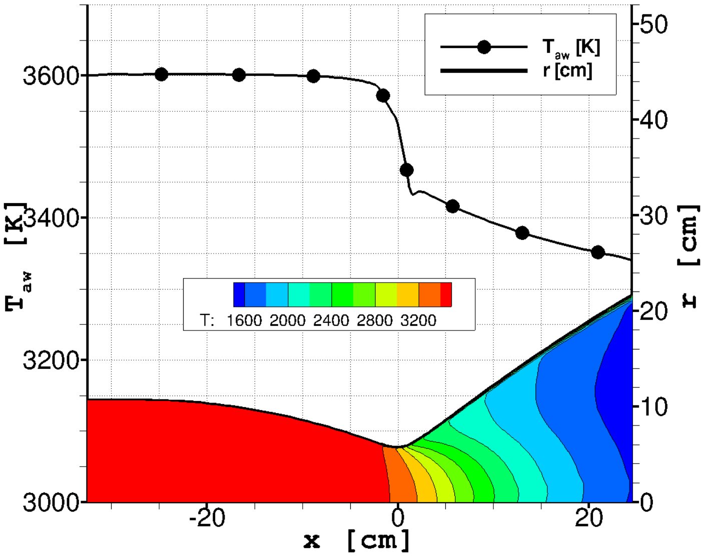

Figure 6.5: Wall temperature and temperature field in the nozzle in case of adiabatic wall.

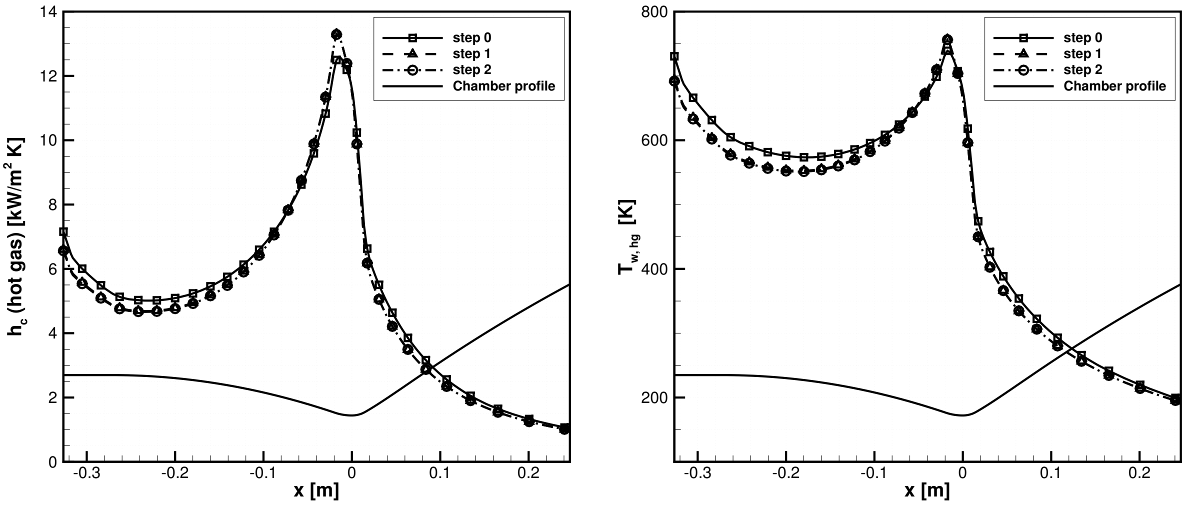

(a) Convective heat transfer coefficient.

(b) Hot gas side wall temperature.

Figure 6.6: Coupled approach convergence history.

presented above. Wall heat flux along the chamber is shown in Fig. 6.7(a): the Bartz's correlation gives a higher wall heat flux compared to the CFD solution in all the thrust chamber except the inlet section where the CFD solution show a higher heat flux related to the injection approach as discussed in Sec. 5.1. As a consequence of the heat transfer balance, hot gas side wall temperature is higher in the Bartz's case than in the CFD solution as shown in Fig. 6.7(b) reaching the maximum temperature in the throat ($\sim$ 1000 K for Bartz's correlation and less than 800 K for the CFD solution). Furthermore, coolant temperature and stagnation pressure along the cooling channels are shown in Fig. 6.7(c) and 6.7(d), respectively. Again, Bartz's correlation gives higher coolant temperature and higher pressure drop in the cooling channels compared to the CFD solution.

These results confirm that the Bartz's correlation provides a conservative evaluation of the hot gas side and coolant properties in the heat transfer coupled problem. On the other hand, the hot gas side CFD solution has proven to provide wall heat flux evaluation in better agreement to experimental data than Bartz's correlation (see Sec. 4.1) and in the coupled problem the higher fidelity of numerical solution can be important in the design optimization where small margins are tolerated in order to achieve better performance.

Each component of the loose coupled analysis (hot gas side heat transfer evaluation and wall and coolant side quasi-2D approach) have been validated separately. The present coupling method has not been validated as a whole approach due to the lack of well documented experimental test case for this coupled problem. Nevertheless, the results obtained in the coupled analysis are in line with those of typical engine configurations in terms of hot gas wall temperature and coolant pressure drop inside the cooling channels.

The present coupling approach will be employed in Ch. 8 for the analysis of a full scale expander cycle engine to study the coupled heat transfer process between hot gas and coolant.

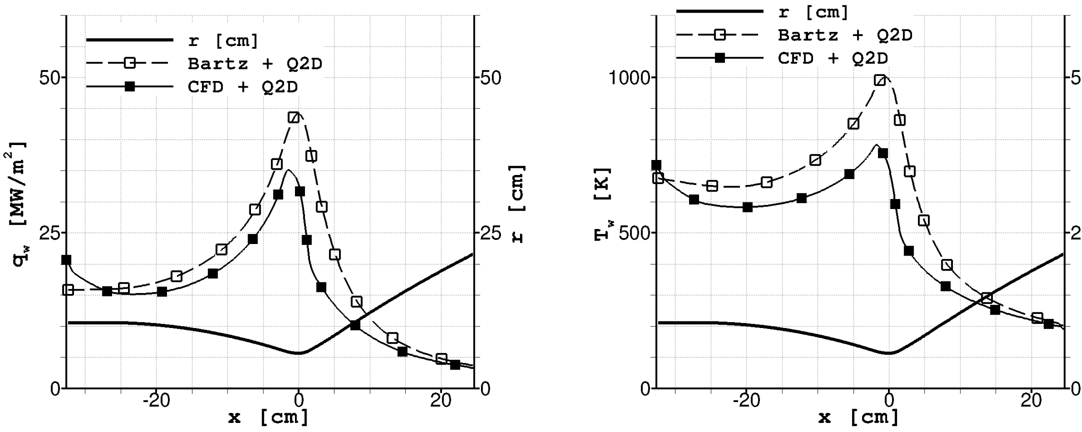

(a) Wall heat flux

(b) Hot gas side wall temperature

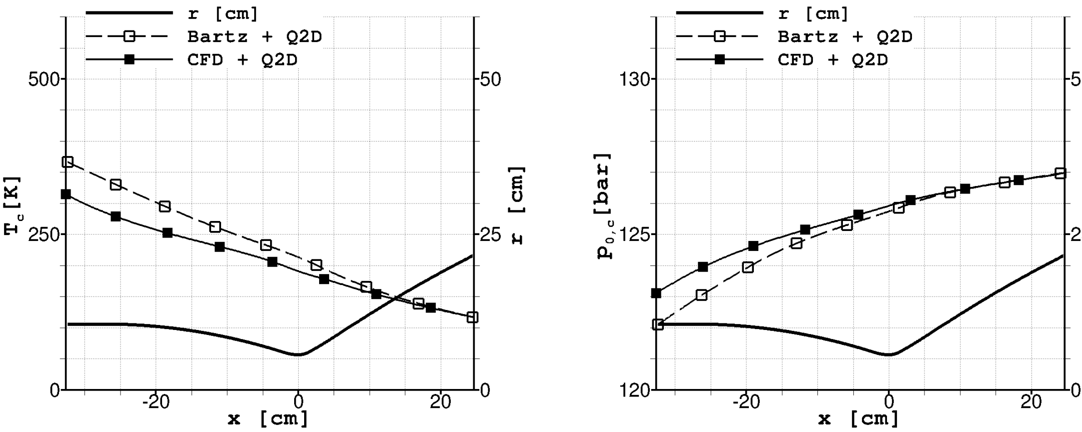

(c) Coolant temperature

(d) Coolant stagnation pressure

Figure 6.7: Coupled analysis: Bartz's correlation against CFD numerical evaluation.

7

Expander cycle engine thrust chamber with ribbed walls

The understanding and prediction of heat transfer characteristics, heat pick-up and wall temperature distribution in the thrust chamber are key features for the development of high performance engines, especially in the case of expander cycle. In fact, in these cycles the driving power for the turbo-pumps comes from the fuel used as a coolant in the regenerative cooling circuit. Expander cycle engines are an attractive solution for upper stage and in-space propulsion because of their capability for multiple restarts and throttling. They have the simplest configuration among the pump-fed cycles because they do not require components such as gas generators or pre-burners. Development and testing of expander cycle engines continues to be of interest for industries and space agencies, as demonstrated by the studies on RL-10 in all its configurations in US since '60 [19, 98], on RD0146 in Russia [20], on LE-5B in Japan [99], and on Vinci in Europe [18]. All of these expander cycle engines are operated with oxygen/hydrogen propellant combination. Although no known oxygen/methane engines have been flown for aerospace applications, space agencies in the US, Russia, Europe and Japan [100] have been also considering methane fueled propulsion system for various applications. The heat transfer enhancement required by the coolant fluid to drive the turbopumps can be achieved with two design options with the goal of increasing the chamber surface: lengthened chambers and increased chamber perimeters. In particular, the second design option can be obtained by means of ribs characterized by rectangular or trapezoidal cross sections arranged in the same direction of the flow in the cylindrical section of lengthened thrust chambers for expander cycle engines.

Similar configurations of axial ribs or *riblets* are widely employed to reduce drag in different flows related to oil & gas, aeronautical, and naval applications. Due to the large computation effort required by DNS in the thrust chamber like regime [101, 102], the optimization of ribbed surfaces can be guided by RANS CFD, whose turbulence model has to be able to capture the main phenomena of the viscous sublayer. In particular, eddy viscosity models are affected by the uncertainty related to the definition of the vicinity of the wall needed in the destruction term [103]. In this case, the riblet can be treated as wall roughness whose effect is to shift the logarithmic law inside the boundary layer [104]. Nevertheless, due to the lack of experimental data for tuning, comparing and validating the correction, the Spalart-Allmaras modified turbulence model proposed in [104] strongly depends on the rib cross section geometry and the correction has been defined only for V-shaped and U-shaped ribs. Two-equations models such as $k-\varepsilon$ and $k-\omega$ are not affected by wall distance definition but are characterized by isotropic normal stresses. Therefore, in order to mimic the secondary motions, which have been identified as the driving phenomena of the drag reduction and the heat transfer increase, two-equations models have been modified to take into account for the anisotropy of the stress tensor [103, 105]. The analyses conducted with these models show that, for low Prandtl number fluids, taking into account for the secondary motions induces negligible effects on the flow and the thermal field around the riblet surface [105].

In liquid rocket thrust chambers, the difference between the wall and the hot gas temperature reaches few thousands K which is far from the conditions investigated in experimental tests devoted to drag reduction analysis [106, 107, 108]. For thrust chamber applications, rib heat transfer enhancement efficiency has been investigated experimentally [109, 110] and numerically [111] in oxygen/hydrogen subscale thrust chambers. The lack of experimental and numerical analysis in this specific application inspired the present chapter to evaluate how rib height affects the heat transfer enhancement efficiency of a ribbed thrust chamber.

First, the capability of the full inlet simplified injection approach to evaluate rib efficiency is validated reproducing an experimental test case and comparing the numerical results with the experimental measurements provided in the reference work. Then, the influence of the wall temperature crosswise variation is investigated comparing the wall heat flux obtained by a coupled numerical simulation accounting for the heat conduction inside the solid material and an isothermal numerical simulation. Finally, a parametric analysis is performed varying the rib height to evaluate how the surface increase reflects on the heat transfer enhancement.

7.1 Rib characterization

Axial ribs for heat transfer enhancement are placed along the cylindrical section of the thrust chamber, as shown in Fig. 7.1, which in case of expander cycle engine can be longer than in other engine cycles. As ribs are designed to increase the surface in the cylindrical region, at the end of the ribbed section the nozzle contour is smooth.

In these specific applications, ribs are usually characterized by rectangular or trapezoidal cross section whose geometrical description is given in terms of base (b), pitch (p), tip (t), height (h) and the tapering angle (α) as defined in Fig. 7.2.

In the flow regime which establishes inside a thrust chamber, rib height is lower than the turbulent boundary layer thickness whose thickness can be evaluated as a function of the Reynolds number based on the distance from the flat plate leading edge [112]:

$$\delta = 0.382\frac{x}{Re_x^{1/5}}$$

Hence, ribs are completely immersed inside the turbulent wall boundary layer

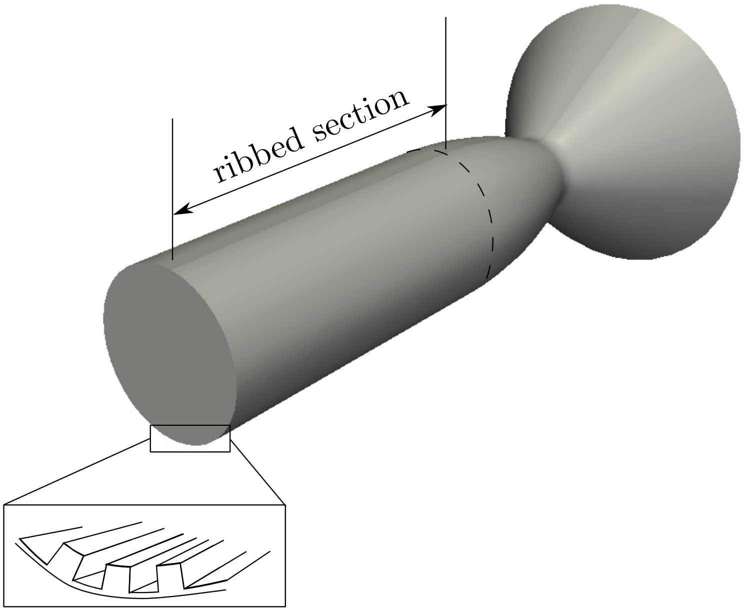

Figure 7.1: Axial ribs arrangement in the cylindrical section of the thrust chamber.

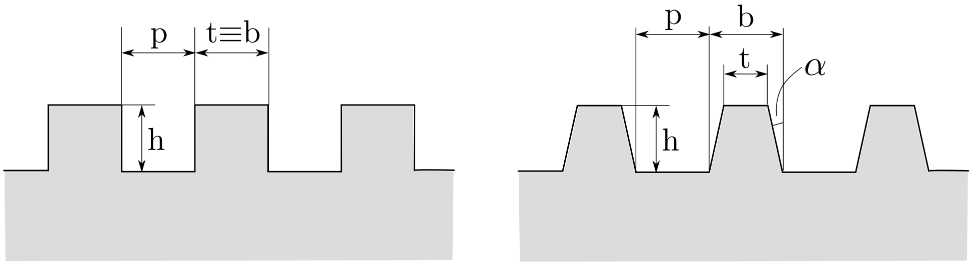

rectangular section

trapezoidal section

Figure 7.2: Rectangular and trapezoidal rib geometrical features.

along the thrust chamber as shown in Fig. 7.3.

The surface increase related to wall ribs with respect to a smooth thrust chamber can be expressed in terms of the number of ribs (N_{rib}), rib height and chamber radius r_c:

$$\frac{\Delta A}{A_{smooth}} = \frac{A_{rib} - A_{smooth}}{A_{smooth}} = \frac{N_{rib}\; h/cos\alpha}{\pi r_c}$$

where A_{rib} and A_{smooth} are the wet surfaces of the same thrust chamber with and without ribs, respectively. The measure of the surface increase efficiency in enhancing the heat transfer from the hot gas side to the wall is given by the rib efficiency defined as the ratio between the heat transfer increase and the surface increase of the ribbed thrust chamber referred to the same thrust chamber with smooth walls:

$$\eta_{rib} = \frac{\Delta q / q_{w,smooth}}{\Delta A / A_{smooth}} \tag{7.1}$$

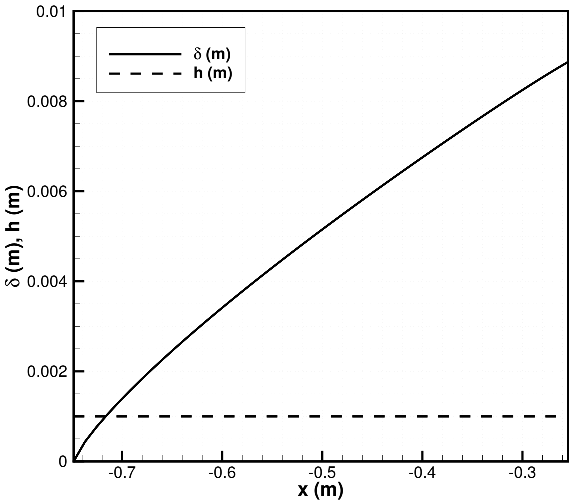

Figure 7.3: Turbulent wall boundary layer thickness along the chamber and rib height.

where Δq is the difference between wall heat flux of the thrust chamber with ribbed $q_{w,rib}$ and smooth $q_{w,smooth}$ walls.

In particular, to take into account the overall heat flux entering the wall material in the ribbed wall case, the heat flux is integrated over the wet surface A_{rib} and divided by the projected surface (i.e. the chamber perimeter if no rib is placed per unit area), whose definitions are shown in Fig. 7.4. Ribs efficiency is 1 when wall heat flux enhancement is equal to the surface increase, whereas it is 0 when the the ribbed configuration does not provide an heat flux increase compared to the smooth test case.

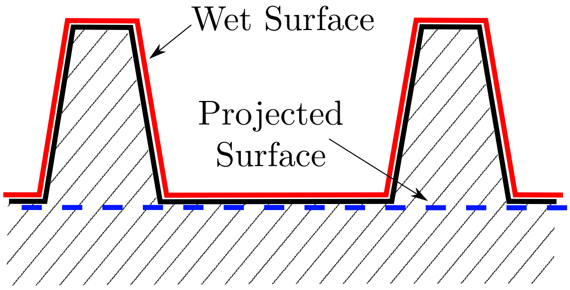

Figure 7.4: Wet and projected surface definition.

7.2 Validation

7.2.1 Experimental test case

To validate the capability of the solver to capture the heat transfer enhancement due to ribbed walls, an experimental test case retrieved in open literature is reproduced. It was designed in the frame of the Orbital Transfer Rocket Engine Technology Program [113] to choose the appropriate rib configuration for the hot-fire test evaluation of an expander cycle engine thrust chamber. The experimental test here reproduced consists in a calorimetric test chamber designed to allow different rib cross section geometries to be tested in the same set-up. The cylinder thrust chamber is composed by four 90 degree test panel segments, where one of the four panels has a smooth wall for reference heat transfer values and the other three panels have ribbed walls with different rib geometry. Hot air at prescribed stagnation temperature (764.26 K) and pressure (20.20 bar) flows inside the thrust chamber. The panel is composed by an oxygen-free high conductivity (OFHC) copper liner where rectangular axial cooling channels are machined. Water at ambient temperature flows counter-wise in the cooling channels arranged in correspondence of the hot-gas wall ribs. Inlet and outlet water temperature measurements are provided together with water temperature along the chamber.

To the present aim, only one rib geometry is selected to be reproduced besides to the smooth wall reference case. In particular, selected rib and channel geometries are shown in Fig. 7.5 and summarized in Tab. 7.1.

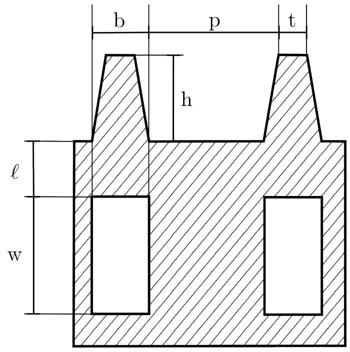

Figure 7.5: Ribbed wall thrust chamber: ribs geometrical features [113].

Chamber	radius (r_c), mm	60.96
	cylinder length (L), mm	457.2
Rib	base (b), mm	1.016
	height (h), mm	1.524
	tip (t), mm	0.508
	pitch (p), mm	2.000
	surface increase, %	85.61
Liner	thickness (ℓ), mm	3.556
Channel	base (b), mm	1.016
	height (w), mm	2.032

Table 7.1: Ribbed wall thrust chamber geometrical features for the selected test case.

Due to the complexity of the test set-up, only water temperature measurements along the chamber are available. As direct measurements on the hot-gas side are not available, numerical simulations are carried out with a coupled approach to solve the balance between hot-gas side convective heat transfer, solid conductive heat transfer and water coolant convective heat transfer. Hot-gas side is solved by means of the present RANS equations solver, whereas solid conductive and water coolant convective heat transfer are modeled by the simple 1D approach described in the following.

7.2.2 Hot gas - wall - water coolant coupling procedure

The present simplified coupling approach relies on the coupling procedure described in Ch. 6 where wall and coolant modeling is further simplified to treat water as a coolant. The heat transfer balance is solved via a loosely coupled procedure that can be summarized in the following steps:

1. RANS computation of the hot-gas flow, enforcing the wall temperature (T_w = 300 K at first iteration, the result provided by 1D computation for the next iterations) as boundary condition and evaluation of the convective heat transfer coefficient h_c (Eq. (6.2)) from the computed heat flux, the enforced wall temperature and the adiabatic wall temperature $T_{w,ad}$;

2. 1D computation of the coupled coolant flow and wall thermal evolution using h_c values from step 1 and $T_{w,ad}$; the coupled coolant flow and wall analysis provides a resulting value of T_w.

Iterations are made repeating steps 1 & 2. The process stops when the difference between the computed values of T_w in two consecutive iterations is smaller than an assigned tolerance. The adiabatic wall temperature $T_{w,ad}$, needed to evaluate the convective heat transfer coefficient, can be evaluated by means of the recovery temperature definition as function of the Prandtl number and the static and stagnation temperature or by means of a CFD numerical simulation on the same numerical grid of that of step 1 where the wall boundary condition is set as adiabatic.

The liner conduction and the water coolant convection are described by means of a simple 1D model, solving the space marching problem described by the two steady-state balances of three heat fluxes: from hot gas to wall; through the wall; and from wall to coolant. These balances can be written as:

$$q = h_{hg}\left(T_{w,ad} - T_{w,hg}\right) = k\left(\frac{T_{w,hg} - T_{w,c}}{\ell}\right) = h_{co}\left(T_{w,c} - T_c\right) \tag{7.2}$$

where q is the heat flux per unit area, h_{hg} and h_{co} are the convective heat transfer coefficients at hot-gas and coolant side, respectively, $T_{w,ad}$, $T_{w,hg}$, $T_{w,c}$ are adiabatic, hot-gas and coolant wall temperatures, respectively, and T_c is the coolant temperature, k is the thermal conductivity of the liner material ($k = 387$ W/(m K) for OFHC copper) and ℓ is the liner thickness. Assuming that all the heat coming from the hot-gas side ($q\,A$) is taken in from the coolant increasing its temperature, the following relation can be written:

$$q\,A = \dot{m}_c C_c \Delta T_c \tag{7.3}$$

where $\dot{m}_c$ is the coolant mass flow rate, C_c is the coolant specific heat and ΔT_c is the coolant temperature increase. The latter can be evaluated for each discretized section of the cooling channel (i) combining Eq. (7.2) and Eq. (7.3) starting from the coolant temperature in the previous section ($i-1$):

$$T_c(i) = T_c(i-1) + \frac{H\left(T_{w,ad}(i-1) - T_c(i-1)\right)\cdot \pi r/2}{\dot{m}_c\, C_c}\Delta x \tag{7.4}$$

where r is the chamber radius, Δx is the space discretization relevant to the cooling channel and H is the equivalent heat transfer coefficient defined as follows:

$$H = \frac{1}{\dfrac{1}{h_{hg}} + \dfrac{\ell}{k} + \dfrac{1}{h_{co}}}$$

Eq. 7.4 is written for a quarter of the chamber recalling the test case design. Hot-gas convective heat transfer coefficient and adiabatic wall temperature come from the CFD numerical simulation, coolant convective heat transfer coefficient is evaluated from the Nusselt number definition:

$$h_{co} = \frac{k_c}{D_h} Nu$$

where k_c is the thermal conductivity of the coolant, D_h is the hydraulic diameter of the cooling channel and Nu is the Nusselt number evaluated by means of the Dittus-Boelter correlation[114] for internal turbulent flows:

$$Nu = 0.023\ Re^{0.8}\ Pr^{0.4}$$

Once T_c is evaluated with Eq. 7.4, $T_{w,c}$ and $T_{w,hg}$ are computed from Eq. 7.2 and thus the step 2 is completed. Step 1 is then repeated enforcing the new hot-gas wall temperature as boundary condition of the CFD numerical simulation.

7.2.3 Numerical simulations

Two dimensional axis-symmetric and three dimensional RANS computations are carried out to study smooth and ribbed wall test chamber, respectively, taking into account only the barrel section of the chamber where experimental measurements are collected. Grid and boundary conditions enforced are shown for the smooth reference case, Fig. 7.6(a), and the selected ribbed case, Fig. 7.6(b), whose geometrical features are summarized in Tab. 7.1. The smooth case is treated with a single-block 2D axis-symmetric grid composed by 40×60 cells in axial and radial direction, respectively. The three dimensional grid for the ribbed wall case is composed by 96000 cells divided in 4 blocks as highlighted by the exploded view in Fig. 7.6(b). Cells are clustered toward the walls (i.e. pitch, height and tip of the rib along the chamber) to resolve thermal and kinematic boundary layer. Mass flow rate per unit area, total temperature, mixture composition and velocity direction are prescribed at the subsonic inflow boundary adopting the full inlet approach discussed in Sec. 5.1, whereas static pressure is enforced at the subsonic outflow boundary to preserve mass flow rate. The first guess wall temperature enforced in both smooth and ribbed wall case is 300 K. Then in the coupling process, the hot gas side wall temperature evaluated by means of the 1D model described in Sec. 7.2.2 is enforced. In the ribbed wall test case, the wall temperature is assumed constant in the crosswise direction. The convergence is reached after few iterations as shown in Fig. 7.7 for the reference smooth test chamber.

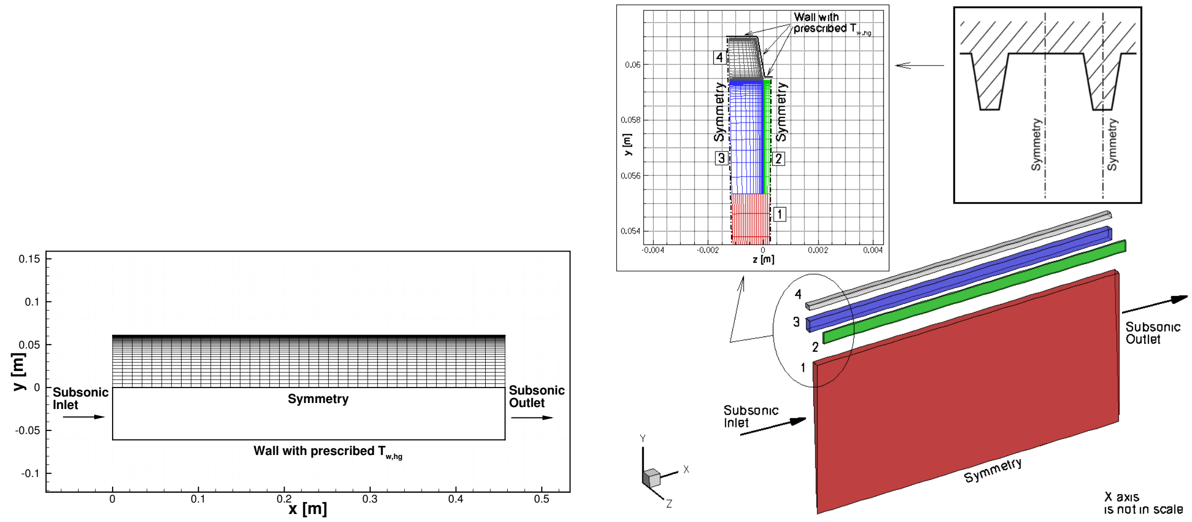

(a) Smooth wall grid and boundary conditions enforced.

(b) Ribbed wall grid (exploded view) and boundary conditions enforced. Enlargement of a x section (top).

Figure 7.6: Wall hot-gas side grid and boundary conditions enforced for smooth and ribbed test chamber [113].

Comparison of the coolant temperature increase obtained with the present numerical coupling procedure in the case with a smooth wall and with a ribbed wall against experimental measurements are shown in Fig. 7.8. Filled and empty circles represent the coolant temperature measurements along the chamber in the panels with and without ribs, respectively. Measurement errors have not been discussed in details in the reference work mainly because the test case was designed for experimental parametric analyses and comparison between different geometrical configurations. Solid and dashed lines represent the coolant temperature increase in the panels with and without ribs, respectively, evaluated with the coupling procedure described in Sec. 7.2.2. Numerical inlet coolant temperature enforced as an initial condition for the 1D coolant model are obtained by a linear extrapolation of the experimental measurements. As described in the reference work, the first and the last temperature measurements can be read as bulk temperatures, whereas the remaining measurements are local temperatures. As shown in Fig. 7.8, water temperature along the chamber evaluated by means of the simplified coupled procedure follows the experimental temperature measurements and the maximum error in both smooth and ribbed panels is 5%.

Smooth wall test case	$q_{wall,\ smooth}$	0.3354 MW/m^2
Ribbed wall test case	$q_{wall,\ ribbed}$	0.5286 MW/m^2
Surface increase	$\Delta A/A_{smooth}$	86.74 %
Rib efficiency	η_{rib}	66.42%

Table 7.2: Rib efficiency evaluation.

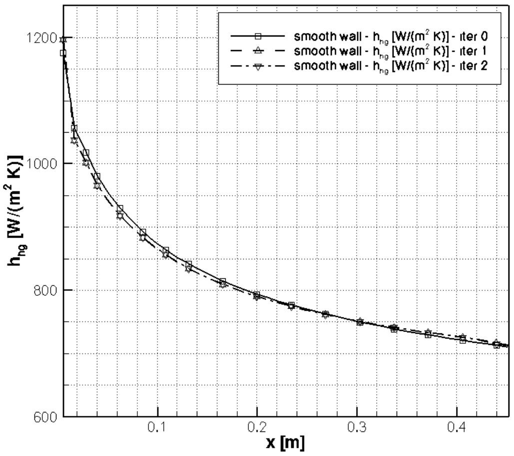

Figure 7.7: Hot-gas side convective heat transfer coefficient convergence history. Smooth test chamber.

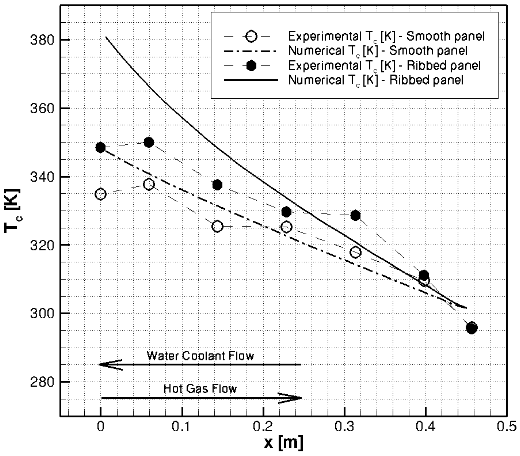

Figure 7.8: Coolant temperature increase: numerical solution vs experimental data. Filled circles and solid line for the panel with ribbed wall. Empty circles and dashed line for the panel with smooth wall[113].

Wall heat flux values in the case with and without ribbed wall are summarized in Tab. 7.2 and rib efficiency is evaluated recalling Eq. 7.1.

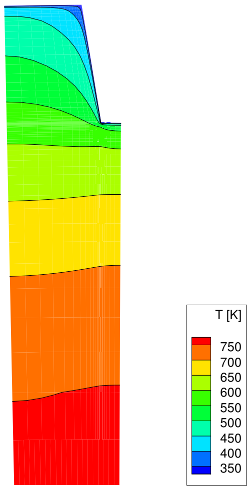

Figure 7.9: Temperature field in a crosswise section of the ribbed wall test case.

Rib efficiency can be associated to the temperature field stratification which establishes between two adjacent ribs as shown in Fig. 7.9. In particular, the average temperature between two ribs is lower than the core temperature hence the wall heat flux through the rib walls is driven by a weaker temperature gradient compared to the smooth test case. Hence, the heat flux enhancement is lower than the surface increase achieved by wall ribs as measured by the rib efficiency.

7.3 Ribbed wall heat transfer analysis

7.3.1 Test case description

The good agreement between numerical solution and available experimental data presented in Sec. 7.2.3 confirms that the full inlet approach can be adopted to study ribbed thrust chambers. Here a sample test case is presented to investigate heat transfer enhancement and rib efficiency in an expander cycle engine configuration. The reference thrust chamber is derived from the expander cycle thrust chamber studied in [10] and analyzed in Ch. 6. In particular, the cylindrical section upstream of the nozzle has been lengthened and modified by the introduction of axial ribs with rectangular cross section whose characteristics are summarized in Tab. 7.3 referring to Fig. 7.2 for the geometrical feature definition.

Chamber	Pressure (p_c), bar	58.6
	Propellants	O_2/CH_4
	O/F	3.5
	Adiabatic flame temperature (T_{ad}), K	3603.20
Nozzle	Expansion ratio (ε_d)	15
	Contraction ratio (ε_c)	3.5
	Throat radius (r_t), mm	56.6
	Divergent section length (L_d), mm	247.64
	Convergent section length (L_c), mm	265.95
Cylinder	Barrel section length (L_b), mm	476.87
	Chamber radius (r_c), mm	105.97
Rib	Base (b), mm	1.27
	Height (h), mm	1.00
	Pitch (p), mm	1.04
	Number (N_{ribs})	288

Table 7.3: Thrust chamber and nozzle data [10] and ribs geometrical features[109, 111].

The reference geometry for the axial rectangular ribs is inspired to that presented in [109, 111], whereas the operative conditions and the nozzle geometry are taken from [10].

The hot gas side numerical grid and boundary conditions adopted hereafter are shown in Fig. 7.10. The details of the numerical grid and boundary conditions in the vicinity of the walls for a cross section at chamber inlet and an axial section of the chamber at the axial position where the ribbed chamber ends are shown in the enlargements of Fig. 7.10.

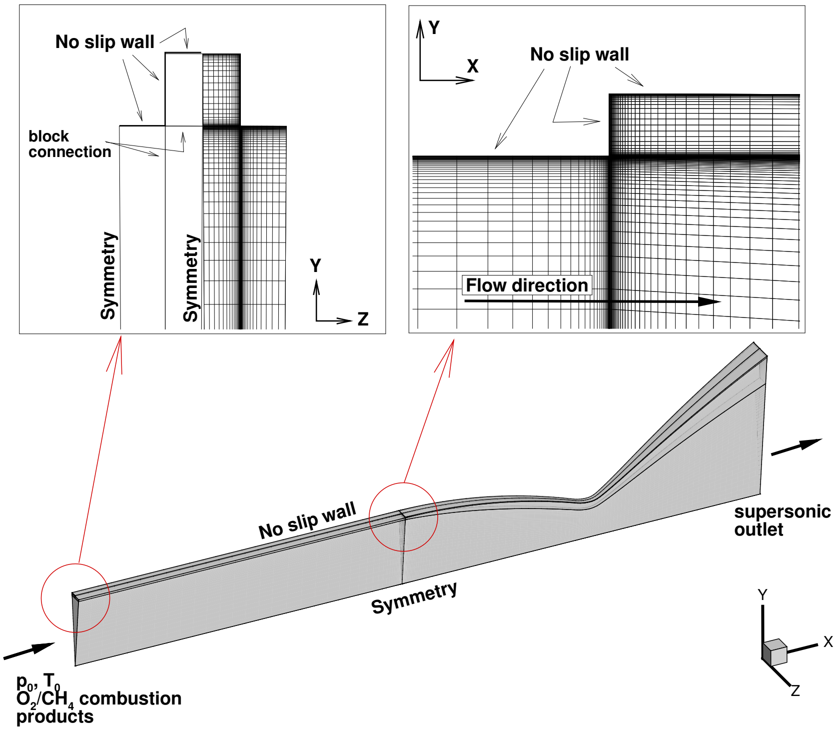

Figure 7.10: Numerical grid and boundary conditions for the hot gas side numerical simulation of the ribbed thrust chamber.

The numerical grid is a three dimensional multi-block grid composed by 576000 volumes divided into 9 blocks whose cells are clustered toward the walls to solve properly the kinematic and the thermal boundary layer. The numerical domain of interest is defined between half rib and half empty space between two ribs, taking advantage of symmetry. At the subsonic inflow, stagnation pressure and stagnation temperature are prescribed together with the mixture composition and the inlet velocity direction. The adiabatic flame temperature enforced as the inlet stagnation temperature and the mixture composition are the result of the chemical equilibrium calculation, obtained for the assigned values of chamber pressure and oxygen/methane mixture ratio. The injected mixture is composed by the main 9 species, whose mass fractions are summarized in Tab. 7.4. Composition is assumed as frozen once injected in the chamber. Crosswise wall temperature effects are investigated enforcing both isothermal and variable temperature at each section of the ribbed region as discussed in Sec. 7.3.2. Supersonic outflow is set at the right boundaries and symmetry is set at the lower boundaries.

7.3.2 Wall temperature crosswise effect

In this section, the effect of enforcing a constant wall temperature rather than enforcing a variable temperature in the crosswise direction is investigated focusing on the

Species	Mass fraction
CO	0.2300
CO_2	0.2482
H	0.0013
HO_2	0.0002
H_2	0.0075
H_2O	0.3864
O	0.0113
OH	0.0651
O_2	0.0500

Table 7.4: Chemical equilibrium mixture composition in terms mass fractions at the operative load point.

wall heat flux. The evaluation of the influence of a simplified boundary condition is the basis of the approach adopted in the next section for the parametric analysis on the rib height. This effect is studied comparing two numerical simulations of the same ribbed thrust chamber with different thermal wall boundary conditions (see Fig. 7.11): in the first the wall temperature is enforced as a constant value along the crosswise direction (i.e. pitch, base and height of the rib have the same wall temperature T_w=700 K), whereas in the second, the wall temperature in the ribbed region is evaluated by a loose coupling analysis taking into account the heat conduction through the solid wall enforcing a constant back temperature ($T_{w,\ back}$=680 K).

The coupling procedure relies on the same simplified approach described in Ch. 6. In this latter case, the wall temperature to enforce as a boundary condition to the numerical simulation is the result of the balance between the heat transfer from the hot gas through the wall. In particular, the wall back temperature is assumed to be constant along the chamber and in the crosswise direction. Moreover, the heat conduction inside the solid material in the streamwise direction is neglected assuming that it is lower than the heat conduction in the radial direction. Then for each cross section in the ribbed region, the wall boundary condition is coupled to a two dimensional cross section of the solid material. The wall is assumed as made of an oxygen free high conductivity (OFHC) copper alloy whose thermal conductivity is 390 W/(m K). The solid material thickness is equal to the height of the rib and is chosen according to the analysis performed in [111]. The heat conduction inside the solid wall is solved by means of a three dimensional solver of the Fourier equation whose features are described in [115]. The boundary conditions and the numerical grid for the ribbed section where the solid material is solved is shown in Fig. 7.12(a). For the solid wall solution, the wall back temperature is fixed at $T_{w,\ back}$=680 K; at the hot gas side wall boundary the heat transfer coefficient, evaluated by means of Eq. 6.2 from the hot gas numerical simulation, is enforced and symmetry is prescribed at both right and left boundaries. The hot gas side wall temperature evaluated by the Fourier equation solver is then enforced to the hot gas side CFD numerical simulation.

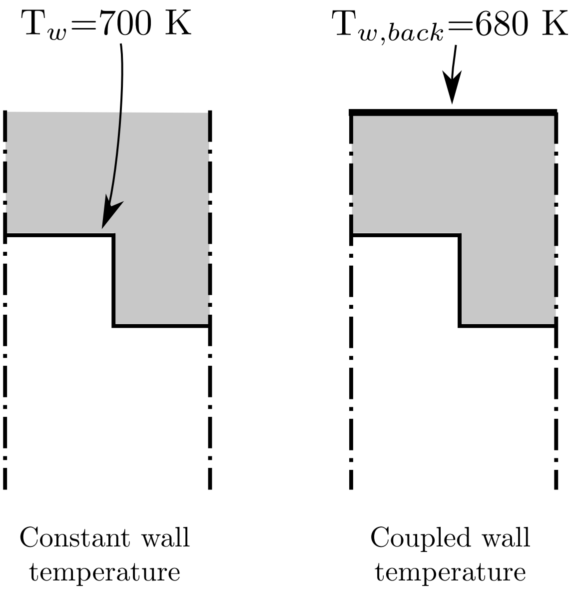

Figure 7.11: Thermal wall boundary conditions for the crosswise effect investigation.

The temperature field obtained with the coupled approach for a cross section of the ribbed region is shown in Fig. 7.12(b), where the temperature contour lines inside the solid material are plotted with dashed lines.

The heat flux evaluated from the hot gas side to the solid material is shown in Fig. 7.13 for the two approaches. In particular, the back temperature enforced in the coupled simulation is chosen to ensure the same wall temperature in the empty space between two ribs for both the approaches. Wall heat flux decreases from the pitch to the corner, then a discontinuity establishes between the corner and the edge increasing the wall heat flux from zero to a very high value related to the sharp edge of the rib. Then wall heat flux decreases toward an asymptotic value along the tip.

The small thickness of the solid material and the small height of the rib induce a difference between the tip and the pitch wall temperature of approximately 50 K in the coupled problem. Due to the strong temperature gradient between the core hot gas flow and the wall, the difference in temperature along the wall between the two approaches does not give an appreciable difference in the wall heat flux. This result allows the next parametric analysis over the rib height influence to be performed with the simpler boundary condition keeping the wall temperature constant in the crosswise direction.

7.3.3 Rib geometry effect

In this section, the influence of the rib height on ribbed wall heat transfer efficiency is investigated by means of a parametric analysis. The numerical grid and boundary conditions enforced are again those shown in Fig. 7.10: the wall temperature in the crosswise direction is fixed to a constant value as a result of the sensitivity analysis

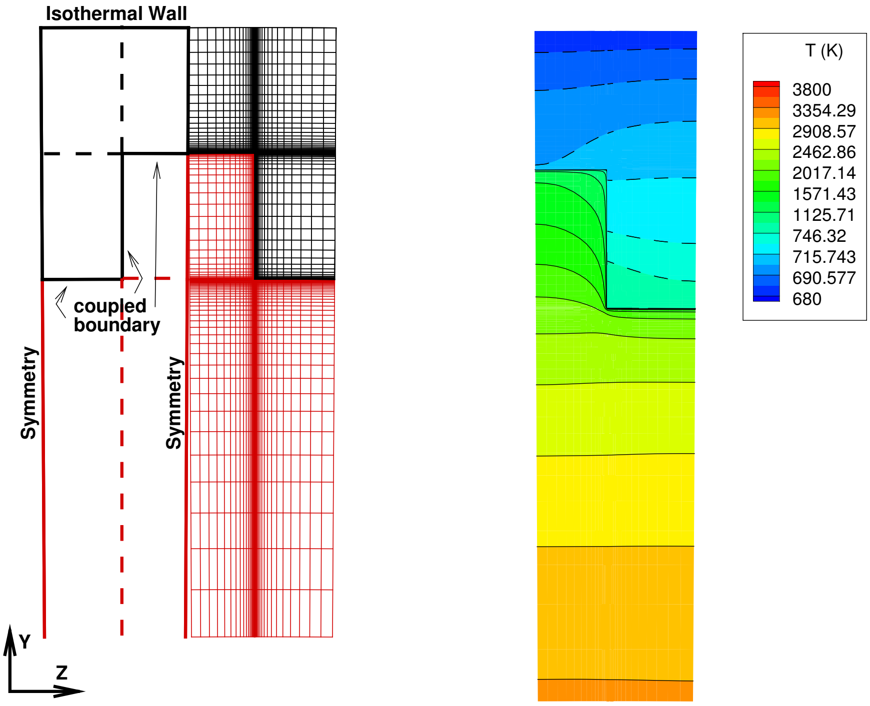

(a) Cross section numerical grid and boundary conditions.

(b) Temperature field: solid material in dashed lines, hot gas side flowfield in solid lines

Figure 7.12: Coupled approach description in a section of the ribbed region.

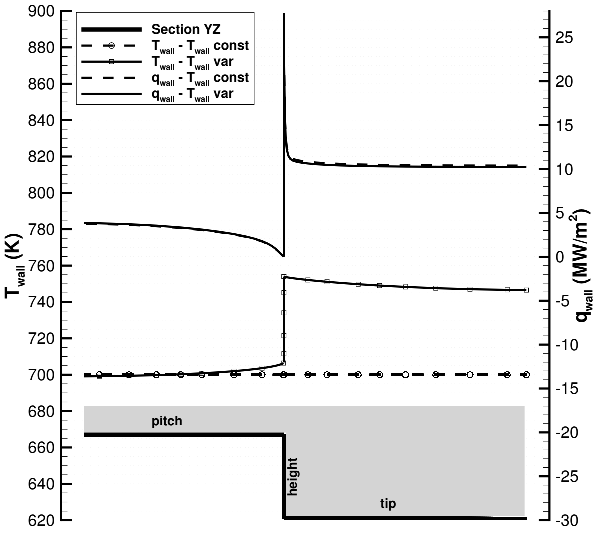

Figure 7.13: Wall heat flux for a section in the ribbed region evaluated with a constant wall temperature (dashed lines) and with the coupled approach with variable wall temperature in the crosswise direction (solid lines).

Test case	Rib height (mm)	Rib base (mm)	Rib pitch (mm)	Surface increment
1	1.00	1.27	1.04	86.51%
2	0.78	1.27	1.04	67.42%
3	0.56	1.27	1.04	48.34%

Table 7.5: Ribs parametric analysis test matrix.

Rib height	Surface increase	Rib efficiency
1.00 mm	86.51%	16.43 %
0.78 mm	67.42%	18.55 %
0.56 mm	48.34%	18.66 %

Table 7.6: Parametric analysis: rib efficiency with different rib heights.

performed in Sec. 7.3.2. Three different rib heights are investigated whose geometrical features are summarized in Tab. 7.5. As a reference test case to evaluate the heat transfer enhancement and the ribs efficiency, a smooth wall thrust chamber is also studied. Wall heat flux numerical results are shown in Fig. 7.14 for the three rib heights compared to the smooth test case, whose maximum value at the throat is adopted to reduce the wall heat flux numerical results (i.e. $\Omega = q_{wall}/q_{wall,\ max\ (smooth)}$). The heat flux in the ribbed region for all the ribbed test cases is higher than the smooth case but strongly reduces along the cylindrical section due to the growth of the boundary layer and the thermal stratification inside the empty space between ribs.

In the section where the ribbed region ends, wall heat flux shows a discontinuity related to the sharp edges of the rib end and the consequent wake which establishes downstream. Due to the small rib height, compared to the thrust chamber radius, the wake region downstream of the rib end is small. Nevertheless, its effect on wall heat flux in the convergent section is not negligible having affected the boundary layer structure. As a consequence, the wall heat flux peak at the throat is lower than the smooth test case in the present configuration because of a thicker boundary layer induced by the wake flow downstream of the rib end.

In Tab. 7.6 rib efficiencies evaluated in the three test cases are summarized compared to the surface increase: in particular the higher the rib, the larger the surface increment but the lower the rib efficiency.

The heat transfer enhancement is ineffective when the surface increase is not followed by a consequent increase of heat flux. This phenomenon can be observed comparing the heat transfer values for h =0.78 mm and h =1.00 mm: increasing the surface compared to the smooth case from 67.42% to 86.51% does not provide a noticeable effect on the heat flux in the ribbed region.

This can be explained focusing on the temperature field which establishes in the empty space between ribs and the wall heat flux contribution of each of the surfaces in a cross section of the ribbed region. In particular, Figs. 7.15 and 7.16 are referred

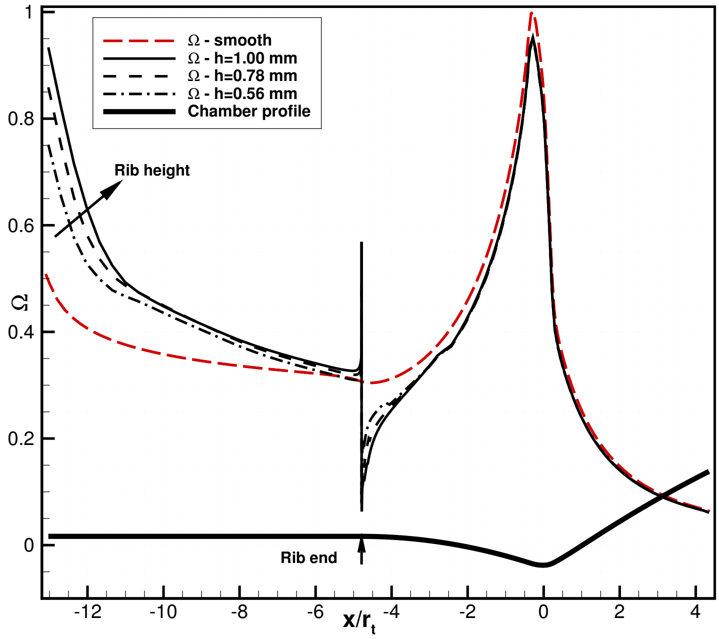

Figure 7.14: Heat transfer enhancement due to wall ribs: wall heat flux along the thrust chamber with three different wall rib heights.

Test case	1	2	3
rib height (mm)	1.00	0.78	0.56
$\bar{T}$ (K)	1566.57	1633.32	1698.09
$\bar{T} - T_{wall}$	866.57	933.32	998.09

Table 7.7: Bulk temperature between two ribs and bulk temperature gradient.

to the axial section $x/r_t = -5$ just upstream of the rib end where the inlet approach influence related to the boundary layer growth vanishes. Comparing the temperature fields in Fig. 7.15, the higher the rib the stronger the thermal stratification between ribs which cools down the flow lowering the average temperature and reducing the heat flux contribution of the pitch and the height of the ribs.

In Tab. 7.7 the average temperature between ribs ($\bar{T}$) is summarized for the three geometries together with the bulk temperature difference between the average temperature and the wall: these values quantify the obvious consideration that the flow in between two ribs gets colder as the height of the rib increases. Moreover, the contribution of the heat flux in the crosswise direction along the walls shown in Fig. 7.16 highlights that the tip of the ribs absorbs nearly the same heat from the hot gas side for the three test cases, whereas the heat flux at the pitch clearly shows a decreasing asymptotic value as the height of the rib increases.

As a consequence, the integral heat transfer enhancement shows a decreasing efficiency as the rib height increases as long as a further surface increase does not provide a further overall heat flux increase.

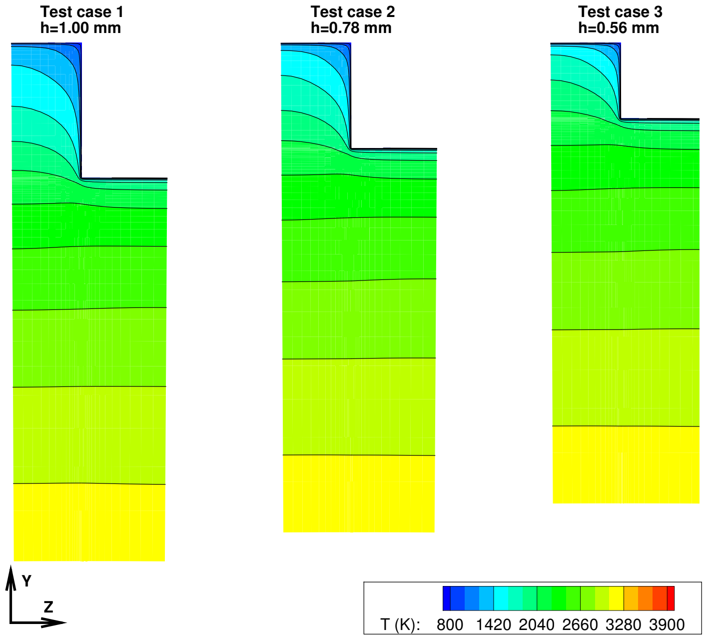

Figure 7.15: Temperature field for the three test cases: focus on the near wall region, x/r_t=-5.

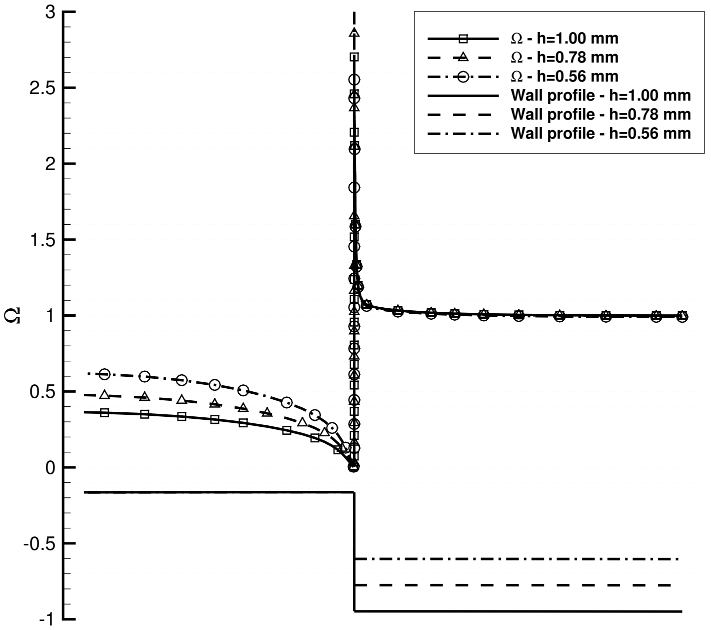

Figure 7.16: Wall heat flux for the three test cases, cross section in x/r_t=-5.

8

Expander cycle engine thrust chamber

Recently, studies on existing oxygen/hydrogen expander cycle engines modified by replacement of hydrogen with methane have been performed by industries [9, 116] and universities [10], in order to better understand feasibility and limits of envisaged oxygen/methane expander cycle engines. This design approach aims to reduce the development costs of a new engine taking advantage of previous know how on hydrogen/oxygen engines, then only few components have to be newly designed to treat a different fuel. In particular, in the LYRA program, an oxygen/hydrogen expander cycle engine is being modified to operate with oxygen/methane. In this last chapter, the thermal analysis of the LM-10 MIRA engine is performed applying the simplified approaches described and validated in Chs. 5, 6 and 7 for the injection simplification, the coupled analysis with the regenerative cooling and the ribber thrust chamber configuration, respectively.

The present analysis is divided into two parts. First the hot gas side heat transfer process is analyzed assuming no coupled interaction with the cooling jacket flow. This preliminary uncoupled analysis aims to compare hot gas side heat flux numerical evaluation with different inlet approaches and barrel section wall geometries, i.e. smooth wall or ribbed wall. Then, the same configurations are investigated with a coupled procedure taking into account also wall and coolant flow heat transfer.

8.1 Test case description

The expander cycle engine of interest is the LM10-MIRA full scale demonstrator based on the existing KBKhA oxygen/hydrogen expander cycle engine prototype modified to operate with liquid methane in the frame of the LYRA program, supported by ASI as the future evolution of the VEGA launcher. The injector head and the fuel turbopump assembly have been newly designed and optimized by AVIO[5, 117] due to the higher density of methane with respect to hydrogen. This approach strongly reduces design and development costs but requires detailed analysis to evaluate the impact of operating the engine with another fuel.

The engine nominal design point is summarized in Tab. 8.1 and the thrust chamber assembly schematic is shown in Fig. 8.1. The thrust chamber was designed to optimize the heat transfer from the hot-gas side to the coolant, that was hydrogen in the original prototype. Then, the large heat transfer required by the hydrogen to drive the turbopump was obtained by means of surface increase obtained increasing the cylinder length and adding axial wall ribs with rectangular cross section, as shown in Fig. 8.2.

The surface increment obtained by means of axial ribs in the cylindrical section of the thrust chamber is $\tilde{4}0\%$ and the rib rectangular cross section is characterized by a low height to tip ratio. Supercritical methane flows inside the cooling circuit counter-wise the main flow inside the channels from the divergent section up to the injector plate (Fig. 8.1). The thrust chamber is divided into four sections characterized by different materials and cooling channels number.

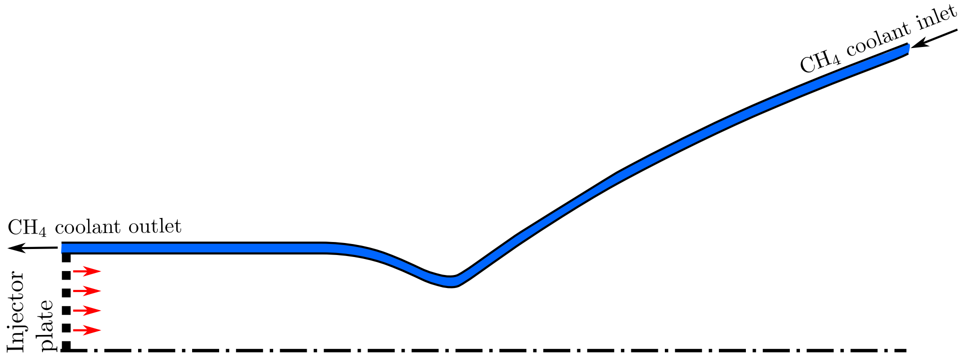

Figure 8.1: LM10-MIRA full scale demonstrator: thrust chamber assembly schematic.

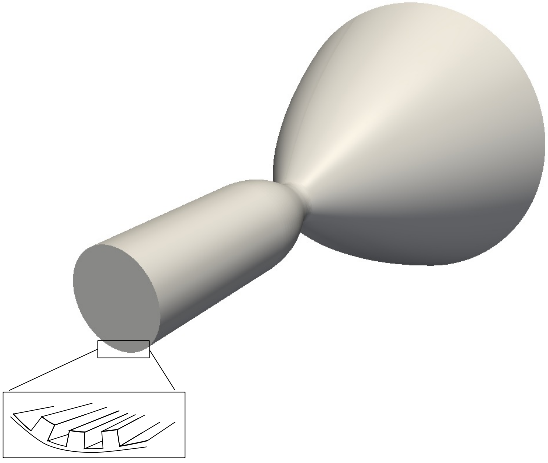

Figure 8.2: Axial ribs arrangement.

Chamber pressure	60 bar
Mixture ratio (OF)	3.4
Ribs surface increase	40 %

Table 8.1: LM10-MIRA full scale demonstrator [117, 20, 118]: thrust chamber assembly data.

8.2 Hot gas side heat transfer modeling

In this section, an uncoupled analysis of the hot gas side heat transfer process is performed comparing two different approaches for the inlet description and the effects of heat transfer enhancement devices in the barrel section. The two approaches follow those described in Sec. 5.1: the full inlet and the pseudo-injector approaches. The

Species	Mass fraction
CO	0.236
CO_2	0.253
H	0.001
H_2	0.008
H_2O	0.400
O	0.008
OH	0.056
O_2	0.037

Table 8.2: Chemical equilibrium mixture composition at nominal condition Tab. 8.1

full scale thrust chamber is analyzed, therefore reducing the complex injector plate arrangement according to the simplified model described in Sec. 5.1.

According to the discussion made on the rib parametric analysis in Chapter 7, heat transfer enhancement due to axial wall ribs is evaluated by means of the rib efficiency. Due to wall ribs axial arrangement, their effect is analyzed by means of a three dimensional numerical simulation which adopts the full inlet approach.

8.2.1 Inlet approach effect

The simplified inlet approaches defined in Sec. 5.1 are adopted to study the heat loads coming from the hot gas side for the full scale engine of interest. Axis-symmetric numerical grid and boundary condition enforced for full inlet and pseudo injector approach are shown in Figs. 8.3(a) and 8.3(b), respectively. Full inlet approach simulations are made over a single block grid, whose volumes are clustered toward the wall to solve properly the turbulent boundary layer. In case of simulations with the pseudo-injector approach a multi-block grid composed by three adjacent blocks is considered. In the first block, cells are clustered toward the walls to solve the turbulent boundary layer. Moreover, cells are also clustered in the field to solve the two wake regions which establish: one in the backward facing step configuration near the inlet section toward the wall and the other in the base flow near the axis of symmetry. The second block is relevant to the cylindrical section of the chamber and the third block is relevant to the supersonic nozzle. Cells of both second and third blocks are clustered toward the upper wall to solve the turbulent boundary layer.

In the inlet boundary, the actual injector plate arrangement is simplified as shown in Fig. 8.4: equilibrium combustion products at the nominal conditions summarized in Tab. 8.1 are injected in the chamber at their adiabatic flame temperature (T_{ad}=3550.18 K) and it is considered as frozen inside the thrust chamber. Mixture composition is listed in Tab. 8.2 in terms of mass fractions of the main 9 species evaluated under the assumption of chemical equilibrium.

In the full inlet approach, stagnation pressure is also enforced and the inlet section is the whole section of the chamber. In the pseudo injector approach the mass flow rate

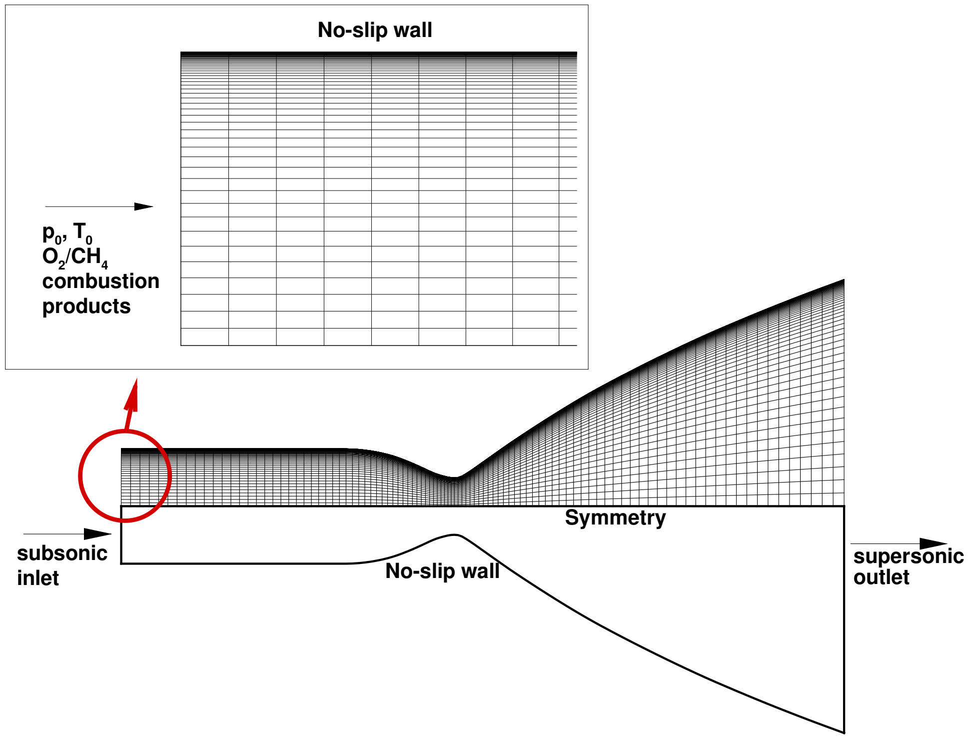

(a) Full inlet approach

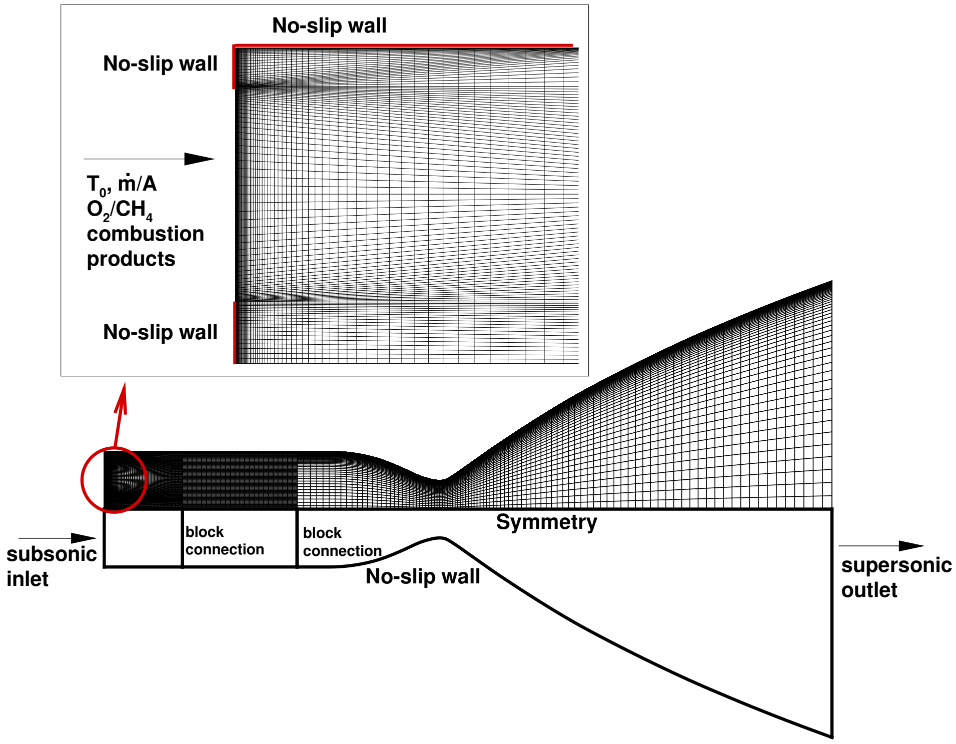

(b) Pseudo injector approach

Figure 8.3: LM10-MIRA full scale demonstrator: numerical grid and boundary conditions enforced.

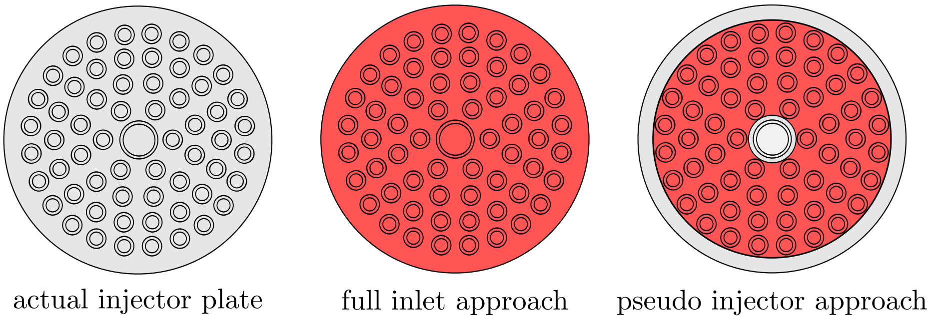

Figure 8.4: LM10-MIRA full scale demonstrator injector plate arrangement and simplified inlet approaches: full inlet and pseudo injector approach.

Grid	N. of volumes	Δy min (μm)
Coarse	50×40	3.80
Medium	100×80	1.90
Fine	200×160	0.95

Table 8.3: Full inlet approach grid convergence analysis.

Grid	N. of volumes			Δy min (μm)
	block 1	block 2	block 3	
Coarse	35×55	12×44	50×40	3.80
Medium	70×110	24×88	100×80	1.90
Fine	140×220	48×176	200×160	0.95

Table 8.4: Pseudo-injector approach grid convergence analysis.

per unit area is enforced at the annular section within the inner and the outer injectors ring. The inlet sections for both approaches are highlighted in red in Fig. 8.4. In a full scale engine, the pseudo injector approximation allows to preserve both the distance between the outer injector ring and the chamber wall and the distance between the inner injector ring and the axis of symmetry.

In both the approaches, the outlet boundary is set as supersonic, then no boundary conditions have to be prescribed. The walls are treated as isothermal walls with a constant wall temperature along the chamber (700 K).

Grid convergence analysis has been performed for both grid topologies with three different grid levels as summarized in Tabs. 8.3 and 8.4.

Axial velocity component profiles evaluated by means of the three grids with full inlet and pseudo injector approach are plotted in Figs. 8.5(a) and 8.5(b), respectively. Richardson extrapolated solution (Eq. 4.2) is taken as a reference to evaluate the numerical error included in the plots relevant to the medium numerical solution. Full inlet approach is characterized by a lower numerical error with respect to the pseudo

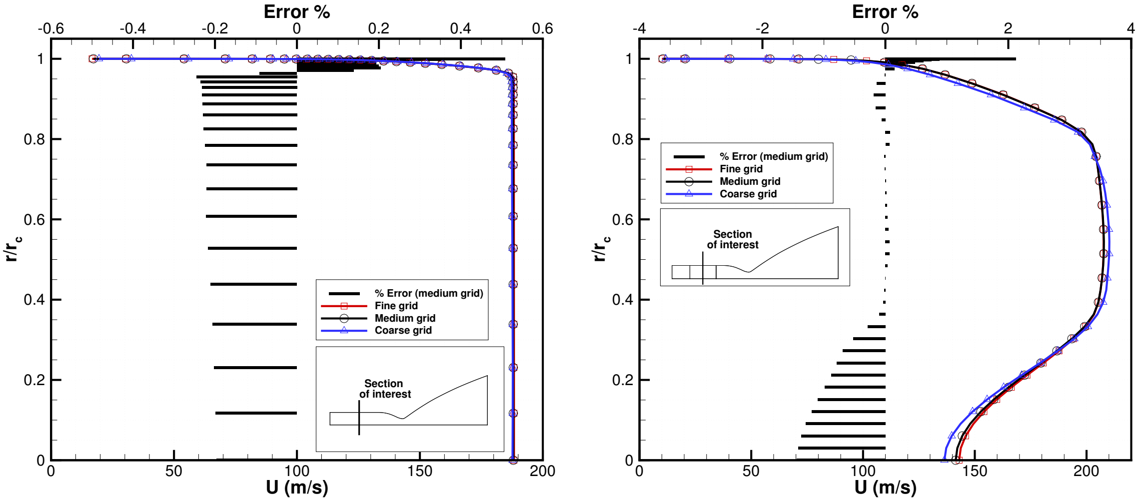

(a) Full inlet approach

(b) Pseudo injector approach

Figure 8.5: LM10-MIRA full scale demonstrator grid convergence analysis: axial velocity component at section x/r_t=-7, upstream of the throat, obtained with three grids (solid lines) and numerical error evaluation (dashed lines) referred to Richardson extrapolated solution.

injector approach. This can be ascribed to the need of higher grid resolution to solve the wake flow which establishes near the axis and in the backward facing step configuration near the wall. Comparing the axial velocity profiles, the full inlet approach shows a typical wall boundary layer profile, whereas the pseudo injector profile is influenced by the presence of the wake and the backward facing step flow even downstream of the end of the recirculating region. Nevertheless, the integral velocity value inside the chamber is the same for both the approaches, because the central region of the pseudo injector profile is characterized by a higher axial velocity component which compensate the lower velocity of the region affected by the recirculating flow.

Temperature fields in the thrust chamber obtained with the two approaches are shown in Fig. 8.6, together with an enlargement of the inlet section of the pseudo-injector approach where streamlines show the wake regions which establish near the axis of symmetry and the chamber wall.

Wall heat flux along the chamber obtained with both inlet approaches is shown in Fig. 8.7. Non dimensional values are plotted referring the chamber axial distance to the throat radius and the wall heat flux to the peak value obtained with the full inlet approach, i.e. $\Omega = q_{wall}/q_{wall,\ max\ (full\ inlet)}$.

In the cylindrical section, wall heat flux evaluated with the full inlet approach is monotonically decreasing in the cylindrical section toward the throat due to the growth of the boundary layer. The wall heat flux along the chamber obtained with the pseudo-injector approach increases in the region near the inlet section showing a peak and a minimum related to the recirculation region which establishes in the backward facing step configuration as described in Sec. 5.1. Then, the wall heat flux maintains

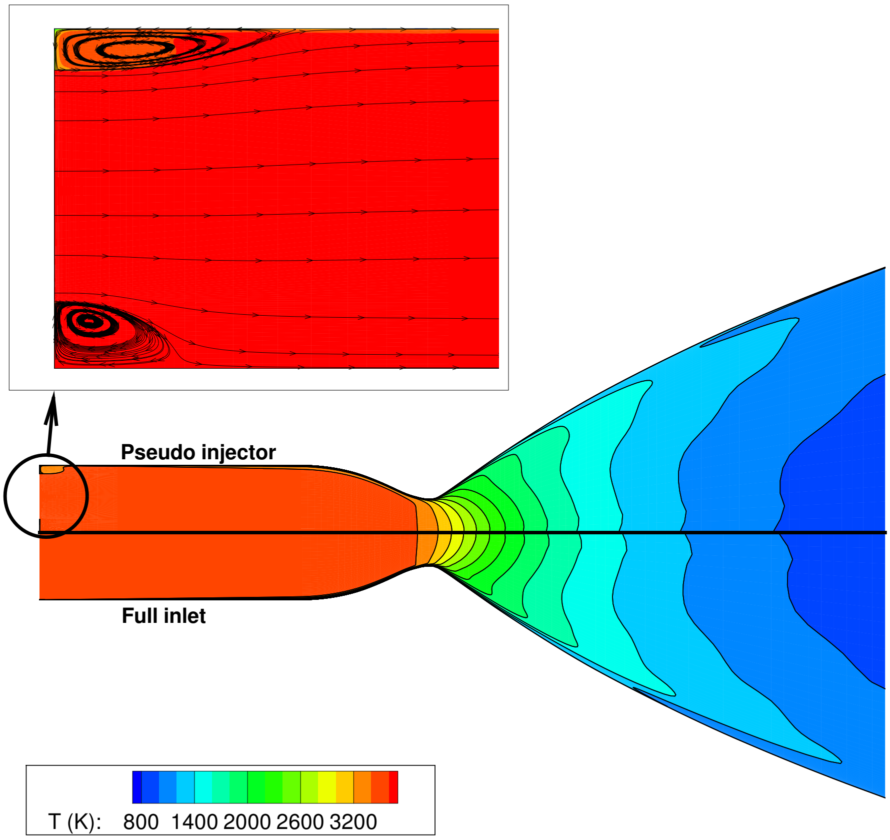

Figure 8.6: Temperature field with full inlet (bottom) and pseudo-injector (top) approach with enlargement of pseudo-injector inlet section with velocity streamlines.

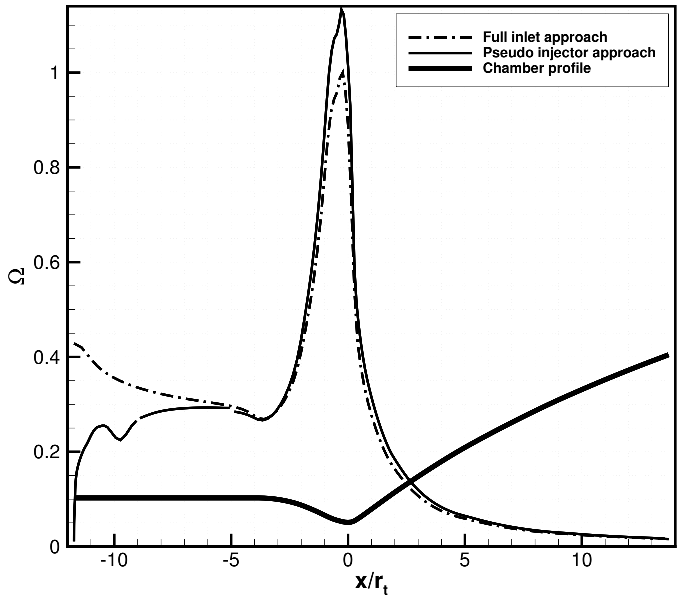

Figure 8.7: Wall heat flux along the chamber: full inlet and pseudo injector approach. Axial distance is referred to the throat radius, wall heat flux is referred to the peak value obtained with the full inlet approach.

a constant value downstream of the flow reattachment point in the cylindrical section up to the convergent section.

In the nozzle, both numerical approach solutions show the characteristic heat flux peak related to the minimum radius of the duct and consequently the smaller thickness of the boundary layer. Downstream of the throat, in the diverging section the boundary layer thickness grows and the wall heat flux decreases.

For a given wall temperature, full inlet provides a higher wall heat flux value in the barrel section and a lower heat flux peak in the throat compared to the pseudo-injector approach. This trend can be ascribed to the different boundary layer growth process in the two inlet approaches. In particular, the pseudo injector approach numerical solution provides a thinner boundary layer in the throat region compared to the full inlet approach, in the present test case. Then, for given wall and main stream temperatures, a thinner boundary layer induces a steeper temperature gradient across the boundary layer and then a higher heat flux in the throat.

8.2.2 Wall ribs heat transfer enhancement

As described in Sec. 8.1, the barrel section of the thrust chamber cross section is equipped with axial wall ribs with rectangular cross section. In this section, the rib efficiency of the present configuration is evaluated by means of a three dimensional numerical simulation relying on the simplified assumption discussed in Ch. 7. The numerical domain is a slice of the thrust chamber including half rib and half of the empty space between two ribs, as shown in Fig. 8.8. The multi-block grid volumes composing the numerical grid are summarized in Tab. 8.5 and numerical grid features and boundary conditions enforced are shown in Fig. 8.9.

In particular, the crosswise section enlarged in Fig. 8.9 top left frame shows that volumes are clustered toward the pitch, height and tip of the rib. Moreover, focusing on the axial section enlarged in Fig. 8.9 top right frame, volumes are clustered to solve for the wake region which establishes at the end of the ribbed section.

Walls are treated as isothermal walls with a constant temperature along the chamber both in axial and crosswise direction. The inlet subsonic boundary condition is the same as the full inlet approach described in Sec. 8.2.1 and the outlet boundary condition is set as supersonic.

To discuss results obtained with the present simulation it is interesting to analyze first the crosswise temperature fields. To this aim, temperature field in the ribbed section is shown in Fig. 8.10 together with the evolution of the temperature field downstream of the rib end. The first section shows the strong thermal stratification between two ribs related to the rib efficiency. Due to the small dimension of the rib height with respect to the chamber radius, the thermal stratification which establishes between two ribs disappears in few rib heights downstream of the barrel section.

Axial velocity component profiles in the ribbed region and downstream of the rib end are plotted in Fig. 8.11 at two different azimuthal sections: at the central plane of a rib and at the central plane in the empty space between two adjacent ribs. Axial velocity profiles obtained in the smooth barrel section simulation are also shown, as a reference. In line with the thermal field trend, axial velocity profiles related to the ribbed plane rapidly recover to the axial velocity profile of the plane between two ribs downstream of the ribbed section end. Focusing on the near wall region, the axial velocity profile far from the rib end (20 x/h) is different from the one obtained in the smooth test case because of the boundary layer separation and reattachment downstream of the wake region. On the contrary, far from the wall, both the smooth and the ribbed wall test case are characterized by the same axial velocity value, meaning that the rib effect is confined inside the boundary layer and does not affect the free stream field.

After having analyzed the thermal field and the axial velocity profiles, the heat flux enhancement due to axial ribs can be quantified by rib efficiency, recalling its definition given in Eq. 7.1. In Fig. 8.12, integral wall heat flux evaluated in the case of ribbed barrel section is compared to the smooth wall numerical simulation described in Sec. 8.2.1 with the full inlet approach. Wall heat flux is referred to the maximum wall heat flux evaluated in the smooth wall test case, i.e. $\Omega = q_{wall}/q_{wall,\ max\ (smooth)}$. Wall heat flux shows a strong increase in the ribbed barrel section compared to the smooth case. At the end of the ribbed section, the integral wall heat flux has a discontinuity related to the rib end: heat flux steeply increases in correspondence to the sharp corner at the end of the rib and rapidly decreases in the backward facing step configuration downstream of the rib end. Further downstream, the heat flux follows the expected trend with the characteristic peak near the nozzle throat already discussed before and then decreases in the divergent section of the nozzle. Recalling Eq. 7.1, for

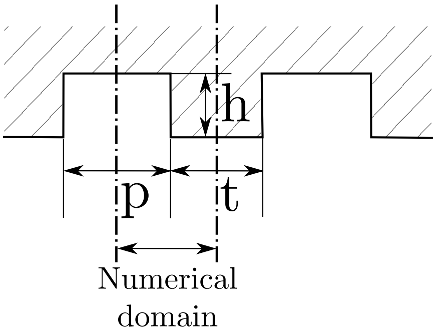

Figure 8.8: Thrust chamber with axial wall ribs: numerical domain.

Section	# block	N. of volumes
Ribbed section	1	60×50×20
	2	60×30×20
	3	60×30×20
	4	60×20×20
Nozzle section	5	120×20×20
	6	120×20×20
	7	120×30×20
	8	120×30×20
	9	120×50×20

Table 8.5: Thrust chamber with axial wall ribs: multi-block numerical grid features.

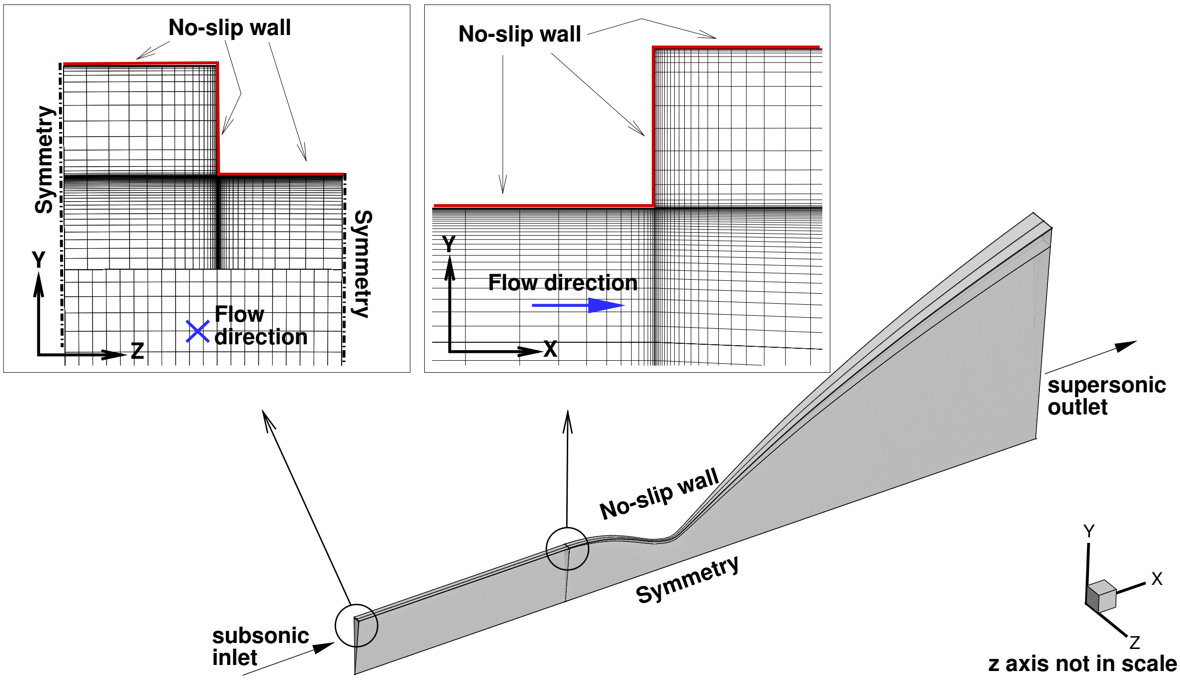

Figure 8.9: Thrust chamber with axial wall ribs: numerical grid and boundary conditions. Top left: enlargement of a crosswise section. Top right: enlargement of an axial section at the end of the ribbed wall section.

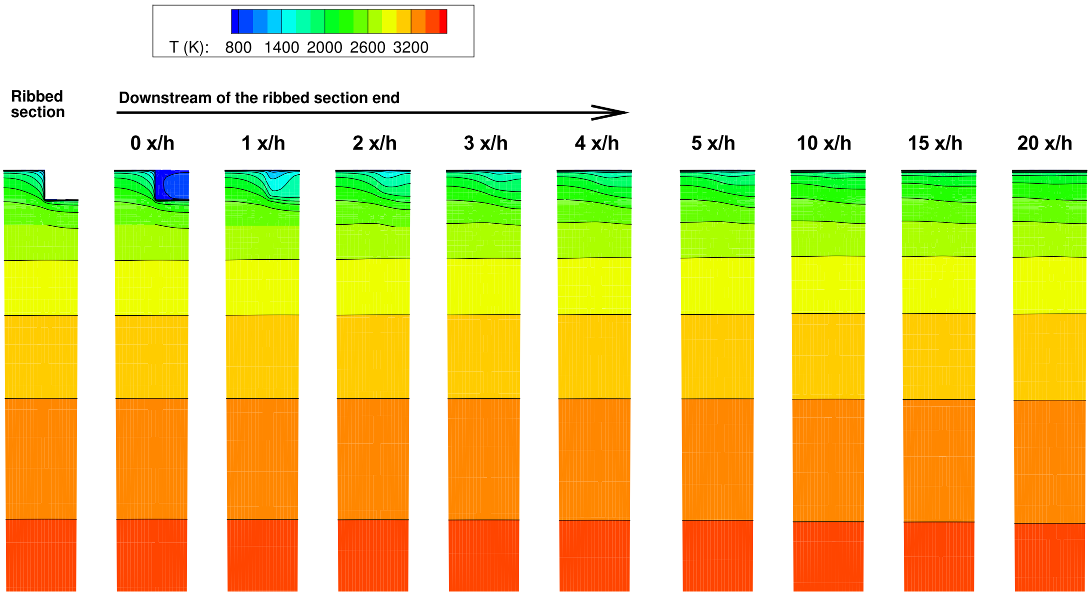

Figure 8.10: Temperature field enlargement in the ribbed region and downstream of the ribbed region end at different sections (non dimensional axial distance referred to rib height).

the present configuration rib efficiency is 54.10%.

The ribbed wall configuration provides a higher wall heat flux peak compared to the smooth barrel section. This can be ascribed to the boundary layer thickness at the throat of the nozzle: in the present test case the ribbed wall configuration is characterized by a thinner boundary layer compared to the smooth wall case. Due to the small height to tip ratio of the present configuration, ribs efficiency has a high value due to low thermal stratification effects in between two adjacent ribs. This result agrees with the conclusions of the parametric study performed in Sec. 7.3.3.

8.3 Hot gas side - wall - coolant side coupled heat transfer

After the preliminary analysis performed for a given wall temperature, inlet effects and wall ribs heat transfer enhancement are investigated by means of a coupled approach with the wall and coolant circuit. The loose coupling procedure has been described in Chapter 6 and here is applied to evaluate the effect of the different inlet approaches and of the wall ribs to the regenerative cooling system.

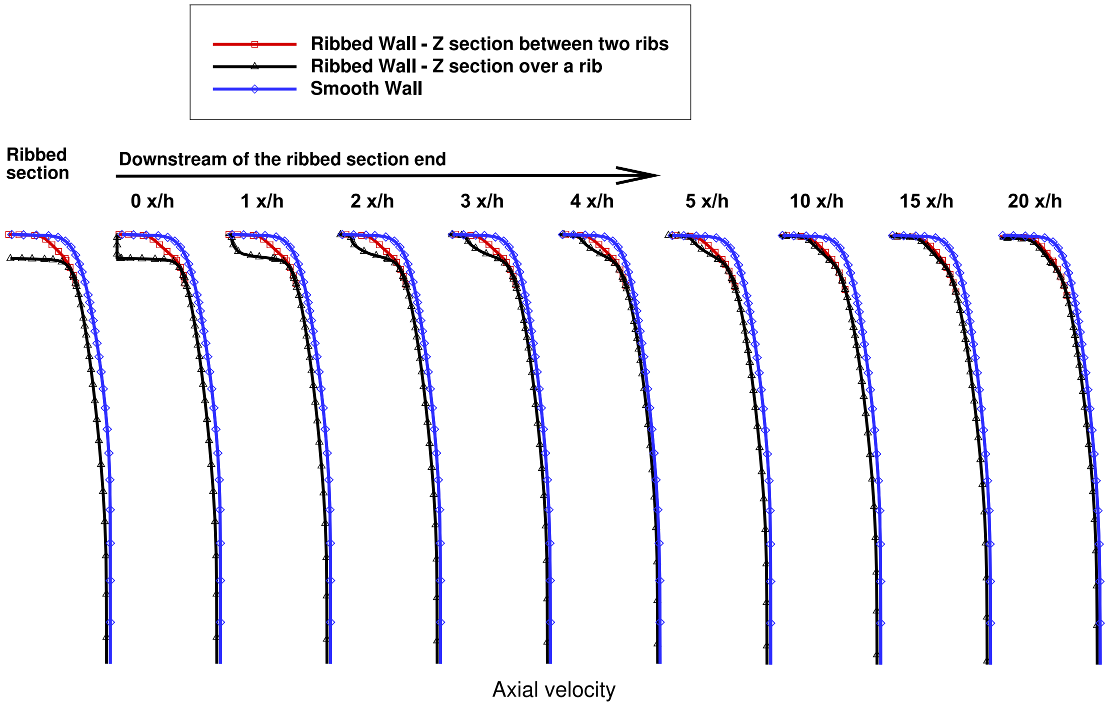

Figure 8.11: Axial velocity component profiles enlargement in the ribbed region and downstream of the ribbed region end at different sections (non dimensional axial distance referred to rib height).

8.3.1 Inlet approach effect

Inlet approach effects on the regenerative system is investigated by means of a loose coupling approach. In Figs. 8.13(a) and 8.13(b), hot gas side heat transfer coefficient evaluation in the coupling convergence process is shown for full inlet and pseudo-injector approach, respectively. Few coupling steps are sufficient to reach convergence balancing the hot gas side, the wall and the coolant side heat transfer. In Fig. 8.14(a), hot gas side heat transfer coefficient evaluated with full inlet and pseudo injector approach are compared. In this section, different wall temperature are enforced to the hot gas numerical simulations coming from the coupling procedure. Therefore, heat transfer coefficient obtained with the two approaches and evaluated by means of Eq. 4.3 is compared taking advantage of its small dependence from the wall temperature. As in the uncoupled analysis, full inlet approach shows a higher heat transfer in the cylindrical section with respect to the pseudo injector approach due to different boundary layer growth processes described in Sec. 8.2.1. In the throat section, pseudo injector approach gives a higher heat transfer coefficient peak related to a thinner boundary layer as discussed in the uncoupled analysis. To analyze the inlet approach effect in case of coupled simulation, hot gas side wall temperature and coolant temperature are shown in Fig. 8.14(b). Wall temperature profiles are affected by cooling channels

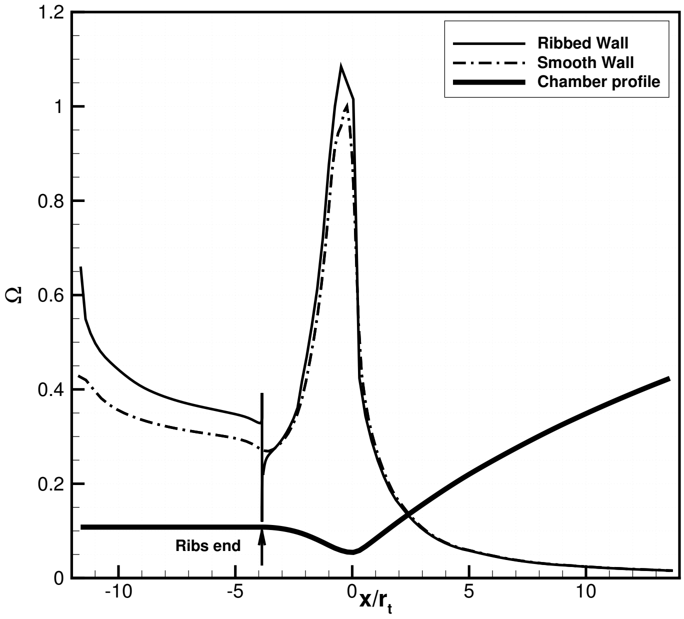

Figure 8.12: Wall heat flux along the ribbed thrust chamber: integral wall heat flux compared to smooth wall heat flux and ribs efficiency. Ω is the non dimensional value of the heat flux referred to the maximum value of the smooth test case.

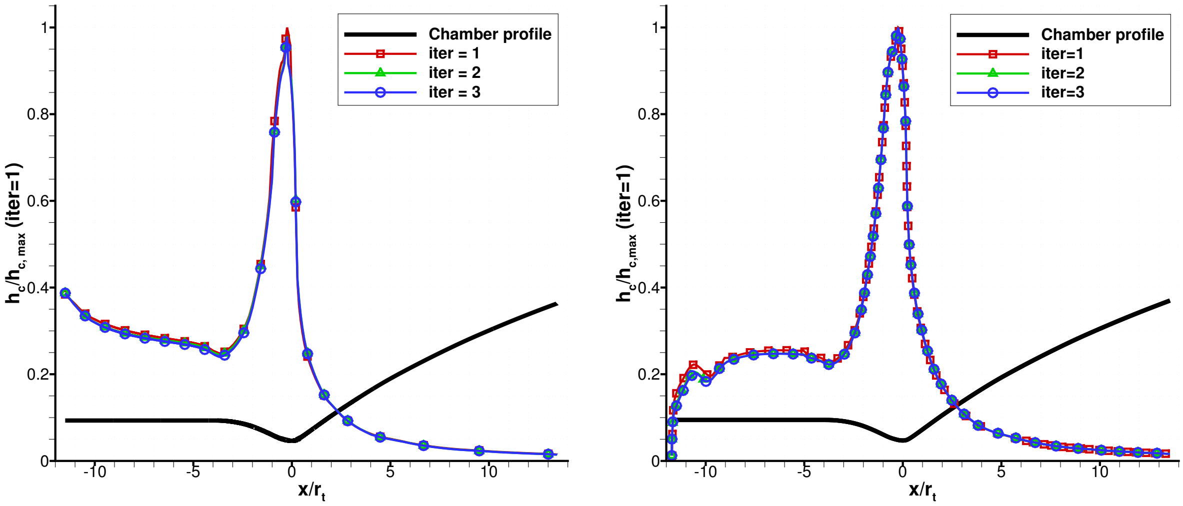

(a) Full inlet approach

(b) Pseudo injector approach

Figure 8.13: Hot gas side heat transfer coefficient: loose coupling convergence iterations. Reference value $h_c/h_{c,\ max\ (iter\ 1)}$.

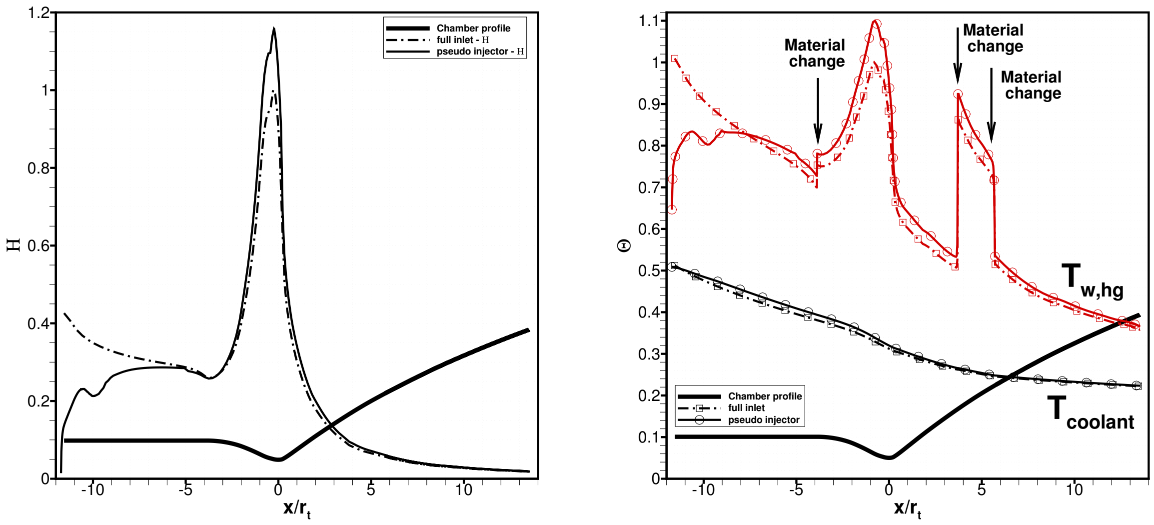

(a) Hot gas side convective heat transfer

(b) Hot gas side wall temperature and coolant temperature

Figure 8.14: Full inlet and pseudo injector approach comparison.

number variation and material variation along the chamber that are located in correspondence to the temperature discontinuity. Focusing on the wall temperature, full inlet approach maximum wall temperature is reached at the inlet section and at the throat region. The first maximum can be ascribed to the inlet approach and does not capture the physical trend near the injector plate, whereas the second maximum is associated to the maximum convective heat transfer in the throat region. On the contrary, pseudo injector approach reaches its maximum wall temperature value at the throat region, whereas shows an increasing wall temperature profile near the inlet section. Comparing numerical solutions in the throat region, pseudo injector reaches a higher hot-gas side wall temperature value than the full inlet approach. This peak value is related to the higher convective heat transfer coefficient in the throat region which can be ascribed to the thinner boundary layer which characterizes the present configuration. The coolant temperature shows slight difference between the two approaches and it is not affected by the change of material and cooling channels number.

8.3.2 Wall ribs heat transfer enhancement

In this section the coupled analysis of the heat transfer process in the ribbed thrust chamber is described. As in the uncoupled analysis, smooth wall test case is taken as a reference to evaluate the heat transfer enhancement due to axial wall ribs. Nevertheless, having different wall temperature because of the coupled analysis together with the regenerative cooling system, the comparison between the two test cases can be only qualitative and rib efficiency cannot be evaluated. In particular, here the feedback effect of the increased heat transfer coefficient on the hot-gas side wall temperature is

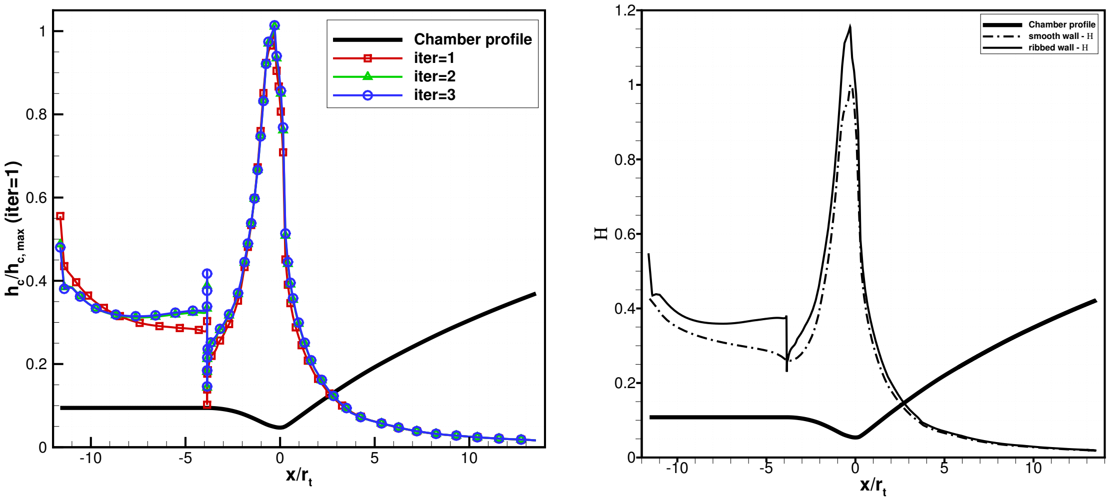

(a) Loose coupling convergence iterations (b) Smooth wall vs ribbed wall

Figure 8.15: Hot gas side heat transfer coefficient with axial wall ribs.

investigated together with the increased coolant temperature at the exit of the cooling circuit related to the heat transfer enhancement produced by wall ribs. The coupling procedure described in Sec. 6.2 requires the heat transfer coefficient along the chamber and does not take into account the actual three dimensional arrangement of the channels in the cooling jacket. Therefore, the hot gas side heat transfer coefficient for the coupling procedure is the same described in Sec. 8.2.2. As a consequence of this assumption, the wall temperature evaluated by the quasi-2D model for the wall and coolant side is enforced for each axial section of the chamber, constant in the crosswise direction. As verified in Sec. 7.3.2, enforcing a constant wall temperature in the crosswise direction rather than a temperature profile on the walls gives negligible effects on the heat transfer enhancement evaluation because of the high temperature gradient between the hot gas and the wall and the typical thickness of the cooling jacket.

As in the investigation of the inlet effects, the coupling procedure between hot gas side and wall and coolant side heat transfer converges in few iterations as shown in Fig. 8.15(a) for the ribbed wall test case. The smooth wall test case numerical solution taken as a reference is that described in Sec. 8.3.1 for the full-inlet approach. The choice of coupling the models by means of the hot gas side heat transfer coefficient ensures that the first iteration with a constant wall temperature along the chamber is able to give a good starting point and then the following iterations are needed to refine the first coupled solution. A fast convergence capability for the coupling procedure is much more important in case of three dimensional numerical simulations for the hot gas side, reducing the need of costly CFD runs to reach the converged coupled solution.

In Fig. 8.15(b), the coupled heat transfer coefficient with axial wall ribs is compared to the smooth test case. As in the uncoupled analysis, the ribbed cylindrical region shows a higher heat transfer than the smooth test case. The heat transfer co-

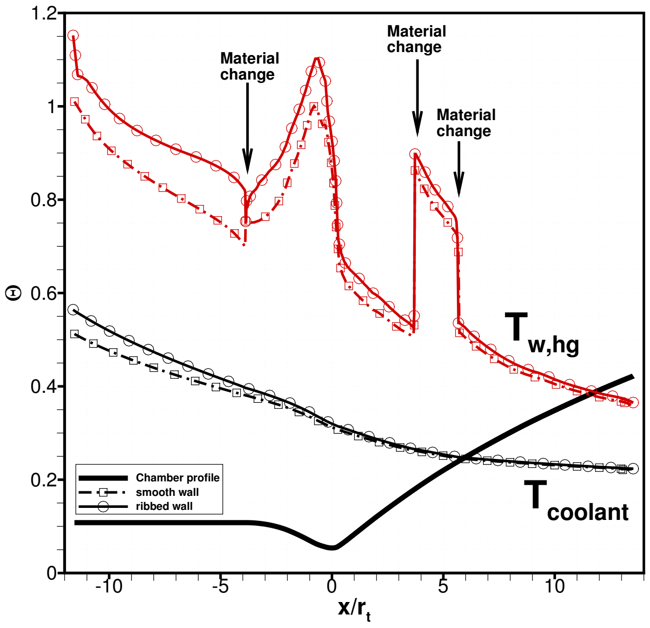

Figure 8.16: Axial wall ribs heat transfer enhancement effect: hot gas side wall temperature and coolant temperature.

efficient evaluated with the ribbed wall first decreases due to the inlet conditions and then increases in the cylindrical section up to the rib end location where a sudden discontinuity takes place due to the sharp corners of the rib end. The different trend of the coupled simulation with ribbed walls with respect to the uncoupled analysis can be justified analyzing the hot-gas side wall temperature and coolant temperature in the cylindrical section (Fig. 8.16). When the coolant exits the throat region, in the ribbed wall test case, it experiences a sudden increase of heat transfer. Then, hot-gas side wall temperature and coolant temperature increases with a consequent decrease of heat transfer from the hot gas side. This feedback mechanism between wall temperature and wall heat flux reflects on the different trend of the uncoupled and coupled analysis.

The thermal analysis described in the present chapter has been compared to classified data provided by AVIO [118]: the numerical prediction is in good agreement with the data collected in critical regions of the thrust chamber both for hot gas and coolant properties.

9

Conclusions

Simplified approaches suitable for engineering support to heat transfer analysis of liquid rocket engine thrust chambers have been discussed and validated by comparison with experimental data. In particular, the results highlight that they are a good compromise between detailed description and low computational cost for full scale engine thermal analysis.

Despite neglecting near injector plate phenomena, it has been proven that simplified injection approaches are able to provide the correct prediction of the wall heat flux all along the thrust chamber except for the injector plate closest wall, as expected due to the simplifying assumptions made. These simplified approaches have been suitably applied to the analysis of heat transfer problems such as those occurring in film cooled thrust chambers and thrust chambers with heat transfer enhancement devices.

The adoption of these approaches to investigate film cooled thrust chambers has proven that in the case of high film cooling mass flow rate injected through circumferential slots, numerical solutions are in good agreement with experimental data. In the case of low film mass flow rate injected through rectangular slots whose geometry is characterized by a high width to height ratio, the heat flux along the chamber evaluated as the weighted average of two dimensional configurations is in good agreement with experimental data and with the three dimensional configuration numerical solution. This result emphasizes that a reasonable prediction of the thermal behavior of slot film cooled thrust chambers can be obtained without resorting to time consuming three dimensional simulations.

The analysis of axial ribs as heat transfer enhancement devices of interest for expander cycle engines, has demonstrated the suitability of a simplified boundary condition to treat three dimensional wall temperature crosswise effect. In particular, due to the characteristic dimension of the rib and the flow regime inside the chamber, it has been shown that the wall temperature crosswise effect can be neglected, allowing the assumption of a crosswise isothermal wall. This approach has led to discuss the role of rib height on rib efficiency and to highlight the increasing rib inefficiency with increasing rib height due to thermal stratification between adjacent ribs, which locally lower the average temperature with consequent decrease of integral wall heat flux.

Finally, the simplified approaches have been successfully applied to the thermal analysis of the LM-10 MIRA full scale liquid rocket engine thrust chamber. This engine is being developed relying on an existing oxygen/hydrogen expander cycle engine where hydrogen is replaced with methane keeping the same thrust chamber and redesigning the injector plate and the fuel pump. Despite its complex thrust chamber profile and regenerative cooling circuit, the simplified approaches has allowed to carry out the coupled thermal analysis between the ribbed thrust chamber and the regenerative cooling circuit with a reduced computational cost. The thermal analysis performed on the LM-10 MIRA engine thrust chamber confirms that the developed approaches are able to give a prediction of the heat loads of a full scale engine with regenerative cooling and heat transfer enhancement devices.

A

Multi-block algorithm

In this appendix the multi-block algorithm is described.

Multi-block connection is realized by the solution of an approximate Riemann problem between the border volume variable values and the ghost cell facing the volume of interest. In order to preserve the second order accuracy of the code, a linear reconstruction is needed even on the border. Then a double shell of ghost cells must be employed. In case of connection, ghost cells properties must depend from the contiguous blocks solution to establish a two-way communication. As a consequence, ghost cells properties have to be interpolated from the properties of the inner cells of the contiguous domain.

The goal of the present algorithm is to identify the nearest four inner cell centers around the ghost cell center of interest to form a tetrahedron containing the ghost cell center (see Fig. A.1).

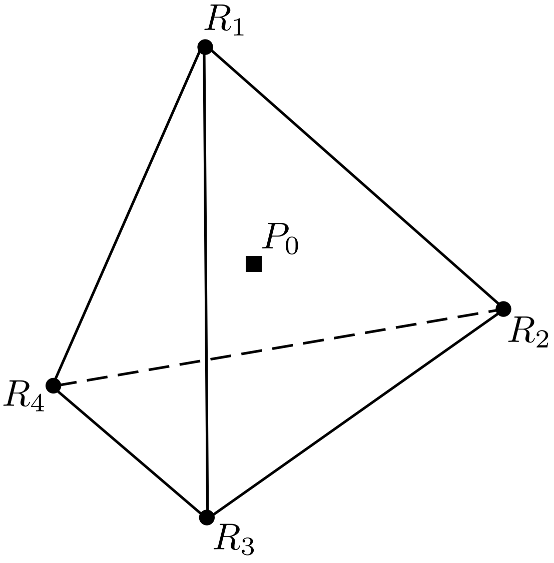

Figure A.1: Tetrahedron of *real* cell centers (R_i, $i = 1,4$) containing the ghost cell center of interest (P_0).

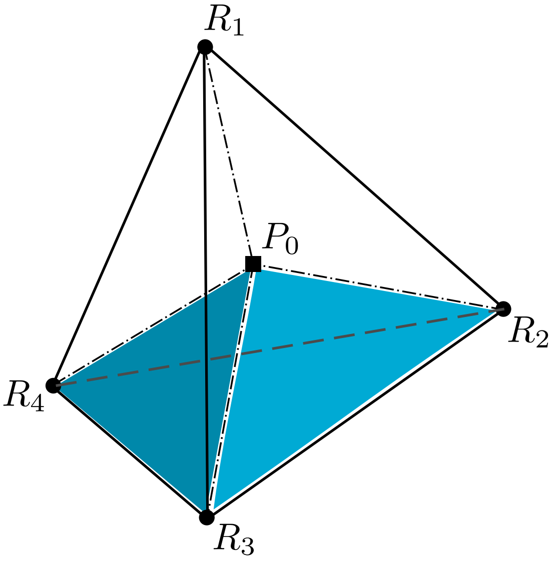

Figure A.2: Volumetric weights definition.

Given the tetrahedron, any property to be assigned at the ghost cell can be interpolated weighting the properties of the tetrahedron four vertices.

The algorithm can be divided in the following steps:

Step 1 a double shell of ghost cells is extrapolated from the *real* domain from the face where connection boundary condition is enforced;

Step 2 for each ghost cell, cell center P_0 is identified;

Step 3 for each P_0, the set of inner domain cell centers R_i (with $i = 1, N$ where N is the number of volumes for all blocks) is sorted by increasing distance from P_0;

Step 4 if the minimum distance between P_0 and all the R_i is less than a given tolerance, $P_0 \equiv R_i$ and weights are not evaluated assigning the maximum weight (1.0) to the point R_i;

Step 5 otherwise four points are searched among the nearest points in order to form a tetrahedron which contains P_0;

Step 6 once the four vertices of the tetrahedron are identified, volumetric weights are evaluated.

Sorting algorithm (step 4) and searching algorithm (step 6) are described in details in Sec. A.1 and Sec. A.2, respectively.

Volumetric weights are defined for each vertex as the ratio between the volume of the tetrahedron composed by P_0 and the other three vertices and the overall tetrahedron volume:

$$\mathcal{W}_1 = \frac{\mathcal{V}_{P_0 R_2 R_3 R_4}}{\mathcal{V}_{R_1 R_2 R_3 R_4}}, \quad \mathcal{W}_2 = \frac{\mathcal{V}_{P_0 R_1 R_3 R_4}}{\mathcal{V}_{R_1 R_2 R_3 R_4}}, \quad \mathcal{W}_3 = \frac{\mathcal{V}_{P_0 R_1 R_2 R_4}}{\mathcal{V}_{R_1 R_2 R_3 R_4}}, \quad \mathcal{W}_4 = \frac{\mathcal{V}_{P_0 R_1 R_2 R_3}}{\mathcal{V}_{R_1 R_2 R_3 R_4}}$$

As shown in Fig. A.2, the ratio between the highlighted volume and the overall volume gives the weight related to the vertex not included in the highlighted volume. Employing this definition, if the ghost cell center P_0 is close to one of the vertex of the tetrahedron R_i, the weight associated to the inner point approaches to 1.0 .

At the end of the algorithm, weights are stored in a file containing the ghost cell indices, the four vertices of the tetrahedron and their relative weights. This algorithm is implemented in a pre-processing program and does not affect the numerical code run-time.

A.1 Sorting algorithm

Multi-block features are of interest especially for three dimensional complex geometries, thus the pre-processor has to manage a large amount of *real* points and ghost points. In order to optimize the pre-processing operations, the bottle neck of the algorithm has been identified as the sorting algorithm employed in step 4. Two different sorting algorithm have been tested to evaluate the faster one to be implemented in the pre-processor: the *quicksort* algorithm and the *merge sort* algorithm [119]. Both are comparison sorts employing the divide-and-conquer paradigm. They determine the sorted order of an input array by comparing elements following three different steps: divide, conquer and combine. Given an array A of dimension n, the quicksort algorithm can be described by the following steps:

Divide rearrange the array $A[p,\cdots,r]$ into two subarrays $A[p,\cdots,q-1]$ and $A[q+1,\cdots,r]$ such that each element of $A[p,\cdots,q-1]$ is less than or equal to $A[q]$, which is, in turn, less than or equal to each element of $A[q+1,\cdots,r]$. (Partitioning procedure)

Conquer Sort the two subarrays $A[p,\cdots,q-1]$ and $A[q+1,\cdots,r]$ by recursive calls to the Divide step

Combine Because the subarrays are already sorted, no work is needed to combine them: the entire array $A[p,\cdots,r]$ is now sorted.

The merge sort algorithm can be described by the following steps:

Divide divide the unsorted array $A[p,\cdots,r]$ into two subarrays of half the size $A[p,\cdots,q]$ and $A[q+1,\cdots,r]$. If the array is of length 0 or 1, it is already sorted.

Conquer sort each subarray recursively by re-applying the merge sort

Combine merge the two sorted subarrays back into one sorted array

The key operation of the merge sort algorithm is the merging of two sorted arrays in the Combine step. To improve the sorting runtime, the algorithm takes advantage of two ideas: a small array will take fewer steps to sort than a large array and fewer steps are required to construct a sorted array from two sorted arrays than from two unsorted arrays.

The average running time for both quicksort and merge sort algorithm is $\mathcal{O}(n\ \log n)$. However, the worst-case running time for quicksort is $\mathcal{O}(n^2)$ whereas for merge sort is $\mathcal{O}(n\ \log n)$. In order to evaluate which sorting algorithm is able to sort a large array of partially ordered items, they have been tested over the pre-processing procedure of a typical three-dimensional mesh configuration. In Fig. A.3 the two sorting algorithm are compared in terms of running time against array dimension (n). As can be seen, merge sort algorithm is able to complete the task in a lower running time than the quicksort algorithm. Recalling that the array to be sorted is composed by the distance of the point of interest (P_0) from each *real* cell center of the mesh (R_i), the difference between quicksort and merge sort algorithm running time can be ascribed to the partially ordered structure of the array to be sorted. In fact, the choice of the pivoting element $A[q]$ in the Divide step of the quicksort algorithm is its weak point thus the running time can be strongly affected by the array structure. With the present partially ordered structure, quicksort algorithm gives poor performance compared to the merge sort algorithm that is not affected by the array structure. Running time has been evaluated measuring the sorting running time over a single AMD Phenom II X6 1090 T processor at 3200MHz.

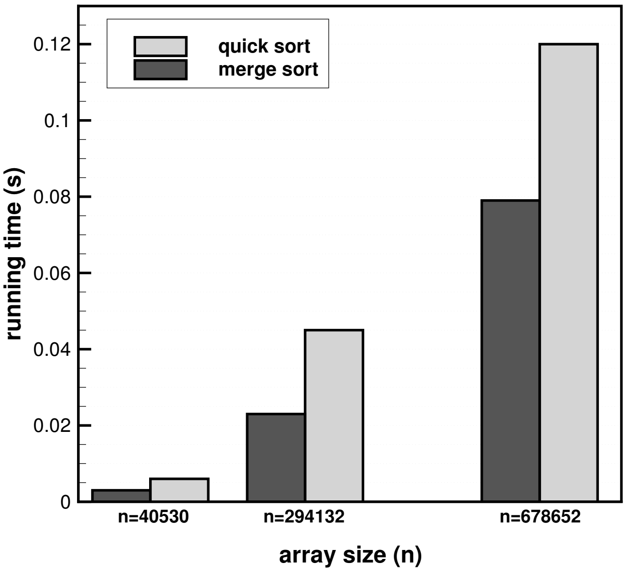

Figure A.3: Sorting algorithm performance evaluation. Running time vs sorted array dimension.

Further running time reduction is obtained by employing the sorting algorithm to rank the distance array instead of re-arranging its elements. In this way, the sorting algorithm gives as output an array containing the ranked positions of the distance array instead of the re-arranged increasing distance array.

A.2 Searching algorithm

The main section of the algorithm is the process of searching interpolation points. The best interpolation points must be physically near the ghost point to be interpolated and form a tetrahedron around the ghost point to evaluate the volumetric weights. In this frame, after the sorting process (step 3), inner points R_i sorted by distance are divided into two groups according to their position with respect to a reference plane. The reference plane is the plane containing P_0 parallel to the face of the tetrahedron where the connection boundary condition is enforced. The positive semi-space ($\mathcal{PS}$) is the one containing R_0, which is the center of the inner cell facing the ghost cell P_0, whereas the negative semi-space ($\mathcal{NS}$) is the one not containing R_0.

$$\overrightarrow{P_0R_0} \cdot \overrightarrow{P_0R_i} \begin{cases} > 0 & R_i \in \mathcal{PS} \\ < 0 & R_i \in \mathcal{NS} \end{cases}$$

The four vertices of the tetrahedron are searched between two families of points referred to in the following as *two anchored points* and *one anchored point*. Starting from three not-aligned inner points near P_0, the two anchored points research family fixes two of the three points chosen on the same semi-space and cycles over the same semi-space to find the third point. The fourth point is cycled among the nearest points belonging to the opposite semi-space to find the tetrahedron which contains P_0. The third and fourth points are cycled while their distance from P_0 is lower than a reference value defined in terms of the closer cells dimension. The algorithm for the two-point anchored research family is formalized in Eq. A.1.

$$
\begin{aligned}
& R_i^{\mathcal{S}},\quad R_j^{\mathcal{S}},\quad R_k^{\mathcal{S}},\quad R_h^{-\mathcal{S}} \\
& \begin{cases}
i \leq 3, \quad j \leq 3 \land j \neq i & \text{(anchored points index variation)} \\
k \geq 1 \land k \neq i \neq j, \quad h \geq 1 & \text{(variable points index variation)} \\
R_i, R_j, R_k \in \mathcal{S}, \quad R_h \in -\mathcal{S} & \text{(semi-space affiliation)} \\
\overrightarrow{R_iR_j} \cdot \overrightarrow{R_iR_k} \neq 1 & \text{(no-alignment)} \\
\left|\overrightarrow{P_0R_k}\right| \leq d, \quad \left|\overrightarrow{P_0R_h}\right| \leq d & \text{(closeness factor)}
\end{cases}
\end{aligned}
\tag{A.1}
$$

where $\mathcal{S}$ is the positive or negative semi-space and $-\mathcal{S}$ its opposite and d is the characteristic distance chosen as the radius of the sphere of influence around P_0 containing the closer inner points.

The one-point anchored research family fixes one of the three nearest not-aligned points on the same semi-space and cycles over the same semi-space to find the second and third point for the base of the tetrahedron. The fourth point is cycled among the nearest points belonging to the opposite semi-space to find the tetrahedron containing P_0. The second, third and fourth points are cycled while their distance from P_0 is lower than a reference value defined in terms of the closer cells dimension. The algorithm for the one-point anchored research family is formalized in Eq. A.2.

$$
\begin{aligned}
& R_i^{\mathcal{S}},\quad R_j^{\mathcal{S}},\quad R_k^{\mathcal{S}},\quad R_h^{-\mathcal{S}} \\
& \begin{cases}
i \leq 3 & \text{(anchored point index variation)} \\
(j \geq 1, \quad k \geq 1) \land k \neq j \neq i, \quad h \geq 1 & \text{(variable points index variation)} \\
R_i, R_j, R_k \in \mathcal{S}, \quad R_h \in -\mathcal{S} & \text{(semi-space affiliation)} \\
\overrightarrow{R_iR_j} \cdot \overrightarrow{R_iR_k} \neq 1 & \text{(no-alignment)} \\
\left|\overrightarrow{P_0R_j}\right| \leq d, \quad \left|\overrightarrow{P_0R_k}\right| \leq d, \quad \left|\overrightarrow{P_0R_h}\right| \leq d & \text{(closeness factor)}
\end{cases}
\end{aligned}
\tag{A.2}
$$

As can be seen in Eqs. A.1,A.2, for each family the fixed points can form three different configurations. The research ends when each of the six configurations belonging to the two families returns a qualified tetrahedron and the best interpolation tetrahedron is chosen as the one with minimum volume which guarantees the closeness of all vertices to P_0. A scheme of the overall algorithm for a single ghost point is shown in Fig. A.4 with details on the searching algorithm.

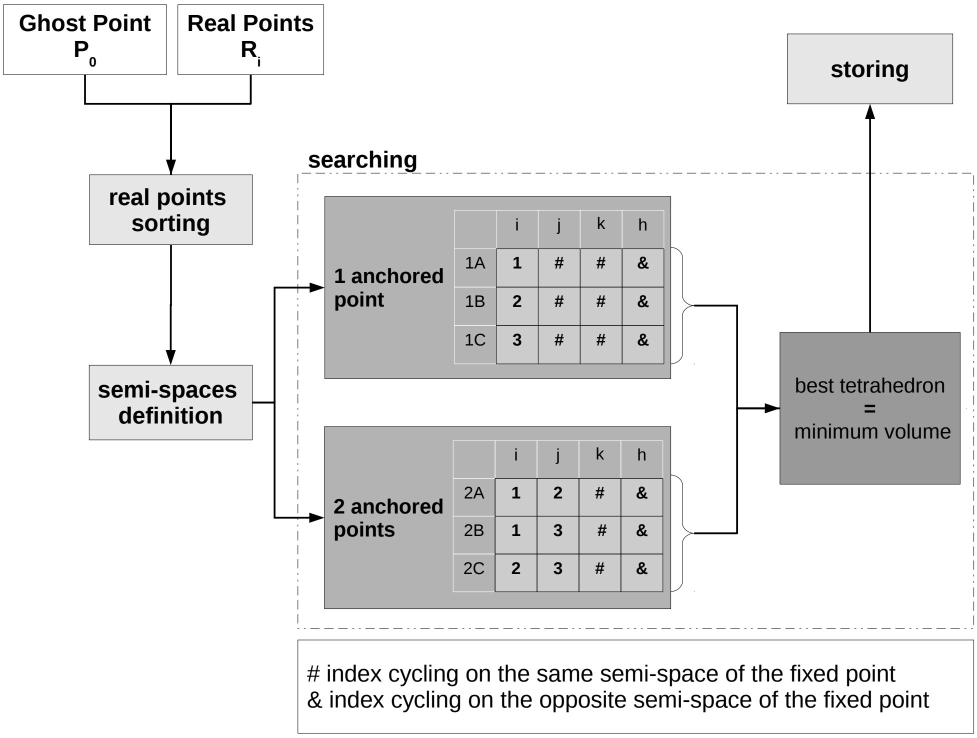

Figure A.4: Interpolation tetrahedron searching algorithm scheme

References

[1] Ogawara, A., Yoshikawa, K., Atsumi, M., Kishimoto, K., and Sack, W., “Dual Hydrogen/Methane Propellant Capability of the Expander-Bleed Cycle Engine,” ISTS 2008-a-07.

[2] Preclik, D., Hagemann, G., Knab, O., Brummer, L., Mading, C., Wiedmann, D., and Vuillermoz, P., “LOX/Hydrocarbon Propellant Trade Considerations for Future Reusable Liquid Booster Engines,” AIAA paper 2005-3567, July 2005, 41st AIAA/ASME/SAE/ASEE Joint Propulsion Conference and Exhibit.

[3] Breteau, J., Kachler, T., and Caruana, J., “European Space Agency Future Launchers Preparatory Programme Propulsion Demonstrators,” AIAA paper 2011-5551.

[4] Ordonneau, G., Vingert, L., Slavisnkaya, N., Sender, J., Suslov, D., Soller, S., Onofri, M., Bruno, C., Lentini, D., Nasuti, F., and Valorani, M., “Oxygen-methane Combustion Studies in In Space Propulsion Programme,” *4th European Conference for Aerospace Sciences, EUCASS 2011, Saint Petersburg, Russia, 3-7 July*, 2011.

[5] Ierardo, N., Biagioni, M., Pirrelli, P., Titkov, N., Shostak, A., De Lillis, A., and D’Aversa, E., “Development of the LM10-MIRA LOX-LNG Expander Cycle Engine for The Lyra Launch Vehicle,” Tech. rep., May.

[6] Preuss, A., Preclik, D., Mading, C., Gorgen, J., Soller, S., Haidn, O., Oschwald, M., Clauss, W., Arnold, R., and Sender, J., “LOX/Methane Technology Efforts for Future Liquid Rocket Engines,” Tech. rep., May 2008, 5th International Spacecraft Propulsion Conference.

[7] Vingert, L., Habiballah, M., and Vuillermoz, P., “Upgrading of the Mascotte cryogenic test bench to LOX/Methane combustion studies,” Tech. rep., Dec. 2002, 4th International Conference on Launcher Technology Space Launcher Liquid Propulsion.

[8] Preclik, D., Hagemann, G., Knab, O., Mading, C., Haeseler, D., Haidn, O., Woschnak, A., and Rosa, M. D., “LOX/Hydrocarbon Preparatory Thrust Chamber Technology Activities in Germany,” AIAA paper 2005-4555, July 2005, 41st AIAA/ASME/SAE/ASEE Joint Propulsion Conference and Exhibit.

[9] Crocker, A. and Peery, S., “System Sensitivity Studies of a LOX/Methane Expander Cycle Rocket Engine,” *34th AIAA/ASME/SAE/ASEE Joint Propulsion Conference and Exhibit, 13-15 July 1998, Cleveland, OH. AIAA-98-3674.*

[10] Schuff, R., Maier, M., Sindiy, O., Ulrich, C., and Fugger, S., "Integrated Modeling and Analysis for a LOX/Methane Expander Cycle Engine: Focusing on Regenerative Cooling Jacket Design," *42nd AIAA/ASME/SAE/ASEE Joint Propulsion Conference and Exhibit, 9-12 July 2006, Sacramento, CA. AIAA-2006-4534.*

[11] Saffel, R. and Moser, M. D., "GOX/Methane Injector Effects on Combustion Efficiency," AIAA paper 2008-4952, July 2008, 44th AIAA/ASME/SAE/ASEE Joint Propulsion Conference and Exhibit.

[12] Salgues, D., Mouis, G., Lee, S., Kalitan, D., Pal, S., and Santoro, R., "Shear and Swirl Coaxial Injector Studies of LOX/GCH4 Rocket Combustion Using Non-Intrusive Laser Diagnostics," AIAA paper 2006-0757, Jan. 2006, 44th AIAA Aerospace Science Meeting & Exhibit.

[13] Flynn, H., Lusby, B., and Villemarette, M., "Liquid Oxygen/ Liquid Methane Integrated Propulsion System Test Bed," AIAA paper 2011-5842, July 2011.

[14] Kawashima, H., Okita, K., Aoki, K., Azuma, N., Kumakawa, A., Onodera, T., Yoshida, S., Negishi, H., Manako, H., and Koganezawa, T., "Combustion and Regenerative Cooling Characteristics of LOX/Methane Engine," *Transactions of Space Technology Japan Volume 7, Issue ists26, pp. 7-11 (2009)..*

[15] Tomita, T., Ueda, S., Kawashima, H., Onodera, T., Kano, Y., Kubota, I., and Munenaga, T., "Status of Experimental Research on High Performance Methane-Fueled Rocket Thrust Chamber," Aiaa paper.

[16] Sutton, G. and Biblarz, O., *Rocket propulsion elements*, John Wiley & Sons, 2001.

[17] Haidn, O. J., "Advanced Rocket Engines," Tech. rep., 2008, Advances on Propulsion Technology for High-Speed Aircraft RTO-EN-AVT-150 , Paper n. 6.

[18] Knab, O., Frohlich, A., Wennerberg, D., and Haslinger, W., "Advanced Cooling Circuit Layout for the VINCI Expander Cycle Thrust Chamber," *38th AIAA/ASME/SAE/ASEE Joint Propulsion Conference and Exhibit, 7-10 July 2002, Indianapolis, IN. AIAA-2002-4005.*

[19] Pugh, R., "The Many Facets of the RL-10 Liquid Rocket Engine, a Continuing Success Story," *34th AIAA/ASME/SAE/ASEE Joint Propulsion Conference and Exhibit, 13-15 July 1998, Cleveland, OH. AIAA-98-3680.*

[20] Rachuk, V. and Titkov, N., "The First Russian LOX-LH$_2$ Expander Cycle LRE: RD0146," *42nd AIAA/ASME/SAE/ASEE Joint Propulsion Conference and Exhibit, 9-12 July 2006, Sacramento, CA. AIAA-2006-4904.*

[21] Cinnella, P., *Flux-Split Algorithmd for Flows with Non-Equilibrium Chemistry and Thermodynamics*, Ph.D. thesis, Virginia Polytechnic Institute and State University, 1989.

[22] Spalart, P. and Allmaras, S., "A One-equation Turbulence Model for Aerodynamic Flows," *La Recherche Aerospatiale 1, 5-23*, 1994.

[23] McBride, B. J. and Gordon, S., "Computer Program for Calculation of Complex Chemical Equilibrium Compositions and Applications," *NASA Reference Publication 1311*, 1994.

[24] Anderson, J. D., *Hypersonic and High-Temperature Gas Dynamics*, AIAA Education series, second edition ed., 2006.

[25] Sutton, K. and Gnoffo, P. A., "Multi-Component Diffusion with Application To Computational Aerothermodynamics," *7th AIAA/ASME Joint Thermophysics and Heat Transfer Conference June 15-18, 1998 / Albuquerque, NM - AIAA 98-2575*.

[26] Hirschfelder, J., Curtiss, C., Bird, R., and of Wisconsin. Theoretical Chemistry Laboratory, U., *Molecular theory of gases and liquids*, Wiley, 1954.

[27] Wilcox, D. C., *Turbulence Modeling for CFD*, D C W Industries, Inc., 1993.

[28] Yimer, I., Campbell, I., and Jiang, L.-Y., "Estimation of the turbulent Schmidt number from experimental profiles of Axial velocity and concentration for High-Reynolds-Number Jet flows," *Canadian aeronautics and space Journal, Vol.48, No.3*, 2002.

[29] He, G., Guo, Y., and Hsu, A., "The effect of Schmidt number on turbulent scalar mixing in a jet-in-crossflow," *International Journal of Heat and Mass Transfer, Vol.42, No.20, 3727-3738*, 1999.

[30] Xiao, X., Edwards, J., Hassan, H., and Cutler, G., "A Variable Turbulent Schmidt Number Formulation for Scramjet Application," AIAA paper 2005-1099, Jan. 2005, 43rd AIAA Aerospace Sciences Meeting and Exhibit.

[31] Brown, G. and Roshko, A., "On density effects and large structure in turbulent mixing layers," *J. Fluid Mech, Vol. 64, part 4, pp. 775-816*, 1974.

[32] Bogdanoff, D. W., "Compressibility effects in turbulent shear layer," *AIAA Journal, Vol.21, No.6 (926-927)*, 1983.

[33] Samimy, M., Reeder, M., and Elliott, G., "Compressibility effects on large scale structures in free shear flows," *Physics of Fluids A 4 1251-8*, 1992.

[34] Clemens, N. and Mungal, M., "Two- and Three- dimensional effects in the supersonic turbulent mixing layer," *AIAA Journal, Vol. 30, No. 4, pp. 973-981*, 1992.

[35] Papamoschou, D. and Roshko, A., "The Compressible Turbulent Shear Layer: an Experimental Study," *Journal of Fluid Mechanics Digit Archive,197:453-477*, 1988.

[36] Dimotakis, P. E., "Turbulent free shear layer mixing and combustion," *High Speed Flight Propulsion Systems, AIAA Progress in Astronautics and Aeronautics Series, Vol. 137, pp. 265-340,*, 1991.

[37] Paciorri, R. and Sabetta, F., "Compressibility Correction for the Spalart-Allmaras Model in Free-Shear Flows," *AIAA Journal of Spacecraft and Rockets, Vol. 40, No. 3*, 2003.

[38] Hirsch, C., *Numerical Computation of Internal and External Flows: Computational methods for inviscid and viscous flows*, Wiley, 1990.

[39] Godunov, S. K., "A Difference Scheme for Numerical Solution of Discontinuos Solution of Hydrodynamic Equations," , No. 47, 1959, pp. 271–306, translated US Joint Publ. Res. Service, JPRS 7226, 1969.

[40] Toro, E. F., *Riemann Solvers and Numerical Methods for Fluid Dynamics*, Springer-Verlag, Berlin, Germany, 1999.

[41] Geron, M., *Simulazioni Numeriche e Fenomenologie di Flussi Tridimensionali in un Aerospike Lineare, (in italian)*, Ph.D. thesis, Department of Mechanics and Aeronautics, 2005.

[42] Roy, C. J., McWherter-Payne, M. A., and Oberkampf, W. L., "Verification and Validation for Laminar Hypersonic Flowfields, Part 1: Verification," *AIAA Journal, Vol. 41, No. 10, October*, 2003.

[43] Back, L. H., Massier, P. F., and Gier, H. L., "Convective Heat Transfer in a Convergent-Divergent Nozzle," *NASA Technical Report No. 32-415*, 1965.

[44] DeLise, J. C. and Naraghi, M. H., "Comparative Studies of Convective Heat Transfer Models for Rocket Engines," AIAA Paper 1995-2499, July 1995, 31st AIAA/ASME/SAE/ASEE Joint Propulsion Conference.

[45] Liu, Q., Luke, E., Cinnella, P., and Tang, L., "Coupling Heat Transfer and Fluid Flow Solvers for Multidisciplinary Simulations," *Journal of Thermophysics and Heat Transfer*, Vol. 19, No. 4, 2005, pp. 417–427.

[46] Marineau, E., Schetz, J. A., and Neel, R. E., "Turbulent Navier-Stokes Simulations of Heat Transfer with Complex Wall Temperature Variations," AIAA Paper 2006-3087, June 2006, 9th AIAA/ASME Joint Thermophysics and Heat Transfer Conference.

[47] Thakre, P., *Chemical Erosion of Graphite and Refractory Metal Nozzles and its Mitigation in Solid-Propellant Rocket Motors*, Ph.D. thesis, Pennsylvania State University, 2008.

[48] Bartz, D. R., "Turbulent Boundary-Layer Heat Transfer from Rapidly Accelerating Flow of Rocket Combustion Gases and of Heated Air," Vol. 2 of *Advances in Heat Transfer*, 1965, pp. 1 – 108.

[49] Cruz, C. A. and Marshall, A. W., "Surface and Gas Measurements Along a Film-Cooled Wall," *Journal of Thermophysics and Heat Transfer, Vol. 21, No. 1, Jan-Mar 2007.*

[50] Goldstein, R. J., "Film Cooling," *Advances in Heat Transfer, Vol. 7, pp. 321-379,* 1971.

[51] Simon, F. F., "Jet Model for Slot Film Cooling with Effect of Free-stream and Coolant Turbulence," *NASA-TP-2655*, 1986.

[52] Dellimore, K. H., "Modeling and Simulation of Mixing Layer Flows For Rocket Engine Film Cooling," *Ph.D. Dissertation, University of Maryland*, 2010.

[53] Cutler, A. D., Diskin, G., Drummond, J., and White, J. A., "Supersonic Coaxial Jet Experiment for Computational Fluid Dynamics Code Validation," *AIAA Journal, Vol. 44, No. 3*, 2006.

[54] Dellimore, K. H., Cruz, C., Marshall, A. W., and Cadou, C. P., "Influence of a Streamwise Pressure Gradient on Film-Cooling Effectiveness," *Journal of Thermophysics and Heat Transfer, Vol.23, No.1, Jan-Mar 2009.*

[55] Dellimore, K. H., Marshall, A. W., and Cadou, C. P., "Influence of Compressibility on Film-Cooling Effectiveness," *Journal of Thermophysics and Heat Transfer, Vol.24, No.3, Jul-Sep 2010.*

[56] Dellimore, K. H., Marshall, A. W., Trouvé, A., and Cadou, C. P., "Numerical Simulation of Subsonic Slot-Jet Film Cooling of an Adiabatic Wall," *47th AIAA Aerospace Science Meeting Including The New Horizons Forum and Aerospace Exposition, 5-8 Jan 2009, Orlando, Florida. AIAA-2009-1577.*

[57] Voegele, A. P., Trouvé, A., Cadou, C., and Marshall, A., "RANS Modeling of 2D Adiabatic Slot Film Cooling," *46th AIAA/ASME/SAE/ASEE Joint Propulsion Conference and Exhibit, 25-28 July 2010, Nashville, TN - AIAA 2010-6735.*

[58] Kim, J. G., Lee, K. J., Seo, S., Han, Y. M., Kim, H. J., and Choi, H. S., "Film Cooling Effects on Wall Heat Flux of a Liquid Propellant Combustion Chamber," *42nd AIAA/ASME/SAE/ASEE Joint Propulsion Conference and Exhibit, 9-12 July 2006, Sacramento, CA. AIAA-2006-5196.*

[59] Arnold, R., Suslov, D., Haidn, O. J., and Weigand, B., "Circumferential Behavior of Tangential Film Cooling and Injector Wall Compatibility in a High Pressure LOX/GH_2 Subscale Combustion Chamber," *44th AIAA/ASME/SAE/ASEE Joint Propulsion Conference and Exhibit, 21-23 July 2008, Hartford, CT, AIAA 2008-5242.*

[60] Arnold, R., Suslov, D., and Haidn, O. J., "Film Cooling of Accelerated Flow in a Subscale Combustion Chamber," *Journal of Propulsion and Power Vol.25, No. 2, Mar-Apr 2009.*

[61] Arnold, R., Suslov, D., and Haidn, O. J., "Film Cooling in a High-Pressure Subscale Combustion Chamber," *Journal of Propulsion and Power, Vol.26, No. 3, May-Jun 2010.*

[62] Han, P. G., Namkoung, H. J., Kim, K. H., and Yoon, Y. B., "A Study on the Cooling Mechanism in Liquid Rocket Engines," *40th AIAA/ASME/SAE/ASEE Joint Propulsion Conference and Exhibit, 11-14 July 2004, Fort Laudardale, FL. AIAA-2004-3672.*

[63] Zhang, H. W., Tao, W. Q., He, Y. L., and Zhang, W., "Numerical Study of Liquid Film Cooling in a Rocket Combustion Chamber," *International Journal of Heat and Mass Transfer, Vol. 49, pp 349-358*, 2006.

[64] Zhang, H. W., He, Y. L., and Tao, W. Q., "Numerical Study of Film and Regenerative Cooling in a Thrust Chamber at High Pressure," *Numerical Heat Transfer, Part A, Vol.52, pp 991-1007*, 2007.

[65] Arnold, R., Suslov, D., Oschwald, M., Haidn, O. J., Aichner, T., Ivancic, B., and Frey, M., "Experimentally and Numerically Investigated Film Cooling in a Subscale Rocket Combustion Chamber," *3rd European Conference for Aerospace Sciences (EUCASS), July 2009.*

[66] Kim, J., Lee, K., Seo, S., Han, Y., Kim, H., and Choi, H., "Film Cooling Effects on Wall Heat Flux of a Liquid Propellant Combustion Chamber," AIAA paper 2006-5196, July 2006, 42nd AIAA/ASME/SAE/ASEE Joint Propulsion Conference and Exhibit.

[67] Kirchberger, C., Schlieben, G., Hupfer, A., Kau, H., , and Soller, S., "Film Cooling Investigations in a Kerosene/GOX Combustion Chamber," AIAA paper 2011-5777, July 2011, 47th AIAA/ASME/SAE/ASEE Joint Propulsion Conference.

[68] Arnold, R., Suslov, S., and Haidn, O. J., "Experimental Investigation of Film Cooling with Tangential Slot Injection in a LOX/CH4 Subscale Rocket Combustion Chamber," *26th International Symposium on Space Technology and Science (ISTS)*, 2008.

[69] Vaidyanathan, R., Tucker, P. K., Papila, N., and Shyy, W., "Computational-Fluid-Dynamics-Based Design Optimization for Single-Element Rocket Injector," *Journal of Propulsion and Power*, Vol. 20, No. 4, 2004.

[70] Cheng, G. C. and Farmer, R., "Real Fluid Modeling of Multiphase Flows in Liquid Rocket Engine Combustors," *Journal of Propulsion and Power*, Vol. 22, No. 6, 2006.

[71] Zong, N. and Yang, V., "Cryogenic Fluid Jets and Mixing Layers in Transcritical and Supercritical Environments," *Combustion Science and Technology, 178: 193-227*, 2006.

[72] Zong, N. and Yang, V., "Near-field Flow and Flame Dynamics of LOX/methane Shear Coaxial Injector Under Supercritical Conditions," *Proceedings of the Combustion Institute (31), 2309-2317*, 2007.

[73] Tsohas, J. and Heister, S. D., "CFD Simulations of Liquid Rocket Coaxial Injector Hydrodynamics," AIAA Paper 2009-5387, 2009, 45th AIAA/ASME/SAE/ASEE Joint Propulsion Conference & Exhibit 2 - 5 August 2009, Denver, Colorado.

[74] Lee, D. J., Thakur, S., Wright, J., Ihme, M., and Shyy, W., "Characterization of Flow Field Structure and Species Composition in a Shear Coaxial Rocket GH2/GO2 Injector: Modeling of Wall Heat Losses Turbulent Navier-Stokes Simulations of Heat Transfer with Complex Wall Temperature Variations," AIAA Paper 2011-6125, 2011, 47th AIAA/ASME/SAE/ASEE Joint Propulsion Conference & Exhibit 31 July - 03 August 2011, San Diego, California.

[75] Suslov, D. I., Arnold, R., and Haidn, O. J., "Investigation of Two Dimensional Thermal Loads in the Region near the Injector Head of a High Pressure Subscale Combustion Chamber," *47th AIAA Aerospace Sciences Meeting Including The New Horizons Forum And Aerospace Exposition 5-8 January 2009, Orlando, FL. AIAA-2009-450.*

[76] Wang, Q., Wu, F., Zeng, M., Luo, L., and Sun, J., "Numerical Simulation and Optimization on Heat Transfer and Fluid Flow in Cooling Channel of Liquid Rocket Engine Thrust Chamber," *Engineering Computations: International Journal for Computed-Aided Engineering and Software. Vol. 23 No. 8, pp.907-921*, 2006.

[77] Suslov, D., Betti, B., Aichner, T., Soller, S., Nasuti, F., and Haidn, O., "Experimental Investigation and CFD-Simulation of the Film Cooling in an O2/CH4 subscale Combustion Chamber," Proceeding, May 2012, 4th Space Propulsion Conference, Bordoeaux, France.

[78] Frohlich, A., Popp, M., Schmidt, G., and Thelemann, D., "Heat Transfer Characteristics of H_2/O_2: Combustion Chambers," AIAA Paper 1993-1826, July 1993, 29th AIAA/ASME/SAE/ASEE Joint Propulsion Conference.

[79] Kirchberger, C., Wagner, R., Kau, H., Soller, S., Martin, P., Bouchez, M., and Bonzom, C., "Prediction and Analysis of Heat Transfer in Small Rocket Chambers," AIAA Paper 2008-1260, July 2008, 44th AIAA/ASME/SAE/ASEE Joint Propulsion Conference.

[80] Marchi, C. H., Laroca, F., da Silva, A. F. C., and Hinckel, J. N., "Numerical Solutions of Flows in Rocket Engines with Regenerative Cooling," *Numerical Heat Transfer, Part A: Applications*, Vol. 45, No. 7, 2004, pp. 699–717.

[81] Wang, T. S. and Luong, V., "Hot-Gas-Side and Coolant-Side Heat Transfer in Liquid Rocket Engine Combustors," *Journal of Thermophysics and Heat Transfer*, Vol. 8, No. 3, 1994, pp. 524–530.

[82] Naraghi, M. H., Dunn, S., and Coats, D., "A Model for Design and Analysis of Regeneratively Cooled Rocket Engines," AIAA Paper 2004-3852, July 2004, 40th AIAA/ASME/SAE/ASEE Joint Propulsion Conference.

[83] Naraghi, M. H. and Jokhakar, J., "A CFD-RTE Model for Thermal Analysis of regeneratively Cooled Rocket Engines," AIAA Paper 2008-4557, July 2008, 44th AIAA/ASME/SAE/ASEE Joint Propulsion Conference.

[84] Kang, Y. D. and Sun, B., "Numerical Simulation of Liquid Rocket Engine Thrust Chamber Regenerative Cooling," *Journal of Thermophysics and Heat Transfer*, Vol. 25, No. 1, 2011, pp. 155–164.

[85] Pizzarelli, M., Betti, B., and Nasuti, F., "Coupled analysis of hot-gas and coolant flows in LOX/methane thrust chambers," Tech. rep., July 2011, 4th European Conference for Aerospace Sciences, EUCASS, Saint Petersburg, Russia.

[86] Pizzarelli, M., Nasuti, F., and Onofri, M., "A Simplified Model for the Analysis of Thermal Stratification in Cooling Channels," 2nd European Conference for Aerospace Sciences, July 2007.

[87] Pizzarelli, M., Carapellese, S., and Nasuti, F., "A Quasi-2D Model for the Prediction of Wall Temperature of Rocket Engine Cooling Channels," *Numerical Heat Transfer, Part A: Applications*, Vol. 60, No. 1, July 2011, pp. 1–24.

[88] Yagley, J., Feng, J., Merkle, C., and Lee, Y.-T., "The Effect of Aspect Ratio on the Effectiveness of Combustor Coolant Passages," AIAA Paper 1992-3153, July 1992, 28th AIAA/ASME/SAE/ASEE Joint Propulsion Conference.

[89] LeBail, F. and Popp, M., "Numerical Analysis of High Aspect Ratio Cooling Passage Flow and Heat Transfer," AIAA Paper 1993-1829, June 1993, 29th AIAA/ASME/SAE/ASEE Joint Propulsion Conference.

[90] Yagley, J., Feng, J., and Merkle, C., "CFD Analyses of Coolant Channel Flowfields," AIAA Paper 1993-1830, June 1993, 29th AIAA/ASME/SAE/ASEE Joint Propulsion Conference.

[91] Knab, O., Fröhlich, A., Wennerberg, D., and Haslinger, W., "Advanced Cooling Circuit Layout for the VINCI Expander Cycle Thrust Chamber," AIAA Paper 2002-4005, July 2002, 38th AIAA/ASME/SAE/ASEE Joint Propulsion Conference.

[92] Jung, H., Merkle, C., Schuff, R., and Anderson, W., "Detailed Flowfield Predictions of Heat Transfer to Supercritical Fluids in High Aspect Ratio Channels," AIAA Paper 2007-5548, July 2007, 43rd AIAA/ASME/SAE/ASEE Joint Propulsion Conference.

[93] Pizzarelli, M., Nasuti, F., and Onofri, M., "Flow Analysis of Transcritical Methane in Rectangular Cooling Channels," AIAA Paper 2008-4556, July 2008, 44th AIAA/ASME/SAE/ASEE Joint Propulsion Conference.

[94] Pizzarelli, M., Nasuti, F., Paciorri, R., and Onofri, M., "Numerical Analysis of Three-Dimensional Flow of Supercritical Fluid in Cooling Channels," *AIAA Journal, Vol. 47, No. 11 (2534-2543)*, 2009.

[95] Younglove, B. and Ely, J., "Thermophysical Properties of Fluids. II. Methane, Ethane, Propane, Isobutane, and Normal Butane," *Journal of Physical and Chemical Reference Data*, Vol. 16, No. 4, June 1987, pp. 577–798.

[96] Colebrook, C. F., "Turbulent Flow in Pipes with Particular Reference to the Transition Region Between the Smooth and Rough Pipe Flow," *J. Inst. Civ. Eng.*, , No. 11, 1938, pp. 133–156.

[97] Sieder, E. N. and Tate, G. E., "Heat Transfer and Pressure Drop of Liquids in Tubes," *Industrial and Engineering Chemistry*, Vol. 28, No. 12, 1936, pp. 1429–1435.

[98] Peery, S. and Minick, A., "Design and Development of an Advanced Expander Combustor," *34th AIAA/ASME/SAE/ASEE Joint Propulsion Conference and Exhibit, 13-15 July 1998, Cleveland, OH. AIAA-98-3675.*

[99] Fujita, M., Aoki, H., Nakagawa, T., Tokunaga, T., Yasui, M., and Iwama, K., "Upper Stage Propulsion System for H-IIA Launch Vehicle," *38th AIAA/ASME/SAE/ASEE Joint Propulsion Conference and Exhibit, 7-10 July 2002, Indianapolis, IN. AIAA-2002-4212.*

[100] Caisso, P., Souchier, A., Rothmund, C., Alliot, P., Bonhomme, C., Zinner, W., Parsley, R., Neill, T., Forde, S., Starke, R., Wang, W., Takahashi, M., Atsumi, M., and Valentian, D., "A liquid propulsion panorama," *Acta Astronautica*, Vol. 65, No. 11-12, 2009, pp. 1723 – 1737.

[101] El-Samni, O. A., Chun, H. H., and Yoon, H. S., "Drag reduction of turbulent flow over thin rectangular riblets," *International Journal of Engineering Science*, Vol. 45, 2007, pp. 436–454.

[102] Stalio, E. and Nobile, E., "Direct Numerical Simulation of Heat Transfer over Riblets," *International Journal of Heat and Fluid Flow*, Vol. 24, 2003, pp. 356–371.

[103] Launder, B. E. and Li, S. P., "On the prediction of riblet performance with engineering turbulence models," *Applied Scientific Research*, Vol. 50, 1993, pp. 283–298.

[104] Aupoix, B., Pailhas, G., and Houdeville, R., "Towards a General Strategy to Model Riblet Effects," *AIAA Journal*, Vol. 50, No. 3, 2012, pp. 708–716.

[105] Benhalilou, M. and Kasagi, N., "Numerical Prediction of Heat and Momentum transfer over micro-grooved surface with a non-linear $k-\varepsilon$ model," *International Journal of Heat and Mass Transfer*, Vol. 42, 1999, pp. 2525–2541.

[106] Walsh, M. J. and Weinstein, L. M., "Drag and Heat-Transfer Characteristics of Small Longitudinally Ribbed Surfaces," *AIAA Journal*, Vol. 17, No. 7, 1979, pp. 770–771.

[107] Lindemann, A. M., "Turbulent Reynolds Analogy Factors for Nonplanar Surface Microgeometries," *Journal of Spacecraft and Rockets*, Vol. 22, No. 5, 1985, pp. 581–582.

[108] Choi, K.-S. and Orchard, D. M., "Turbulence Management Using Riblets for Heat and Momentum Transfer," *Experimental Thermal and Fluid Science*, Vol. 15, 1997, pp. 109–124.

[109] Kawashima, H., Sakamoto, H., Takahashi, M., Sasaki, M., and Kumakawa, A., "Hot-gas-side Heat Transfer Characteristics of a Ribbed Combustor," *45th AIAA/ASME/SAE/ASEE Joint Propulsion Conference and Exhibit, 2-5 August 2009, Denver, CO. AIAA-2009-5476.*

[110] Immich, H., Alting, J., Kretschmer, J., and Preclik, D., "Technology Developments for Thrust Chambers of Future Launch Vehicle Liquid Rocket Engines," *Acta Astronautica 53, 2003, 597-605.*

[111] Negishi, H., Kumakawa, A., Moriya, S., Yamanishi, N., and Sunakawa, H., "Numerical Investigations of Heat Transfer Enhancement in a Thrust Chamber with Hot Gas Side Wall Ribs," *47th AIAA Aerospace Sciences Meeting Including The New Horizons Forum ANd Aerospace Exposition 5-8 January 2009, Orlando, FL. AIAA-2009-830.*

[112] Schlichting, H. and Gersten, K., *Boundary-layer theory*, Springer, 2000.

[113] Baily, R. D., "Enhanced heat transfer combustor technology, subtasks 1 and 2, tast C.1," Tech. Rep. NASA-CR-179541, NASA, 1986.

[114] Leinard, IV, J. H. and Leinard, V, J. H., *A Heat Transfer Textbook*, Phlogiston Press, 2005.

[115] Pizzarelli, M., Nasuti, F., and Onofri, M., "Coupled Numerical Simulation of Wall Heat Conduction and Coolant Flow in Liquid Rocket Engines," AIAA Paper 2011-5623, Jul.-Aug. 2011, 47th AIAA/ASME/SAE/ASEE Joint Propulsion Conference.

[116] Brown, C., "Conceptual Investigations for a Methane-Fueled Expander Rocket Engine," *40th AIAA/ASME/SAE/ASEE Joint Propulsion Conference and Exhibit, 11-14 July 2004, Fort Laudardale, FL. AIAA-2004-4210.*

[117] Arione, L., Ierardo, N., Rudnykh, M., Caggiano, G., Lobov, S., Shostak, A., De Lillis, A., and D'Aversa, E., "Development status of the LM10-MIRA LOX-LNG Expander Cycle Engine for The LYRA Launch Vehicle," *6th International Spacecraft Propulsion Conference, 3 - 6 May 2010, San Sebastian, Spain.*

[118] AVIO, personal communication, 2010.

[119] Cormen, T., *Introduction to algorithms*, MIT electrical engineering and computer science series, MIT Press, 2001.